DIGITAL HOLOGRAPHY EFFICIENCY EXPERIMENTS FOR TACTICAL APPLICATIONS

DISSERTATION

Douglas E. Thornton, Major, USAF

AFIT-ENP-DS-19-S-029

DEPARTMENT OF THE AIR FORCE
AIR UNIVERSITY

AIR FORCE INSTITUTE OF TECHNOLOGY

Wright-Patterson Air Force Base, Ohio

AFIT/DS/ENP/19-S-029

DIGITAL HOLOGRAPHY EFFICIENCY EXPERIMENTS FOR TACTICAL APPLICATIONS

DISSERTATION

Presented to the Faculty

Graduate School of Engineering and Management

Air Force Institute of Technology

Air University

Air Education and Training Command

in Partial Fulfillment of the Requirements for the

Degree of Doctor of Philosophy in Applied Physics

Douglas E. Thornton, B.S.E.E., M.S.E.E.

Major, USAF

September 2019

AFIT/DS/ENP/19-S-029

DIGITAL HOLOGRAPHY EFFICIENCY EXPERIMENTS FOR TACTICAL APPLICATIONS

DISSERTATION

Douglas E. Thornton, B.S.E.E., M.S.E.E.
Major, USAF

Committee Membership:

Glen P. Perram, PhD
Chairman

Mark F. Spencer, PhD
Member

Steve T. Fiorino, PhD
Member

Benjamin F. Akers, PhD
Member

ADEDJI B. BADIRU, PhD
Dean, Graduate School of Engineering and Management

AFIT/DS/ENP/19-S-029

Abstract

This dissertation analyzes the system efficiencies (multiplicative losses) of a digital holography (DH) system for tactical applications and is comprised of four unique contributions. For the first contribution, the performance of DH in the on-axis phase shifting recording geometry is compared to a similar, well-studied wavefront sensor for deep turbulence, the self-referencing interferometer (SRI), which has known efficiency losses. Wave-optics simulations with deep-turbulence conditions and noise were conducted and the results show that DH outperforms the SRI by 10's of dB due to DH's strong reference beam. In the second contribution, an experiment with DH in the off-axis image plane recording geometry was conducted with a continuous-wave laser with near-ideal laser coherence to quantity the major system efficiencies. The experimental results show that the mixing efficiency (37%) is the dominant efficiency loss; however, excess reference (75%) and signal noise (3%-100%) are significant efficiency losses as well. For the third contribution, additional experiments show that the the mixing efficiency depends on the coherence efficiency of the master oscillator (MO) laser, which degrades with range. Here, the MO laser was phase modulated to represent multi-longitudinal mode operation and rapid-frequency fluctuations. The experimental results show that DH effectively measures the coherence efficiency to within 3.2% from the spectral models for both effects. Since the MO laser spectrum is related to the coherence efficiency, the losses as a function of range can be well determined from the MO laser spectrum. Finally, in the fourth contribution, further experiments showed that if the MO laser has significant low frequency laser frequency noise, the coherence efficiency can be increased by decreasing the hologram measurement time (from 100 ms to 100 μs), thus filtering the laser frequency noise

and increasing the effective range by 280%. Altogether, the results from these four contributions provide the framework to estimate the major system losses for designing a tactical DH system and have been or will be published in peer-reviewed journal articles.

To my wife and son.

Acknowledgements

I would like to first thank my advisor Dr. Glen Perram for his guidance through this journey, wisdom on solving tough problems, and patience when lab equipment broke. The primary reason I decided to return to AFIT for my PhD was because I truly enjoyed my time and research as a Masters student under his tutelage. Since I was fortunate enough to be his student again, I am truly appreciative for the work and growth I've accomplished because of him. I have enjoyed these past few years even more.

Next, I would like to thank Dr. Christopher Rice for his support and sage advice over the years. Whenever I had issues in the lab, needed to brainstorm ideas, or became conflicted on minute nuances, he provided the insight and past experiences I needed to progress. I am truly appreciative of the amount of time he unselfishly provided to help me be successful.

Furthermore, I need to extend my gratitude to my committee member and sponsor, Dr. Mark Spencer. When learning that I'd be coming back to AFIT, he offered research opportunities and extended support from 1,400 miles away. I greatly appreciate the many pages of feedback on my writings, the one month "internship" at Kirtland AFB to start up my digital holography lab at AFIT, and the collaboration on the digital holography demonstrator for STEM outreach. His support and mentorship has been indispensable throughout this journey.

Additionally, I have to thank my other committee members, many members of the EN faculty, AFRL/RY, and fellow students. I appreciate Dr. Fiorino's and Dr. Akers's feedback, insight, and support through the dissertation process. Next, I would like to thank Dr. Marciniak and Lt Col Butler for their advisement and support of the student SPIE chapter, which is an invaluable resource and experience for students at AFIT. I'd like to also thank Lt Col Hyde, Dr. Basu, and Dr. McCrae for their

perspective on my research problems. Next, I appreciate the insight and solutions Dr. Stafford and Mr. Miller from AFRL/RY provided on my lab issues. Additionally, I need thank Capt Mao for his Masters research in the lab and perspective for follow on experiments, and my fellow students for the homework help, an ear to whine to, and sharing advice.

Lastly, I am truly appreciative of the support from my wife, family, and friends. Without them, this wouldn't have been possible.

Douglas E. Thornton

Table of Contents

Page

List of Figures

List of Tables

List of Symbols

Symbol		Page
$\mathcal{N}_k$	Circular-complex Gaussian random number [*uniteless*]	10
(f_x, f_y)	Fourier plane coordinates $[1/p]$	10
q_I	Image-plane sampling quotient[*unitless*]	11
d_p	Pupil diameter $[m]$	11
σ_I^2	Compressed-noise variance $[pe^2]$	12
η_s	Spatial integration efficiency [%]	12
S/N	Signal-to-noise ratio [*unitless*]	13
η_T	Total efficiency [%]	13
r_0	Fried Coherence Length $[m]$	14
σ_χ^2	Rytov Number of Log-Amplitude Variance [*unitless*]	14
θ_0	Isoplanatic Angle [*rads*]	14
C_n^2	Index of Refraction Structure Constant $[m^{-2/3}]$	14
k	Wave number $[1/m]$	14
τ	Time delay $[s]$	17
$\mathcal{V}$	Fringe visibility [*unitless*]	18
$\gamma(\tau)$	Normalized complex degree of coherence [*unitless*]	18
$\mathcal{G}(\nu)$	Power spectral density $[unit^2/Hz]$	18
τ_c	Coherence time $[s]$	19
ℓ_c	Coherence length $[m]$	19
c	Speed of light$[m/s]$	19
$\Delta\nu$	Spectral full-width at half-max linewidth $[Hz]$	19

List of Abbreviations

Abbreviation		Page
DH	Digital holography	1
AO	Adaptive Optics	1
FOV	Field Of View	1
SNR	Signal-to-noise ratio	2
IPRG	Image Plane Recording Geometry	5
MO	Master Oscillator	5
LO	Local Oscillator	5
FPA	Focal Plane Array	5
pe	photoelectrons	7
DN	Digital Number	9
PSD	Power Spectral Density	18
PSO	Phase Shifting Optics	25
BS	Beam Splitter	25
QWP	Quarter-Wave Plate	25
MTF	Modulation Transfer Function	51
FI	Faraday Isolator	59
HWP	Half-Wave Plate	59
PBS	Polarizing Beam Splitter	59
BD	Beam Dump	59
ND	Neutral Density	59
FP	Fabry-Perot	60
FFT	Fast Fourier Transform	115

DIGITAL HOLOGRAPHY EFFICIENCY EXPERIMENTS FOR TACTICAL APPLICATIONS

I. Introduction

In the late 1960's, Goodman, Gaskill, and others paved the way for using holography for wavefront sensing for tactical applications [1, 2, 3, 4]. Since then, digital holography (DH) has been well studied for a variety of applications like microscopy [5, 6] and optical coherence tomography [7, 8], which typically involve table-top systems in controlled environments. On the other hand, military tactical applications like wavefront sensing [9], long-range imaging [10], and 3D imaging [11] involve long propagation paths through the atmosphere. For these tactical applications, DH offers distinct advantages over direct-detection methods, since it provides access to the complex-optical field (i.e., both the amplitude and phase) and enables increased sensitivity due to coherent detection with a strong reference.

When light propagates through the Earths atmosphere, small temperature differences lead to tiny refractive-index differences that cause aberrations known as optical turbulence. Traditional adaptive optics (AO) systems attempt to sense and correct for these aberrations and achieve near-diffraction-limited performance given weak-turbulence conditions [12]. With weak-turbulence conditions, constructive and destructive interference known as scintillation is negligible and the optical system is isoplanatic [i.e., a single phase estimate corrects the entire field of view (FOV)]. However, under deep-turbulence conditions, also called distributed-volume turbulence, the scintillation becomes appreciable with total-destructive interference. This outcome causes branch points and cuts to arise in the phase function and the aberrations be-

come anisoplanatic (i.e., multiple phase estimates are needed to correct the entire FOV). These effects cause traditional AO system performance to quickly degrade.

Along with scintillation from long atmospheric paths, the light also experiences extinction (i.e., absorption and scattering). Both of these effects lead to weak signals. For direct detection systems, like those used in traditional AO systems, the measured signal must be above the system's noise floor to achieve the detection threshold. Since DH uses coherent detection, the signal light is interfered with a reference light source. When a strong reference is used, this interference boosts the weak signal above the system's noise floor and enables increased sensitivity due to coherent detection with a strong reference (as previously mentioned).

Additionally, DH provides other distinct benefits for tactical applications. The branch points, which arise from nulls in the real and imaginary parts of the complex-optical field, cause traditional AO systems to fail [13]. This failure is the result of the inability to both sense and correct for the branch points and associated branch cuts, which are 2π discontinuities in the phase function. With that said, the wrapped-phase function provided by DH directly contains these branch points and branch cuts; thus, DH can be used to overcome their effects.

Lastly, traditional AO systems cannot resolve anisoplanatism with the use of a single phase-function estimate and correction. Since DH estimates and corrects the phase function digitally, multi-plane algorithms can be used. [14, 15, 16, 17]. These multi-plane algorithms enable enhanced performance when in the presence of anisoplanatism without the use of additional hardware.

With the above benefits in mind, the performance of DH can be characterized using the signal-to-noise ratio (SNR). Naturally, the strong reference of DH enables increased sensitivity and can preform well in weak signal environments like those given with deep-turbulence conditions. However, there are phenomenon that reduce

the SNR and therefore reduce performance. These phenomenon can be characterized as system efficiencies or multiplicative losses to the SNR. Some phenomenon, like the detector quantum efficiency, can be viewed as a constant and independent DH system operation. Other phenomenon, like coherence, can be dynamic, and dependent on non-ideal hardware performance and DH system operation. To fully comprehend the performance capabilities and limits of a DH system for tactical applications, an understanding of the major DH system efficiencies is required.

Past efforts have explored the use of DH for tactical applications. With that said, many hologram recording geometries exist for DH and each recording geometry has different considerations depending on the application [18, 19]. In particular, the off-axis image plane and pupil plane recording geometries have been studied for the deep-turbulence wavefront sensing using modeling and simulation [20, 21]. Additionally, field tests have been conducted at ranges of 100 m and 1.5 km [10, 22]. Their results focus on the phase error estimation and correction, but lack details on the DH system hardware and performance, which gives rise to the purpose of this dissertation effort.

The overall goal of this dissertation is to analyze the system efficiencies (multiplicative losses) associated with a DH system for tactical applications. With the above introductory comments in mind, this dissertation proceeds in the following manner. Chapter II provides the background information on DH, turbulence, and temporal coherence. Then, the individual contributions are presented in the following Chapters:

Chapter III: The performance of the on-axis phase shifting recording geometry of DH is analyzed and compared to the self-reference interferometer using wave-optics simulations with deep-turbulence conditions and noise.

Chapter IV: DH efficiency experiments are conducted to quantify the major system efficiencies with excess noise.

Chapter V: The coherence efficiency of DH is experimentally measured and compared to the spectrum of a multi-mode and linewidth-broaden MO laser.

Chapter VI: The mixing efficiency is fully characterized to account for vibrational and coherence effects and shows the coherence efficiency at range is inversely proportional to the hologram integration time.

Lastly, the conclusions are summarized in Chapter VII with recommendations for future work.

II. Background

This chapter provides the background material for the contributions presented in Ch. III - VI. First, the fundamentals of digital holography in the off-axis image plane recording geometry (IPRG) is discussed. Then, the optical characteristics of turbulence and conditions for deep turbulence is presented. Lastly, temporal coherence theory is discussed with respect to DH.

2.1 Digital holography in the off-axis image plane recording geometry

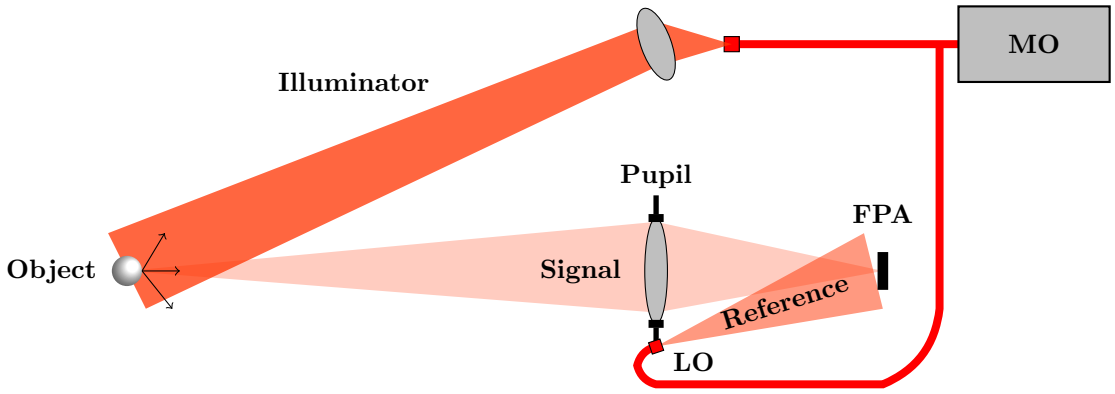

Figure 2.1. Optical setup of DH in the off-axis image plane recording geometry (IPRG)

Figure 2.1 illustrates the optical setup of DH in the off-axis image plane recording geometry (IPRG). The master oscillator (MO) laser is split into two paths: the illuminator to flood illuminate the imaged object and a local oscillator (LO) to provide the reference light. The scattered light from the object becomes the signal light and is imaged onto the focal plane array (FPA) by the receiver pupil lens. At the FPA, the signal is interfered with the reference to create the hologram. The interference produces spatial fringes in the hologram, which is demodulated to gain access to the signal complex-optical field. The ensuing sections mathematically describe the hologram detection and noise, how the signal complex-optical field is estimated, and then

formulates the signal-to-noise ratio. The definitions of the special functions used in this section can be found in App. A. Further details can be found in the *Encyclopedia of Modern Optics II* article on"Spatial Heterodyne" by Spencer [23].

2.1.1 Hologram Detection and Noise

Using the Fresnel approximation for a tilted spherical wave, the complex-optical field of the reference, U_R, is described as

$$\begin{aligned} U_R(x,y) =& A_R\, e^{j2\pi z_I/\lambda} \exp\left[j\frac{\pi}{\lambda z_I}\left(x^2+y^2\right)\right] \\ & \exp\left[j2\pi x_R\frac{x}{\lambda z_I}\right]\exp\left[j2\pi y_R\frac{y}{\lambda z_I}\right], \end{aligned} \tag{2.1}$$

where (x,y) are the FPA coordinates, A_R is a complex constant, z_I is the image distance, λ is the MO wavelength, and (x_R, y_R) are the pupil coordinates at the injection of the reference light. Note that A_R is a complex constant assuming uniform illumination of the FPA. At the FPA, the signal and reference light interfere and produces the hologram irradiance, i_H. In units of W/m^2,

$$\begin{aligned} i_H(x,y) =& \left|U_S(x,y)+U_R(x,y)\right|^2 \\ =& \left|U_S(x,y)\right|^2+\left|U_R(x,y)\right|^2 \\ &+\left|U_S(x,y)\,U_R^*(x,y)\right| \\ &+\left|U_S^*(x,y)\,U_R(x,y)\right|, \end{aligned} \tag{2.2}$$

where U_S is the signal complex-optical field and * denotes complex conjugate. Here, the hologram irradiance is spatially continuous and is real valued. The absolute value of the third and forth terms eliminates residual phase.

Note that the signal incurs optical losses upon reaching the FPA, which is represented by the transmission efficiency, η_t. Additionally, the signal is often assumed

to 100% depolarized due to the rough-surface scattering of the a dielectric object. Since the reference light is 100% polarized, the magnitude of the third and fourth interference terms of Eq. (2.2) is decreased by 50% of the signal irradiance or 70.7% of the signal field amplitude, which is represented by the polarization efficiency, η_p. The inclusion of these factors into Eq. (2.2) gives

$$\begin{aligned} i_H(x,y) = \eta_t \left|U_S(x,y)\right|^2 + \left|U_R(x,y)\right|^2 \\ + \sqrt{\eta_t \eta_p}\ \left|U_S(x,y)\, U_R^*(x,y)\right| \\ + \sqrt{\eta_t \eta_p}\ \left|U_S^*(x,y)\, U_R(x,y)\right|. \end{aligned} \tag{2.3}$$

Also note that losses due to temporal coherence between the signal and reference are neglected. This effect is discussed in detail in Ch. 2.3.

The FPA records the hologram on an $M \times N$ rectangular array of square pixels of width p (assuming 100% pixel fill factor). The recording of the continuous hologram is described as a 2D-convolution of the hologram irradiance with a 2D-rectangle function (representing the spatial-pixel averaging) [24]:

$$\hat{i}_H(x',y') = \frac{1}{p^2}\left[i_H(x',y') ** \operatorname{rect}\left(\frac{x'}{p}, \frac{y'}{p}\right)\right], \tag{2.4}$$

where $\hat{i}_H$ is the pixel-averaged hologram irradiance in units of W/m^2, (x', y') is the sampled hologram plane coordinates, and $**$ denotes a 2D-convolution. Here, $x' = np$ and $y' = mp$ where $n = -\frac{N}{2} \ldots, \frac{N}{2} - 1$ and $m = -\frac{M}{2}, \ldots, \frac{M}{2} - 1$ for even M and N. However from hereon, we refer to sample coordinates without the accent. The FPA converts the random arrival of photons to electrons over an integration time, t_i. The sampled mean number of hologram photoelectrons (pe), $\overline{m}_H$, is

$$\overline{m}_H(x,y) = \eta_q \frac{t_i p^2}{h\nu}\ \hat{i}_H(x,y), \tag{2.5}$$

where η_q is the FPA quantum efficiency, h is Planck's constant, and ν is the MO laser frequency [25]. Similarly, a the mean number of signal photoelectrons, $\overline{m}_S$, is

$$\overline{m}_S(x,y) = \eta_q \frac{t_i p^2}{h\nu} \left|U(x,y)\right|^2 \tag{2.6}$$

and the mean number of reference photoelectrons, $\overline{m}_R$, is

$$\overline{m}_R = \eta_q \frac{t_i p^2}{h\nu} \left|A_R\right|^2. \tag{2.7}$$

Again, we assume a spatially uniform reference light and $\overline{m}_R$ is independent of pixel location. Note that Eq. (2.5) - (2.7) do not contain noise.

The strong-reference assumption enables DH detection at the shot noise limit and drives the development of the noise model. Our noise model is Gaussian and additive, and as such,

$$\overline{m}_H^+(x,y) = \overline{m}_H(x,y) + \sigma_n n_k(x,y), \tag{2.8}$$

where $\overline{m}_H^+(x,y)$ is the mean hologram photoelectron count with noise, σ_n is the noise standard deviation, and $n_k(x,y)$ is the kth realization of real-valued, zero-mean, unit-variance Gaussian random numbers. To achieve a strong reference, we set the reference strength to fill the pixel-well depth, such that the hologram noise is reference shot noise dominate, but pixel saturation is avoided. Shot noise has a Poisson distribution, but can be approximated as a Gaussian distribution when $\overline{m}_H \gg 1$. Also, it is independent of the FPA read noise, so the total noise becomes

$$\sigma_n^2(x,y) = \overline{m}_H(x,y) + \sigma_r^2, \tag{2.9}$$

where $\sigma_n^2(x,y)$ is the total noise variance, $\overline{m}_H(x,y)$ is the hologram shot-noise variance, and σ_r^2 is the read-noise variance, all in units of pe^2. Often with the strong-

reference approximation, $\overline{m}_H \approx \overline{m}_R$ and $\overline{m}_R \gg \sigma_r^2$, so the only noise contribution considered is the reference shot noise. However, there are cases where other sources of shot noise must be accounted.

The FPA digitizes the photoelectrons to discrete values, d_H, with units of DN [26]. The digitization is described with additive quantization noise [27] as

$$d_H^+(x,y) = g_{A/D}\overline{m}_H^+(x,y) + \sigma_q u_k(x,y), \tag{2.10}$$

where $d_H^+(x,y)$ is the mean hologram digital number with noise, $g_{A/D}$ is the analog-to-digital gain (DN/pe), σ_q is the quantization-noise standard deviation, and $u_k(x,y)$ is real-valued, zero-mean, random numbers from -0.5 to 0.5 with a uniform distribution. The quantization-noise variance is

$$\sigma_q^2 = \frac{LSB^2}{12}, \tag{2.11}$$

where LSB is the least-significant bit. In most cases, the quantization noise is negligible, especially for high bit depths (e.g. 14-bit), therefore it is neglected in the ensuing development. Additionally, other noise sources exist [28, 26], but are also typically negligible.

2.1.2 Hologram Demodulation

In the hologram, the reference spatially modulates the signal. This encodes the signal light in the hologram and the demodulation process provides access to the signal complex-optical field. Since the image and pupil planes are Fourier transform pairs [29], the Fourier transform of the hologram provides access the signal complex-optical field in the pupil. The hologram is recorded in an image plane, so the discrete

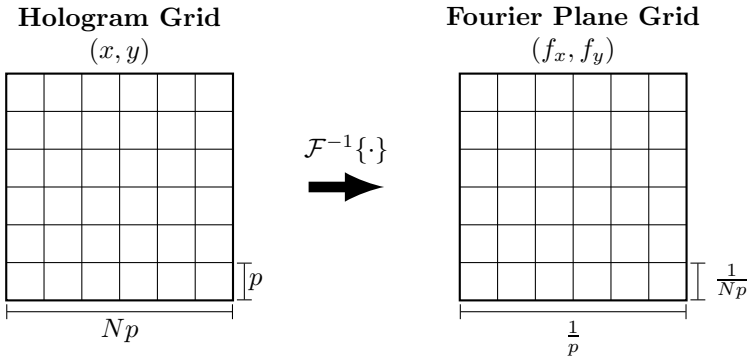

Figure 2.2. Spatial sampling between the recorded hologram and Fourier plane on a square grid (i.e., $M = N$).

inverse Fourier transform, $\mathcal{DFT}^{-1}$, is operated on $d_H^+(n,m)$ to arrive at

$$\begin{aligned}\mathcal{DFT}^{-1}\left\{d_H^+(x,y)\right\} =& D_H^+(f_x,f_y)\\ =& g_{A/D}\eta_q\frac{t_i}{h\nu}\mathcal{DFT}^{-1}\left\{i_H(x,y)\right\}\operatorname{sinc}(p\,f_x,p\,f_y)\\ &+ g_{A/D}\frac{\sigma_n}{\sqrt{2}}\,\mathcal{N}_k(f_x,f_y),\end{aligned} \tag{2.12}$$

where $\mathcal{N}_k$ is the kth realization of circular-complex Gaussian random numbers with zero-mean and unit-variance for both the real and imaginary components (hence the $\sqrt{2}$ factor) and (f_x, f_y) are the sampled Fourier plane coordinates. As illustrated in Fig. 2.2, the Fourier plane is represented in image-plane spatial-frequency coordinates, $f_x = \frac{n}{N}$ and $f_y = \frac{m}{M}$ in units of $1/p$ or per pixel. Additionally, the 2D-sinc appears from the rect convolution in Eq. (2.4).

Then, the $\mathcal{DFT}^{-1}$ of the hologram irradiance is evaluated as

$$\begin{aligned}&\mathcal{DFT}^{-1}\left\{i_H(x,y)\right\} = |A_R|^2\,\delta(f_x,f_y)\\ &+\eta_t\widetilde{U}_S(f_x,f_y) * *\widetilde{U}_S^*(f_x,f_y)\\ &+\sqrt{\eta_t\eta_p}A_R^*\widetilde{U}_S\left(f_x-\frac{x_R}{\lambda z_I},f_y-\frac{y_R}{\lambda z_I}\right)\\ &-\sqrt{\eta_t\eta_p}A_R\widetilde{U}_S^*\left(f_x+\frac{x_R}{\lambda z_I},f_y+\frac{y_R}{\lambda z_I}\right),\end{aligned} \tag{2.13}$$

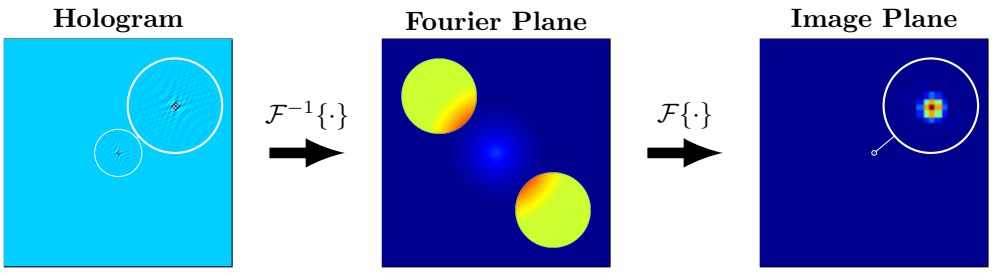

Figure 2.3. An illustration of the demodulation process of a point source without noise

where δ is the impulse function and $\widetilde{U}_S$ is the Fourier transform of U_S. The Fourier plane in Fig. 2.3 illustrates these four terms. The first term is the result of the spatially uniform reference light which resides in the center the Fourier plane. The second term is the autocorrelation of the signal complex-optical field in the pupil plane, which results in a weak chat function (cf. App. A). The third term is the signal complex-optical field in the pupil plane, $\widetilde{U}_S$, scaled by A_R^*, and centered at $\left(\frac{x_R}{\lambda z_I}, \frac{y_R}{\lambda z_I}\right)$. It is spatially shifted away from DC due to the tilt of off-axis reference light and the shifting property of the Fourier transform. The fourth term is conjugate of the third term, which arises from the Hermitian symmetry of the Fourier transform for real-valued functions.

To isolate $\widetilde{U}_S$, a digital window is used as described as

$$w\left(f_x, f_y\right) = \operatorname{circ}\left(2 f_x\, q_I, 2 f_y\, q_I\right), \tag{2.14}$$

where circ is the circle function (cf. App. A) and q_I is the image-plane sampling quotient. The image-plane sampling quotient is defined as

$$q_I = \frac{\lambda z_I}{p d_p}, \tag{2.15}$$

where d_p is the pupil diameter. q_I has various physical descriptions, but the most applicable here, is q_I corresponds to the number of pupil widths across the Fourier

plane. Therefore, typical values range from $q_I = 2.5 - 3$.

Next, $\widehat{\widetilde{U}}_S$ is obtained by shifting the Fourier plane and applying our window $w(f_x, f_y)$ as

$$\begin{aligned}\widehat{\widetilde{U}}_S(f_x, f_y) =& w(f_x, f_y)\, D_H^+\left(f_x + \frac{x_R}{\lambda z_I}, f_y + \frac{y_R}{\lambda z_I}\right) \\ =& g_{A/D}\eta_q\sqrt{\eta_t\eta_p\eta_s}\frac{t_i p^2}{h\nu}A_R^*\widetilde{U}_S(f_x, f_y) \\ &+ g_{A/D}\frac{\sigma_I}{\sqrt{2}}\,\mathcal{N}_k(f_x, f_y),\end{aligned} \tag{2.16}$$

where σ_I^2 is the compressed-noise variance for the off-axis IPRG ($\sigma_I^2 = \frac{\pi}{4q_I^2}\sigma_n^2$) and η_s is the spatial integration efficiency. Note that the factor of $\frac{\pi}{4q_I^2}$ is the ratio of windowed area to the total Fourier plane area. η_s is added to account for the pixel integration in Eq. (2.4), which results in the 2D-sinc function in the Fourier plane,

$$\eta_s = \left\langle w(f_x, f_y)\,\mathrm{sinc}^2\left(p\left[f_x + \frac{x_R}{\lambda z_I}\right], p\left[f_y + \frac{y_R}{\lambda z_I}\right]\right)\right\rangle, \tag{2.17}$$

where $\langle\cdot\rangle$ is the spatial average. Depending on pupil size and location, typical values are $\approx 64\%$ for a $q_i = 2$ and a pupil centered at $(p/4, p/4)$ in the Fourier plane. Note that the sinc is the approximation of the pixel modulation transfer function (MTF).

Lastly, to obtain the estimated-signal complex-optical field, $\widehat{U}_S$, a discrete Fourier transform, $\mathcal{DFT}$, is performed on $\widehat{\widetilde{U}}_S$ to arrive at

$$\begin{aligned}\widehat{U}_S(x, y) =& \mathcal{DFT}\left\{\widehat{U}_P(f_x, f_y)\right\} \\ =& g_{A/D}\eta_q\sqrt{\eta_t\eta_p\eta_s}\frac{t_i p^2}{h\nu}A_R^* U_S(x, y) \\ &+ g_{A/D}\frac{\sigma_I(x, y)}{\sqrt{2}}\,\mathcal{N}_k(x, y)\end{aligned} \tag{2.18}$$

which is in units of DN. Note that the grid dimensions do not change between planes to preserve the energy per unit area.

2.1.3 Signal-to-Noise Ratio

The power definition of the signal-to-noise ratio, S/N, is used, such that

$$S/N\left(x,y\right)=\frac{\mathcal{E}\left\{\left|\widehat{U}_S\left(x,y\right)\right|^2\right\}}{\mathcal{V}\left\{\widehat{U}_S\left(x,y\right)\right\}}, \tag{2.19}$$

where $\mathcal{E}\{\cdot\}$ is the expectation operator and $\mathcal{V}\{\cdot\}$ is the variance operator. Using Eq. (2.6), (2.7), and (2.18), the signal magnitude-squared expectation value becomes

$$\mathcal{E}\left\{\left|\widehat{U}_S\left(x,y\right)\right|^2\right\}=g_{A/D}^2\eta_t\eta_s\eta_p\eta_q^2\ \overline{m}_S\left(x,y\right)\overline{m}_R. \tag{2.20}$$

The variance is the noise of Eq. (2.18) and becomes

$$\mathcal{V}\left\{\widehat{U}_S\left(x,y\right)\right\}=g_{A/D}^2\frac{\pi}{4q_I^2}\sigma_n^2\left(x,y\right). \tag{2.21}$$

Combining Eq. (2.9) into Eq. (2.21), the SNR becomes

$$S/N\left(x,y\right)=\eta_T\frac{4q_I^2}{\pi}\frac{\overline{m}_S\left(x,y\right)\overline{m}_R}{\overline{m}_R+\overline{m}_S\left(x,y\right)+\grave{\sigma}_r^2}, \tag{2.22}$$

where η_T is the total efficiency and $\grave{\sigma}_r^2=\sigma_r^2/\eta_q$. With the strong reference assumption, $\overline{m}_R\gg\overline{m}_s(x,y)$ and $\overline{m}_R\gg\grave{\sigma}_r^2$, S/N reduces to

$$S/N\left(x,y\right)\approx\eta_T\frac{4q_I^2}{\pi}\overline{m}_S\left(x,y\right), \tag{2.23}$$

which means the SNR is only dependent on the signal strength. With the efficiencies present here, the total system efficiency becomes

$$\eta_T=\eta_s\eta_p\eta_t\eta_q. \tag{2.24}$$

2.2 Optical Turbulence

Optical turbulence in the earth's atmosphere generates eddies, which have varying refractive indices, and in turn, induces aberrations along the optical path because the light rays travel slightly different paths. Andrei Kolmogorov was the first to statistically describe the spectrum of the eddy sizes [30] and from that, optical metrics for the turbulence-induced distortions were developed by Fried [31, 32] and others. Three optical metrics of concern are the Fried parameter or coherence length (r_0), log-amplitude variance or Rytov number (σ_χ^2), and isoplanatic angle (θ_0). The following equations [33, 34] show how these parameters scale with wavelength (λ), turbulence strength (C_n^2), along the optical path (z), and range (L):

$$r_0 = \left[0.423k^2 \int_0^L C_n^2(z) \left(\frac{z}{L}\right)^{5/3} dz\right]^{-3/5}, \tag{2.25}$$

$$\sigma_\chi^2 = 0.563k^{7/6} \int_0^L C_n^2(z) \left(\frac{z}{L}\right)^{5/6} (L-z)^{5/6} dz, \tag{2.26}$$

$$\theta_0 = \left[2.91k^2 \int_0^L C_n^2(z) (L-z)^{5/3} dz\right]^{-3/5}, \tag{2.27}$$

where C_n^2 is refractive index turbulence structure constant (e.g. strength of turbulence), k is the wave number given by $\frac{2\pi}{\lambda}$, and L is the total distance of the optical path. Note that Eq. 2.25-2.27 are for a spherical wave.

2.2.1 Fried's coherence length r_0

Fried's coherence length is the resolution limiting aperture size. If $r_0 = 10\,\text{cm}$, then the imaging system has the effective resolution as a 10 cm aperture and a larger aperture doesn't improve resolution. As shown in Eq. (2.25), r_0 is proportional to wavelength, $r_0 \propto \lambda^{6/5}$, e.g. the longer the wavelength, the better the r_0. It is also distance dependent, and therefore, weak turbulence over a long path can yield a small

r_0. In terms of adaptive optics correction, if the aperture diameter (d_p) is less than four times r_0, only low-order correction is required, e.g. tip and tilt. For $d_p/r_0 > 4$, then higher order correction is needed, e.g. with something like a deformable mirror.

2.2.2 Rytov number σ_χ^2

The Rytov number is the log-amplitude variance which quantifies the amount of scintillation experienced by the optical field. From Eq. (2.26), it is inversely proportional to wavelength, $\sigma_\chi^2 \propto \lambda^{-7/6}$, and scales with turbulence strength, C_n^2, and optical path distance. Scintillation redistributes the optical field energy unpredictably and produces branch points, where there are nulls in the irradiance. Branch points originate around $\sigma_\chi^2 \approx .25$, where some classify as the origin of strong turbulence [35], and increase as the Rytov number increases. Additionally, branch cuts arise between the branch points where there is a 2π discontinuity in the phase. Figure 2.4 shows a simulated point source numerically propagated through weak and strong turbulence. The increase in scintillation is seen in the irradiance between Fig. 2.4 (a) and (b). Additionally, the wrapped phase in Fig. 2.4 (d) is less smooth than in Fig. 2.4 (c).

2.2.3 Isoplanatic angle θ_0

An imaging system is isoplanatic when it is a linear shift-invariant system [24], meaning the system experiences proportional shift when the input is shifted. For example, when a star streaks across a telescopes view, the imaged star also streaks in the corresponding trajectory. The isoplanatic angle is the imaging system's maximum FOV for which it is still isoplantatic. From Eq. (2.27), it is proportional to wavelength and decreases as optical path increases. When the imaging system is isoplanatic with turbulence, which is typically the case with weak turbulence, the phase aberrations can be estimated and corrected at the pupil of the imaging system. However, the

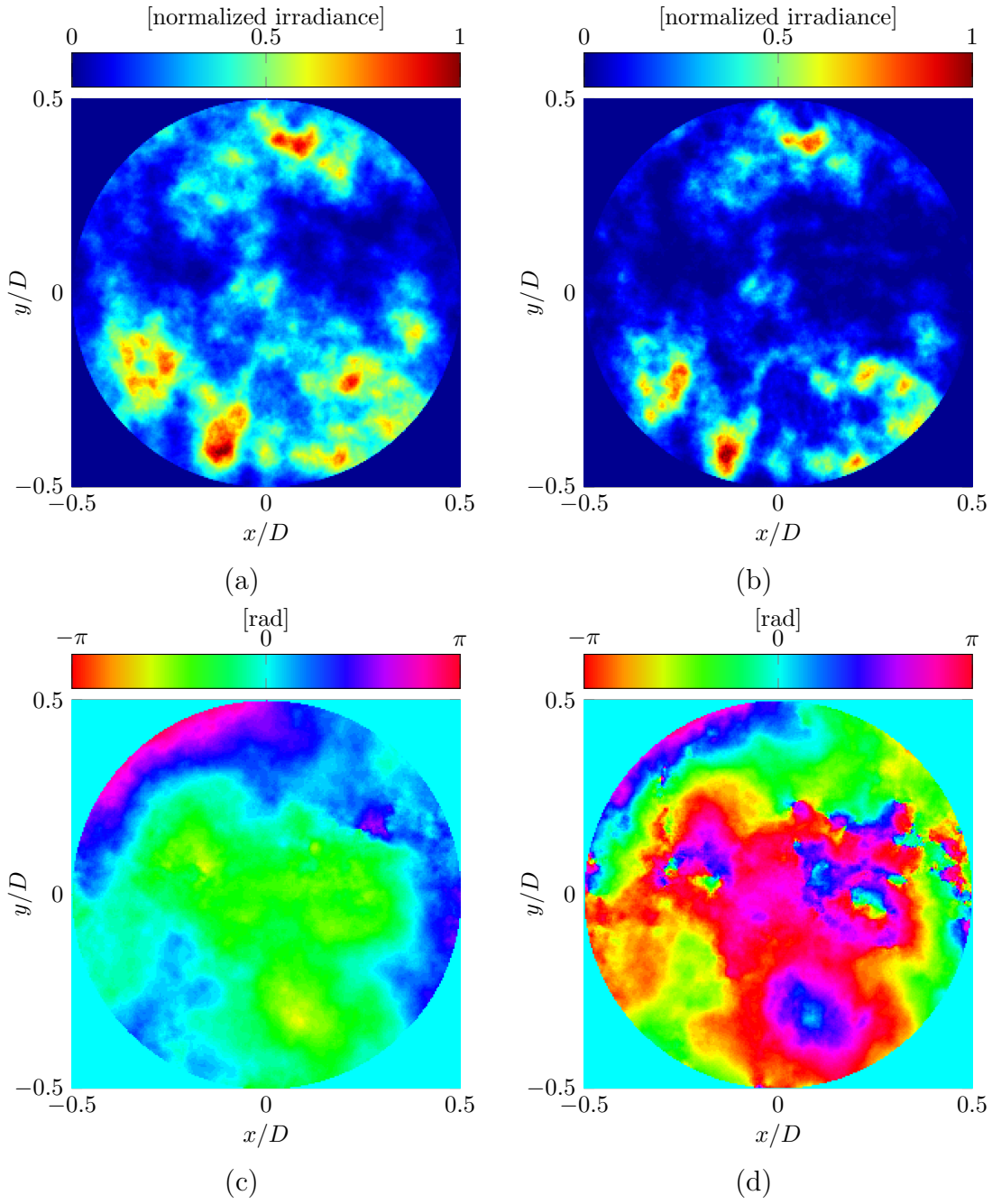

Figure 2.4. Examples of a simulated point source numerically propagated 7.5 km through weak turbulence ($C_n^2 = 10^{-15}$, $r_0 = 9.5\,cm$, and $\sigma_\chi^2 = 0.135$) [(a) and (b)] and strong turbulence ($C_n^2 = 3 \times 10^{-15}$, $r_0 = 5.1\,cm$, and $\sigma_\chi^2 = 0.404$) [(c) and (d)] with a 30 cm diameter aperture.

isoplanatic angle becomes smaller than the FOV of the imaging system, the phase aberrations need to be estimated and corrected along the optical path in order to

correct for the entire FOV. Otherwise, only an isoplanatic patch (e.g., an area of the image that is isoplanatic) of the image would be corrected, provided you could zoom in on that region of interest and locally apply the correction.

2.2.4 Deep turbulence

The term deep turbulence (also called distributed-volume turbulence) is used to describe strong turbulence that is distributed along the optical path and causes the imaging system to be anisoplanatic. In scenarios that experience strong turbulence over a very short path (e.g. aero-optic effects since the turbulence effects are nearby the pupil and not along the path), the system can still be isoplanatic. However, over a long path of turbulence, the light from different points on the imaged object experiences different turbulence along the path. Therefore, phase estimation and correction is needed along the optical path, not just at the pupil.

2.3 Temporal coherence

For DH tactical applications, the hologram is formed because of the MO laser's temporal coherence. Goodman states that

> "... the concept of temporal coherence has to do with the ability of a light wave to interfere constructively and destructively with a delayed version of itself.". [36]

With that said, the temporally-dependent hologram irradiance, i_H, is

$$\begin{aligned} i_H(t,\tau) = &|U_R(t)|^2 + |U_S(t+\tau)|^2 \\ &+ U_R^*(t)U_S(t+\tau) + U_R(t)U_S^*(t+\tau), \end{aligned} \tag{2.28}$$

where τ is the time delay between the signal and reference. The fringe visibility is a physical metric which measures how well the signal and reference interfere. Using

Eq. (2.28) and assuming $i_H(t,\tau)$ is only dependent on τ and independent of t (i.e., the time origin), the fringe visibility, $\mathcal{V}$, is defined as

$$\mathcal{V}(\tau) = \frac{i_H^{max}(\tau) - i_H^{min}(\tau)}{i_H^{max}(\tau) + i_H^{min}(\tau)}, \tag{2.29}$$

where $i_H^{max}(\tau)$ is the peak of the hologram fringe and $i_H^{min}(\tau)$ is the trough of the hologram fringe [36]. $\mathcal{V}(\tau)$ is a normalized metric, so $\mathcal{V}(\tau)$ ranges from zero to one. This provides a physical metric for the interference. However, this definition of $\mathcal{V}(\tau)$ is dependent on the signal and reference amplitudes.

Another function for coherence is the normalized complex degree of coherence, $\gamma(\tau)$, [37] and is defined in terms of the reference and signal complex-optical fields as

$$\gamma(\tau) = \frac{\langle U_R(t)^*(t) U_S(t+\tau)\rangle}{\langle U_R(0) U_S(0)\rangle}, \tag{2.30}$$

where $\langle\cdot\rangle$ is the expectation value, $\gamma(\tau) = 1$ represents ideal coherence and $\gamma(\tau) = 0$ represents no coherence. Note that Eq. (2.30) is an autocorrelation if the MO laser is assumed to be at least wide-sense stationary since γ is only dependent on τ. Additionally, $\mathcal{V}(\tau)$ is related to $\gamma(\tau)$ via

$$\mathcal{V}(\tau) = \frac{2|U_S||U_R|}{|U_S|^2 + |U_R|^2}|\gamma(\tau)|, \tag{2.31}$$

and $\mathcal{V}(\tau) = |\gamma(\tau)|$ when $|U_S|^2 = |U_R|^2$ [36]. An important property of $\gamma(\tau)$ is that it is a Fourier transform pair with the normalized power spectral density (PSD), $\widehat{\mathcal{G}}(\nu)$, due to the Wiener-Khinchin theorem [36]. The PSD, $\mathcal{G}(\nu)$, represents the frequency content or spectrum of the MO laser and is normalized so that $\int_0^\infty \widehat{\mathcal{G}}(\nu)d\nu = 1$. Often $\widehat{\mathcal{G}}(\nu)$ is known or well approximated by a lineshape, such as a Gaussian, and therefore, $\gamma(\tau)$ is also a Gaussian.

Two common metrics often used to characterize the coherence of MO laser is the coherence time, τ_c, and the coherence length, ℓ_c. Here, Mandel's definition of τ_c is used [38], which is defined as

$$\tau_c = \int_{-\infty}^{\infty} |\gamma(\tau)|^2 \, d\tau, \tag{2.32}$$

and $\ell_c = c\,\tau_c$, where c is the speed of light. Because of Eq. (2.32) and the the Wiener-Khinchin theorem, τ_c and ℓ_c are inversely proportional to the full-width at half-max, $\Delta\nu$, of $\mathcal{G}(\nu)$. With this inverse relationship, the narrower the $\Delta\nu$ of the MO laser, the longer τ_c and ℓ_c. Figure 2.5 illustrates the loss of coherence versus a normalized τ, where $|\gamma(t_c)| = 0.21$. For DH, the approximated range of the system due to temporal coherence is often considered to be $\ell_c/2$ so that $\tau < \tau_c$.

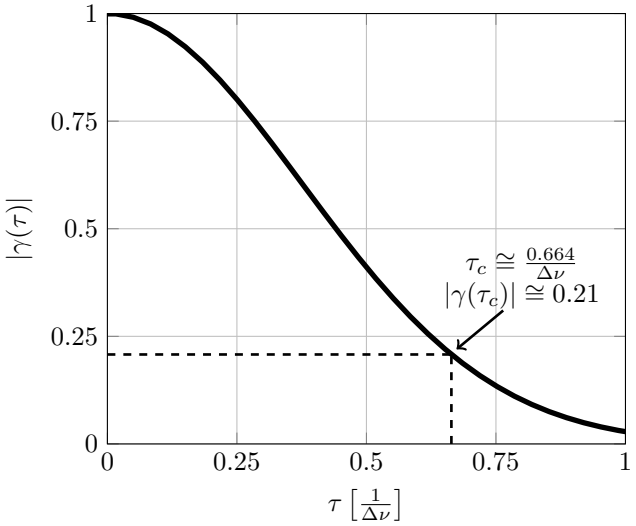

Figure 2.5. The magnitude of the normalized complex-degree of coherence ($|\gamma|$) vs a normalized time delay (τ) for a Gaussian power spectral density

III. Deep-turbulence wavefront sensing using digital holography in the on-axis phase shifting recording geometry with comparisons to the self-referencing interferometer

The contents of this chapter, Appendix B, and Appendix C were published in the *Digital Holography and 3-D Imaging* feature issue of *Applied Optics*, vol. 58, no. 5 on January 15, 2019 [39].

In this paper, we study the use of digital holography in the on-axis phase shifting recording geometry for the purposes of deep-turbulence wavefront sensing. In particular, we develop closed-form expressions for the field-estimated Strehl ratio and signal-to-noise ratio for three separate phase-shifting strategies—the four-, three-, and two-step methods. These closed form expressions compare favorably with our detailed wave-optics simulations, which propagate a point-source beacon through deep-turbulence conditions, model digital holography with noise, and calculate the Monte-Carlo averages associated with increasing turbulence strengths and decreasing focal-plane array sampling. Overall, the results show the four-step method is the most efficient phase-shifting strategy and deep-turbulence conditions only degrade performance with respect to insufficient focal-plane array sampling and low signal-to-noise ratios. The results also show the strong-reference beam from the local oscillator provided by digital holography greatly improves performance by 10's of dB when compared with the self-referencing interferometer.

3.1 Introduction

Holography has a rich history in applications involving long-range imaging [4] and wavefront reconstruction [1]. In practice, we can use these applications in concert to overcome atmospheric distortions and low-signal levels [3, 40, 41]. With the advent of robust focal-plane arrays (FPAs), researchers began to measure and store holo-

grams digitally [2]. In an effort to characterize the atmosphere [32, 42, 43], this early research provided the framework needed for deep-turbulence wavefront sensing using digital holography.

Many applications, such as free-space laser communications, involve propagation paths which experience deep-turbulence conditions. Also known as distributed-volume turbulence or strong turbulence, deep turbulence arises from atmospheric aberrations being distributed along the propagation path. Given spatially coherent light, this outcome gives rise to time-varying constructive and destructive interference. Known as scintillation, this phenomena typically hinders wavefront-sensing performance. While all atmospheric-optical paths experience scintillation to some degree, the effects of scintillation are often negligible for the vertical-propagation paths (e.g., those associated with ground-based telescopes [12], which experience weak-turbulence conditions) and often appreciable for the horizontal-propagation paths (e.g., those associated with long-range imaging systems [18], which experience deep-turbulence conditions).

Traditional wavefront-sensing methods use localized irradiance measurements to estimate phase gradients [e.g., the Shack-Hartmann wavefront sensor (SHWFS)]. Note that these traditional methods enable near-diffraction-limited optical systems [12]; however, performance degrades substantially in the presence of strong scintillation. For all intents and purposes, strong scintillation occurs when, for example, the spherical-wave log amplitude variance, which gives a measure for the amount of scintillation, becomes greater than 0.2 [44, 45]. Given strong scintillation, branch points arise in the continuous-phase function, in particular, where there are amplitude nulls in the real and imaginary parts of the complex-optical field [13]. For gradient-based wavefront sensors, like the SHWFS, these amplitude nulls cause the wavefront sensor to measure and reconstruct noise. The branch points also add a

rotational component to the phase function that gets mapped to the null space of a least-squares phase reconstructor, which manipulates the estimated phase gradients into a continuous-phase function. In turn, traditional wavefront-sensing methods do not perform well in deep-turbulence conditions.

We can alternatively use interferometric wavefront-sensing methods, such as the point-diffraction interferometer [46] and self-referencing interferometer (SRI) [47], to obtain an estimate of the complex-optical field. This estimate gives us access to the wrapped-phase function which contains both the irrotational and rotational phase components [13]. As such, we can use a branch-point-tolerant phase reconstructor to buy back performance when in the presence of strong scintillation [48]; however, this approach has yet to be demonstrated beyond a scaled-laboratory environment [49]. This last detail is most likely due to additional constraints caused by deep-turbulence conditions. For example, with an SRI, the received light is split to create a spatially filtered reference beam. Typically, researchers perform this spatial filtering by coupling the split received light into a single-mode optical fiber. When in the presence of strong scintillation, which arises with deep-turbulence conditions, this coupling results in efficiency losses and creates low signal-to-noise ratios (SNRs) that quickly lead to performance degradations [50].

To overcome the performance degradations caused by deep-turbulence conditions, we can instead use digital holography which is another interferometric wavefront-sensing method. In practice, digital holography is able to resolve the branch points associated with strong scintillation, since it provides us with an estimate of complex-optical field and access to the wrapped-phase function which contains both the rotational and irrotational phase components [13]. Furthermore, digital holography is robust against the amplitude nulls caused by strong scintillation. The use of a strong-reference beam from a local oscillator (LO) allows us to approach the shot-

noise limit, since the signal beam is boosted above the read-noise floor of the FPA [23]. With these benefits in mind, this paper evaluates the performance of digital holography in the on-axis phase shifting recording geometry (PSRG), as shown in Figs. 1 and 2. This paper, in turn, provides the necessary analysis needed to design and conduct future deep-turbulence experiments using digital holography in the on-axis PSRG. These experiments shall investigate both open- and closed-loop performance in scaled-laboratory and field environments. Such experiments shall also include additional factors not investigated in this paper like reference-beam nonuniformity, detector nonlinearities, laser practicalities, and vibration resistance.

It is worth mentioning that this paper builds upon the noiseless analysis contained in a recent conference proceeding by Thornton *et al.* [51]. Specifically, this paper develops and verifies the use of closed-form expressions for the SNR and field-estimated Strehl ratio with respect to the on-axis PSRG operating with three separate phase-shifting strategies—the four-, three-, and two-step methods [52, 53]. Using detailed wave-optics simulations, which propagate a point-source beacon through deep-turbulence conditions, model digital holography with noise, and calculate the Monte-Carlo averages associated with increasing turbulence strengths and decreasing focal-plane array sampling, the analysis shows the four-step method is the most efficient phase-shifting strategy. Furthermore, deep-turbulence conditions only degrade performance with respect to insufficient FPA sampling and low SNRs.

It is also worth mentioning that this paper is a companion paper to the analysis presented by Spencer *et al.* [20] and Banet *et al.* [21] with respect to digital holography in the off-axis image plane recording geometry (IPRG) and off-axis pupil plane recording geometry (PPRG), respectively. In practice, the off-axis IPRG and off-axis PPRG indirectly obtains an estimate of the complex-optical field from Fourier transformations and digital-signal-processing techniques (i.e., filtering the 2D spectrum of

the digital hologram recorded with the FPA). Conversely, the on-axis PSRG directly obtains an estimate of the complex-optical field from multiple digital holograms being recorded on one or more FPA(s) and straightforward calculations [23].

In what follows, this paper develops closed-form expressions for two performance metrics (cf. Section 3.2), the SNR and field-estimated Strehl ratio, and verifies their use with detailed wave-optics simulations, which again, propagate a point-source beacon through deep-turbulence conditions, model digital holography with noise, and calculate the Monte-Carlo averages associated with increasing turbulence strengths and decreasing focal-plane array sampling. (cf. Section 3.3). This outcome demonstrates the on-axis PSRG is another valid recording geometry for deep-turbulence wavefront sensing. Before moving onto the next section, it is important to note that digital holography in the on-axis PSRG and the SRI are similar in design, except for the origin of the reference beam. Therefore, this paper also includes a comparison between digital holography in the on-axis PSRG and the SRI to show the benefits of using a strong-reference beam for applications involving deep-turbulence conditions (cf. Section 3.4).

3.2 Development of closed-form expressions for two performance metrics

This section provides an overview of the optical setup used for digital holography in the on-axis PSRG. It also develops estimate and noise models for three separate phase-shifting strategies—the four-, three-, and two-step methods. We then use the models to develop closed-form expressions for the SNR and field-estimated Strehl ratio. In the ensuing sections, we verify the use of these performance metrics via wave-optics simulations and then use them to compare the performance of digital holography in the on-axis PSRG to the performance of an SRI, both using the four-step method (i.e., the most efficient method).

3.2.1 Optical Setup

As shown in Fig. 3.1, to realize digital holography in the on-axis PSRG, we split a master oscillator (MO) laser into two optical legs. The first leg flood illuminates an unresolved, ball-bearing object creating a point-source beacon. Then, the reflected spherical wave propagates through deep-turbulence conditions and becomes the signal beam U_S collimated in a pupil. The second leg creates a LO that gives rise to a reference beam U_R. After the reference and signal beams pass through the phase shifting optics (PSO), we use the interference of light to create multiple holograms and record the resulting hologram irradiances $i_H^{(\delta)}$ on the FPA(s).

With Fig. 3.1 in mind, we show some of the details of the PSO in Fig. 3.2 for the four-step method. As shown in Fig. 3.2, the purpose of the PSO is to obtain the desired phase shift δ on the reference beam for the recorded holograms. Note that, in practice, a phase shift of π occurs with reflections from the mirrors (M) and 50/50 beam splitters (BS) when the light is incident on the side favoring the black dot. The reflected light incident on the opposing side of the black dot does not incur a phase shift [25]. Additionally, we obtain a $\pi/2$-phase shift at the quarter-wave plate (QWP). Aggregating these phase shifts for the reference and signal beams results in the four holograms shown in Fig. 3.2 and has been demonstrated in hardware [54, 55].

There are two more items to consider with respect to Fig. 3.2: optical-path length and polarization. As shown, we do not draw the optical-path lengths to scale, and in a real system, we would want to match the optical-path lengths to ensure the proper phase shifts and minimize any losses in fringe visibility due to vibrations. Also note that we would need to image the signal and reference beams onto the FPA(s) to record the resulting hologram irradiances. To do so, we would need to employ relay optics (not shown here) to create conjugate pupil planes at the FPA(s), so that we conserve the phase of the signal and reference beams in forming our holograms. With

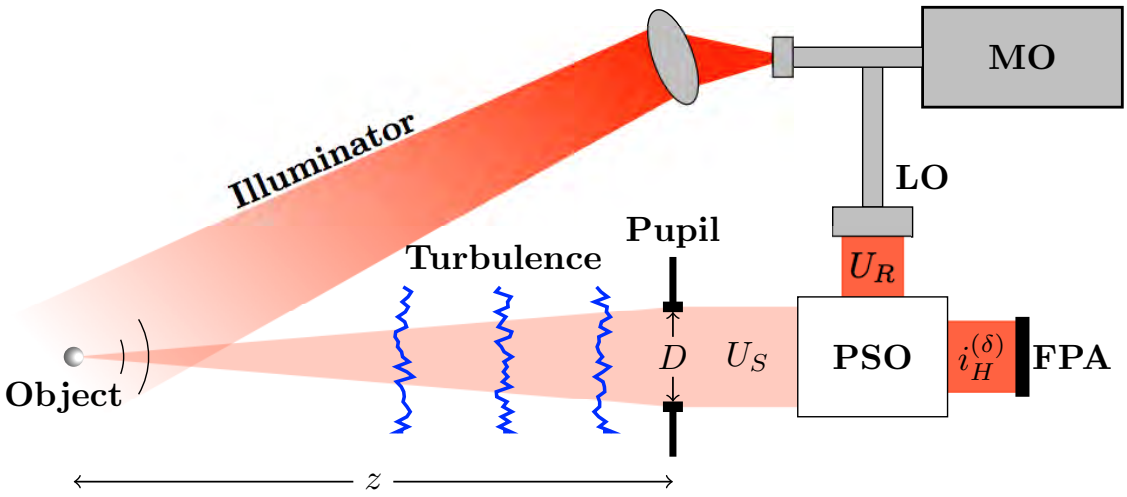

Figure 3.1. An illustration of digital holography in the on-axis PSRG. Note that we need phase-shifting optics (PSO) to implement our phase-shifting strategy (cf. Fig. 3.2).

respect to the polarization concerns, maximum fringe visibility only occurs when the reference and signal beam's polarization states match. However, in a real system, the reference beam's polarization state is probably different than the signal beam's polarization state due to rough-surface scattering from the object. Therefore, also not shown here are the polarization optics we would need to use to maximize the fringe visibility in our holograms. Moving forward in the analysis, we simply assume that we match the polarization states and that we are only dealing with absolute phase shifts (e.g., there are no piston errors in the phase shifts).

With the above assumptions in mind, the on-axis PSRG can employ different phase-shifting strategies to calculate the complex-optical field [52, 53]. In this paper, we analyze three methods, namely, the four-, three-, and two-step methods. As previously stated, we show the four-step method's PSO in Fig. 3.2. The three- and two-step methods use similar PSO with some exceptions. In particular, we can modify the fraction of transmitted/reflected light off the first beam splitter encountered for the reference and signal beams to ensure equal amounts of light for each hologram. We can also exchange the final beam splitters with beam-combining optics to remove

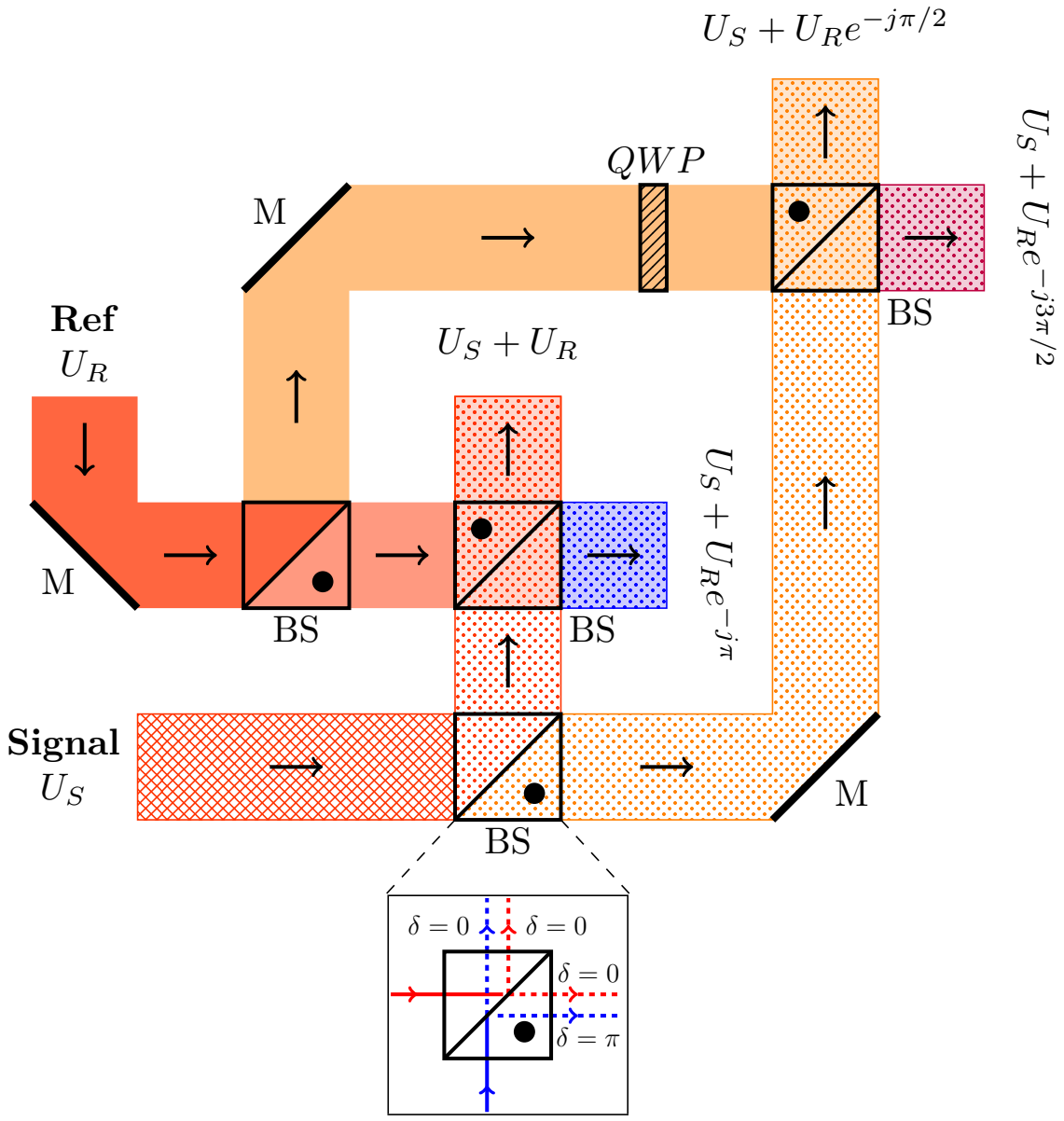

Figure 3.2. An example of the PSO needed for the four-step method. This example also contains an illustration of the directional dependence of the π-phase shift upon reflection from a beam splitter (BS).

the unnecessary measurements while preserving the signal beam. In so doing, we only divide the signal beam by the number of holograms desired, and the holograms make use of corresponding strong-reference beams to maximize SNR.

3.2.2 Estimate model

Provided Figs. 3.1 and 3.2, the hologram irradiances $i_H^{(\delta)}$ take the following form:

$$\begin{aligned} i_H^{(\delta)} &= \left| U_S + U_R\ e^{-j\delta} \right|^2 \\ &= |U_S|^2 + |U_R|^2 + U_S U_R^*\ e^{j\delta} + U_S^* U_R\ e^{-j\delta}, \end{aligned} \tag{3.1}$$

where δ is again the desired reference-beam phase shift. Throughout the analysis, it is important to note that we assume, by choice, a spatially uniform reference beam. With increments of $\pi/2$ phase shifts, the corresponding $i_H^{(\delta)}$ become

$$\begin{aligned} i_H^{(0)} &= |U_S|^2 + |U_R|^2 + U_S U_R^* + U_S^* U_R \\ i_H^{(\pi/2)} &= |U_S|^2 + |U_R|^2 + jU_S U_R^* - jU_S^* U_R \\ i_H^{(\pi)} &= |U_S|^2 + |U_R|^2 - U_S U_R^* - U_S^* U_R \\ i_H^{(3\pi/2)} &= |U_S|^2 + |U_R|^2 - jU_S U_R^* + jU_S^* U_R. \end{aligned} \tag{3.2}$$

Here, we replace the superscript δ with the appropriate reference-phase shift and * denotes complex conjugate.

Provided Eq. (3.2), we can perform algebraic manipulations to isolate the signal beam U_S [52]. For each of the phase-shifting strategies considered in this paper, we arrive at the following relationships:

$$4U_R^* U_S = \left(i_H^{(0)} - i_H^{(\pi)} \right) - j \left(i_H^{(\pi/2)} - i_H^{(3\pi/2)} \right) \tag{3.3}$$

for the four-step method,

$$4U_R^* U_S = (1+j) \left(i_H^{(0)} - i_H^{(\pi/2)} \right) + (j-1) \left(i_H^{(\pi)} - i_H^{(\pi/2)} \right) \tag{3.4}$$

for the three-step method, and

$$2U_R^* U_S = \left(i_H^{(0)} - |U_S|^2 - |U_R|^2\right) - j\left(i_H^{(\pi/2)} - |U_S|^2 - |U_R|^2\right) \tag{3.5}$$

for the two-step method. Notice that the two-step method also requires that we know the irradiances associated with the signal and reference beams (cf. Eq. 3.5). To obtain the reference-beam irradiance, we would need to add a way to monitor the reference beam. This addition might seem excessive at first; however, in a real system, this monitoring would also allow us to maintain the strong-reference beam assumption and avoid pixel saturation on the FPA(s). To obtain the signal-beam irradiance, we can make use of the following relationship derived by Poon and Liu [56]:

$$\begin{aligned} 2\left|U_S\right|^2 = \; & i_H^{(0)} + i_H^{(\pi/2)} - \left\{\left[2\left|U_R\right|^2 + i_H^{(0)} + i_H^{(\pi/2)}\right]^2 - \right. \\ & \left. 2\left[4\left|U_R\right|^4 + \left(i_H^{(0)}\right)^2 + \left(i_H^{(\pi/2)}\right)^2\right]\right\}^{1/2} . \end{aligned} \tag{3.6}$$

This relationship helps our efforts since the low-signal levels associated with deep-turbulence conditions make the signal-beam irradiance hard to monitor.

With Eqs. (3.1-3.6) in mind, we can record the hologram irradiances $i_H^{(\delta)}$ with a FPA, which performs a pixel-by-pixel integration [23]. Thus, for a FPA with $M \times N$ pixels,

$$\begin{aligned} & \widehat{i}_H^{(\delta)}\left(nx_p, my_p\right) = \\ & \frac{1}{w_x w_y} \int\!\!\int_{-\infty}^{\infty} i_H^{(\delta)}(x', y') \operatorname{rect}\left(\frac{x' - nx_p}{w_x}\right) \operatorname{rect}\left(\frac{y' - my_p}{w_y}\right) dx' dy' \; , \end{aligned} \tag{3.7}$$

where m and n are the FPA pixel indices from $m = 1$ to M and $n = 1$ to N, x_p and y_p are the pixel pitches, w_x and w_y are the pixel widths, and

$$\text{rect}(x) = \begin{cases} 1 & 0 \leq |x| < 0.5 \\ 0.5 & |x| = 0.5 \\ 0 & |x| > 0.5 \end{cases} \tag{3.8}$$

is the rectangle function. Since the FPA detects photoelectrons [25, 28], we determine the per-pixel mean number of hologram photoelectrons $\overline{m}_H(nx_p, my_p)$ as

$$\begin{aligned} \overline{m}_H^{(\delta)}(nx_p, my_p) =& \frac{\eta\tau w_x w_y}{h\ \nu} \widehat{i}_H^{(\delta)}(nx_p, my_p) \\ =& \frac{\eta\tau}{h\ \nu} i_H^{(\delta)}(nx_p, my_p) \\ & * * \text{rect}\left(\frac{nx_p}{w_x}\right) \text{rect}\left(\frac{my_p}{w_y}\right), \end{aligned} \tag{3.9}$$

where η is the quantum efficiency, τ is the integration time, h is Planck's constant, ν is the optical frequency, and $**$ denotes 2D convolution. Similarly, we determine the per-pixel mean number of reference photoelectrons $\overline{m}_R$ as

$$\overline{m}_R = \frac{\eta\tau w_x w_y}{h\nu} |U_R|^2, \tag{3.10}$$

where again, we drop the pixel coordinates to denote spatial uniformity. The per-pixel mean number of signal photoelectrons $\overline{m}_S(nx_p, my_p)$ then becomes

$$\begin{aligned} \overline{m}_S(nx_p, my_p) =& \frac{\eta\tau}{h\nu} |U_S(nx_p, my_p)|^2 \\ & * * \text{rect}\left(\frac{nx_p}{w_x}\right) \text{rect}\left(\frac{my_p}{w_y}\right). \end{aligned} \tag{3.11}$$

We will use these last-two relationships in the coming noise-model analysis.

Provided the right-hand sides of Eqs. (3.3 - 3.5), which depend on the measured hologram irradiances, $i_H^{(\delta)}$, we can use Eq. (3.9) to obtain a generic expression for the signal-beam estimate, $\widehat{U}_S^{(s)}$, in terms of the left-hand sides of Eqs. (3.3 - 3.5). In particular,

$$\begin{aligned}\widehat{U}_S^{(s)}\left(nx_p, my_p\right) =& \frac{\kappa}{\sqrt{s}}\frac{\eta\tau}{h\nu}U_R^* U_S\left(nx_p, my_p\right) \\ & * * \operatorname{rect}\left(\frac{nx_p}{w_x}\right)\operatorname{rect}\left(\frac{my_p}{w_y}\right),\end{aligned} \tag{3.12}$$

where s is the number of shifts or measurements required by the phase-shifting strategy (e.g., $s = 4$, 3, and 2 for the four-, three-, and two-step methods, respectively) and κ is a phase-shifting constant, such that $\kappa = 4$ for the four- and three-step methods and $\kappa = 2$ for the two-step method (cf. the left-hand sides of Eqs. (3.3) - (3.5). In using Eq. (3.12) along with Eqs. (3.3) - (3.5), we define the magnitude of signal beam at the pupil before the PSO (hence the exclusion of s and κ in Eq. (3.11), so that we can easily compare the three methods. Also note that we define the magnitude of the reference beam at the FPA(s), since we can easily adjust the strength of the reference beam using the LO (cf. Figs. 3.1 and 3.2). As such, we are left with a straightforward calculation to obtain the wrapped-phase function from an estimate of the complex-optical field. We illustrate this process for the four-step method in Fig. 3.3.

3.2.3 Noise model

Moving forward in the analysis, we would like to account for the effects of shot noise and read noise. For this purpose, we assume that the shot noise results from the random arrival times of the photons that are incident on the FPA, and that the read noise results from the read-out integrated circuitry of the FPA. We also assume that

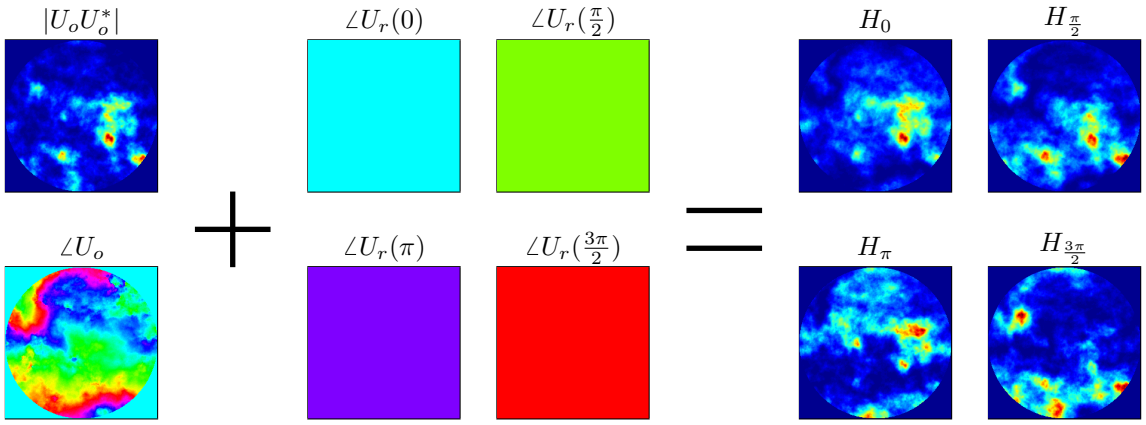

Figure 3.3. An illustration of how digital holography in the on-axis PSRG allows us to access the wrapped-phase function. Here, we use the interference of light to create multiple holograms by mixing a phase-shifted reference beam with a signal beam. Note that the number of shifts or measurements required by the phase-shifting strategy is dependent on the phase-shifting method being used (here, we illustrate the four-step method). After we record the hologram irradiances with a FPA, we perform a straightforward calculation to obtain the wrapped-phase function from an estimate of complex-optical field [cf. Eq. (3.12) along with Eqs. (3.3) - (3.5)].

the shot noise follows a Poisson distribution, whereas read noise follows a Gaussian distribution.

For a Poisson-distributed random process, the mean is equal to the variance [25]. In this paper [cf. Eqs. (3.10) and (3.11)], the mean is equal to the sum of the per-pixel mean number of photoelectrons from the signal and reference beams, $\overline{m}_S$ and $\overline{m}_R$, respectively. Here, we drop the FPA coordinates to denote the average over the entire detection area. Since we set $\overline{m}_R$ to 75% of pixel-well depth of the FPA, we assume that $\overline{m}_R \gg \overline{m}_S$ and that the mean number of hologram photoelectrons varies little from pixel to pixel because of the strong-reference beam ($\overline{m}_H \approx \overline{m}_R$). In turn, the Poisson-distributed shot noise follows a Gaussian distribution (to a good approximation when $\overline{m}_R \gg 1$) with variance $\overline{m}_R + \overline{m}_S \approx \overline{m}_R$. Armed with these assumptions, we can add the variances for each Gaussian-distributed random process and arrive at the noise variance σ_n^2, such that

$$\sigma_n^2 = \overline{m}_R + \sigma_r^2, \tag{3.13}$$

where σ_r^2 is the variance of the read noise.

In the analysis that follows, we model the additive Gaussian noise [23], such that

$$\overline{m}_{H+N}^{(\delta)}\left(nx_p, my_p\right) = \overline{m}_{H}^{(\delta)}\left(nx_p, my_p\right) + \sigma_n n_k\left(nx_p, my_p\right), \tag{3.14}$$

where $\overline{m}_{H+N}^{(\delta)}$ is the mean number of hologram photo-electrons with noise and $n_k\left(nx_p, my_p\right)$ is the k^{th} realization of real-valued, zero-mean, unit-variance Gaussian random numbers. Correspondingly, the signal-beam estimate with noise $U_{S+N}^{(s)}$ takes the following form:

$$\widehat{U}_{S+N}^{(s)}\left(nx_p, my_p\right) = \widehat{U}_{S}^{(s)}\left(nx_p, my_p\right) + \sqrt{\zeta}\sigma_n N_k\left(nx_p, my_p\right), \tag{3.15}$$

where ζ is a constant resulting from the number of noise-contributing terms in Eqs. (3.3) - (3.5) (i.e., $\zeta = 4$ for the four- and two-step methods and $\zeta = 8$ for the three-step method), σ_n^2 is the noise variance [cf. Eq. (3.13)], and $N_k\left(nx_p, my_p\right)$ is the k^{th} realization of circular-complex Gaussian random numbers with zero mean and unit variance. In the signal-beam estimate, $\widehat{U}_S^{(s)}$ [cf. Eq. (3.12)], each measured hologram irradiance, $i_H^{(\delta)}$, adds to the total noise of the estimate and ζ accounts for this addition. Lastly, we state that $\zeta = 4$ for the two-step method; however, Eq. (3.5) has six terms. Since we assume $\overline{m}_R \gg \overline{m}_S$, the noise from the signal-beam irradiance ($|U_S|^2$) is negligible and even more so with the use of Eq. (3.6). This assumption is a sound one, as shown in the following analysis.

3.2.4 Signal-to-Noise and Field-Estimated Strehl Ratios

In what follows, we formulate the SNR $S/N^{(s)}$ as the ratio of the mean-signal power to the total-noise variance. As such, we obtain the following relationship:

$$S/N^{(s)} = \frac{\left\langle \left| \widehat{U}_S^{(s)}(x,y) \right|^2 \right\rangle}{\mathcal{V}\left\{ \widehat{U}_{S+N}^{(s)}(x,y) \right\}}, \tag{3.16}$$

where $\langle \cdot \rangle$ denotes mean over all pixels, $\widehat{U}_S^{(s)}$ is the signal-beam estimate [cf. Eq. (3.12)], $\mathcal{V}\{\cdot\}$ denotes the variance operator over all pixels, and $\widehat{U}_{S+N}^{(s)}$ is the is the signal-beam estimate with noise [cf. Eq. (3.15)]. Here, we again drop the FPA coordinates to denote the average over the entire detection area. Provided Eq. (3.16) along with Eqs. (3.10 - 3.12), we then determine the mean-signal power as

$$\left\langle \left| \widehat{U}_S^{(s)}(x,y) \right|^2 \right\rangle = \frac{\kappa^2}{s} \overline{m}_R \overline{m}_S, \tag{3.17}$$

and the total-noise variance as

$$\mathcal{V}\left\{ \widehat{U}_{S+N}^{(s)}(x,y) \right\} = \zeta \sigma_n^2. \tag{3.18}$$

Substituting Eqs. (3.17) and (3.18) into Eq. (3.16), we obtain the following closed-form expressions for the SNR:

$$S/N^{(4)} = \frac{\overline{m}_R \overline{m}_S}{\overline{m}_R + \sigma_r^2} \tag{3.19}$$

for the four-step method,

$$S/N^{(3)} = \frac{2}{3} \frac{\overline{m}_R \overline{m}_S}{\overline{m}_R + \sigma_r^2} \tag{3.20}$$

for the three-step method, and

$$S/N^{(2)} = \frac{1}{2}\frac{\overline{m}_R\overline{m}_S}{\overline{m}_R + \sigma_r^2} \tag{3.21}$$

for the two-step method. If $\overline{m}_R \gg \sigma_r^2$, then we reach the shot-noise limit and these closed-form expressions become a function of only $\overline{m}_S$. In turn, these closed-form expressions for the SNR provide a nice metric for the performance of digital holography in the on-axis PSRG.

Another performance metric of interest in the analysis is the field-estimated Strehl ratio $S_F^{(s)}$ [57, 20, 21]. As shown in Appendix B and C, we can relate $S_F^{(s)}$ to the SNR $S/N^{(s)}$ via the following relationship [57]:

$$S_F^{(s)} = \frac{1}{1 + \frac{1}{S/N^{(s)}}}. \tag{3.22}$$

Provided Eq. (3.22) along with Eqs. (3.19 - 3.21), we obtain the following closed-form expressions for field-estimated Strehl ratio:

$$S_F^{(4)} = \frac{\overline{m}_R\overline{m}_S}{\overline{m}_R\overline{m}_S + \overline{m}_R + \sigma_r^2} \tag{3.23}$$

for the four-step method,

$$S_F^{(3)} = \frac{2\overline{m}_R\overline{m}_S}{2\overline{m}_R\overline{m}_S + 3\left(\overline{m}_R + \sigma_r^2\right)}, \tag{3.24}$$

for the three-step method, and

$$S_F^{(2)} = \frac{\overline{m}_R\overline{m}_S}{\overline{m}_R\overline{m}_S + 2\left(\overline{m}_R + \sigma_r^2\right)}, \tag{3.25}$$

for the two-step method. We verify the use of these closed-form expressions in the next section.

3.3 Performance Metric Comparison using Wave-Optics Simulations

This section develops the wave-optics simulations employed to verify the closed-form expressions developed above for the signal-to-noise and field-estimated Strehl ratios. We conduct this analysis entirely in MATLAB using the principles from Schmidt [34] with help from WaveProp [58] and AOTools [59] which are MATLAB toolboxes written by the Optical Sciences Company. For further insight on these wave-optics simulations, we list several references that include additional detail [60, 20, 61, 21, 51].

3.3.1 Numerical Model

With Fig. 3.1 in mind, we modeled the point-source beacon as a narrow sinc function modulated by a raised-cosine envelope on a 4096 x 4096 numerical grid. Note that we set the physical side length of the numerical grid in the object plane, so that we met Fresnel scaling. We then propagated the point-source beacon to the pupil plane using the split-step beam propagation method. Here, we collimated the light and cropped the numerical grid to 256 256, so that it had the same physical side length as the pupil diameter, D. We provide a list of simulation parameters in Table 3.1.

Table 3.1. Simulation parameters used in the wave-optics simulations.

$\lambda = 1$ μm	optical wavelength
$D = 30$ cm	pupil diameter
$z = 7.5$ km	propagation distance
$h = 10$ m	horizontal-path altitude

With Table 3.1 in mind, we modeled five-distinct scenarios with increasing turbu-

lence strengths. Table 3.2 lists the refractive-index structure parameter, C_n^2, spherical-wave log amplitude variance (Rytov number), $\sigma_{\chi-sw}^2$, and spherical-wave coherence length (Fried parameter), r_{0-sw}, for the various scenarios. For a given C_n^2, wavelength λ, and horizontal-path propagation distance z, we can calculate $\sigma_{\chi-sw}^2$ and r_{0-sw}, respectively, using the following formulas [33]:

$$\sigma_{\chi-sw}^2 = 0.124 k^{7/6} z^{11/6} C_n^2 \tag{3.26}$$

and

$$r_{0-sw} = 0.33 \left(\frac{\lambda^2}{z C_n^2} \right)^{3/5}, \tag{3.27}$$

where $k = 2\pi/\lambda$ is the angular wavenumber. Provided Eqs. (3.26) and (3.27), the turbulence strength becomes proportional to the Rytov number and inversely proportional to the Fried parameter. Recall for imaging systems, the Fried parameter provides a measure for resolution relative to the pupil diameter D; therefore, the larger, the better. Additionally, the Rytov number provides a measure for the amount of scintillation. As a rule of thumb, Rytov numbers less than 0.2 provide weak scintillation and those greater than 0.2 provide strong scintillation. As shown in Table 2, the turbulence strength increases from Scenario 1 to Scenario 5.

With respect to the split-step beam propagation method, we used ten equally-spaced Kolmogorov phase screens to achieve deep-turbulence conditions. By satisfying Fresnel scaling, we met all of the sampling requirements set forth by Schmidt [34], as discussed in Thornton *et al.* [51]. For model verification, the discrete calculations

Table 3.2. Turbulence parameters used for five-distinct scenarios.

Scenario	1	2	3	4	5
$C_n^2 \ \left[m^{-2/3} \times 10^{-15}\right]$	1.00	1.50	2.00	2.50	3.00
$\sigma_{\chi-sw}^2$	0.135	0.202	0.270	0.337	0.404
$r_{0-sw} \ [cm]$	9.92	7.78	6.55	5.73	5.14

were within 1% error when compared to the continuous calculations [cf. Eq. (3.26) and (3.27)]. Additionally, we calculated the Monte-Carlo averages associated with the magnitude of the complex degree of coherence in the pupil plane using 40 independent realizations for Scenarios 1-5 in Table 3.2, and the results closely matched theory [51]. We show an example of one realization of the irradiance and wrapped phase in Fig. 3.4 for the simulated signal-beam truth.

In addition to the turbulence strength, we varied the FPA sampling by changing the number of FPA pixels across a demagnified pupil image. For this objective, we interpolated the simulated signal beam in the pupil plane to match the size of the FPA. Note that we fixed the square-pixel width, so that the physical size of the FPA was proportional to the number of pixels across. Therefore, we demagnified the simulated signal beam, such that $M_T = W/D$, where M_T is the transverse magnification, $W = N_p w_{x,y}$ is the side length of the FPA, N_p is the FPA sampling, and $w_{x,y}$ is the square-pixel width. After this demagnification via interpolation, we scaled the mean number of signal photoelectrons $\overline{m}_S$ to vary the signal strength. For this purpose, we set the characteristics of the FPA, such that the quantum efficiency was 100%, as well as the pixel-fill factor. Additionally, we assumed a uniform, linear-pixel gain from zero to saturation (100,000 pe). As mentioned before, we then set the read-noise standard deviation, such that $\sigma_r = 100$ pe, and the strength of the simulated strong-reference beam, so that $\overline{m}_R = 75,000$ pe. Put another way, we set the mean number of reference photoelectrons $\overline{m}_R$ to 75% of pixel-well depth of the FPA to create a strong-reference beam but avoid pixel saturation and excess shot noise.

We accounted for each phase-shifting strategy by dividing the simulated signal beam by the number of measurements needed for the corresponding method [cf. the factor s in Eq. (3.12)]. With this in mind, we then estimated the complex-optical field in the pupil plane with the corresponding pixel-by-pixel formulas [cf. Eq. (3.12)

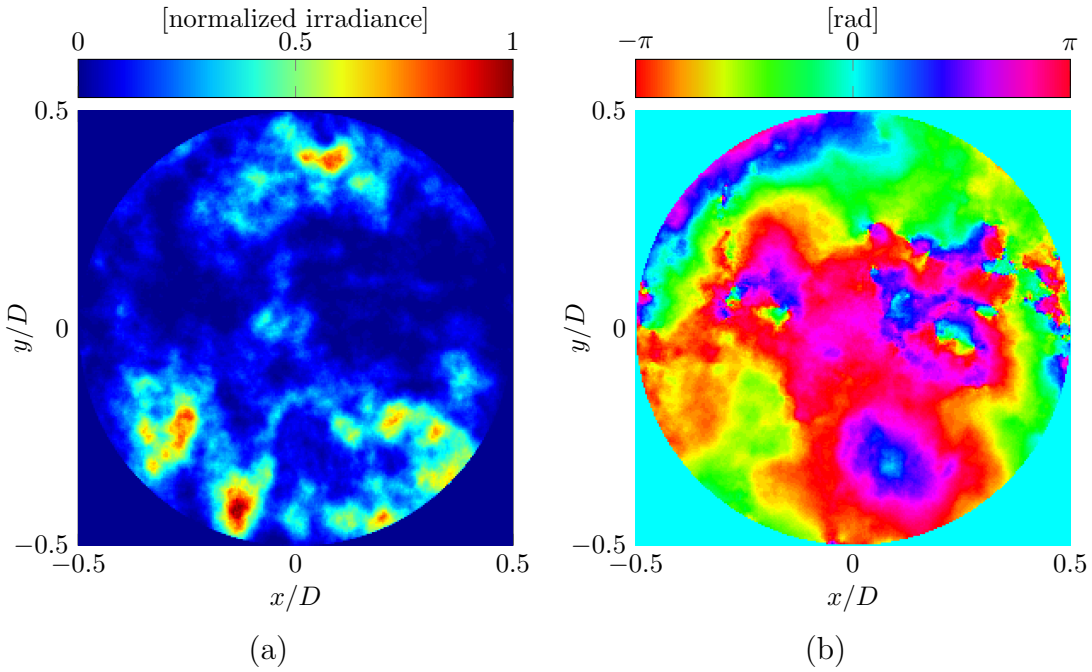

Figure 3.4. The (a) irradiance and (b) wrapped phase for the simulated signal-beam truth for one realization of the turbulence (cf. Scenario 5 in Table 3.2).

along with Eqs. (3.3) - (3.5)]. We show an example of one realization of the irradiance and wrapped phase in Fig. 3.5 for the simulated signal-beam estimate.

3.3.2 Numerical Results

The results of the wave-optics simulations presented here cover a three-fold trade space with respect to the four-, three-, and two-step methods. In particular, we quantify performance by

1. varying the signal strength,

2. varying the turbulence strength, and

3. varying the FPA sampling.

As shown in Fig. 3.6, we verify the use of Eqs. (3.19) - (3.25). Here, we compare both the numerical field-estimated Strehl ratio S_F and numerical SNR S/N to theory.

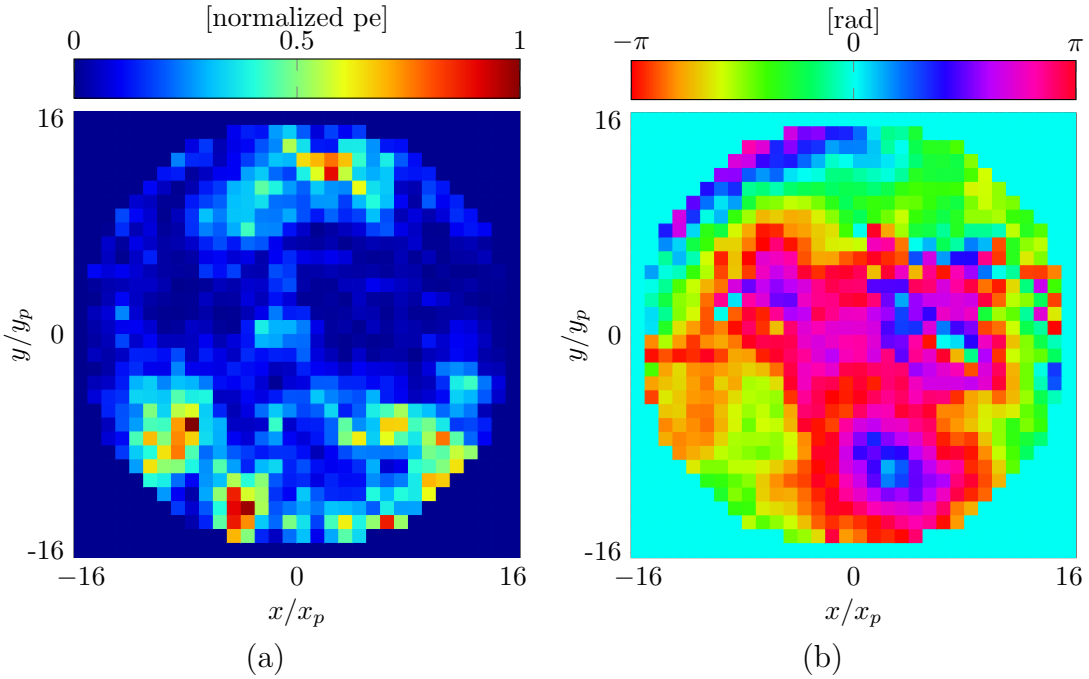

Figure 3.5. The (a) irradiance and (b) wrapped phase for the simulated signal-beam estimate for one realization of turbulence (cf. Scenario 5 in Table 3.2).

Note that the differences between the theoretical lines and data points are less than 1% for the Monte-Carlo averages from 40 independent realizations of turbulence and 30 independent realizations of noise for all of the scenarios given in Table 3.2. To calculate S_F, we made use of the following relationship (cf. Appendix B):

$$S_F = \frac{\left|\left\langle U_S(x,y)\widehat{U}^*_{S+N}(x,y)\right\rangle\right|^2}{\langle|U_S(x,y)|^2\rangle\left\langle|\widehat{U}_{S+N}(x,y)|^2\right\rangle}, \tag{3.28}$$

where $U_S(x,y)$ is the signal-beam truth and $\widehat{U}_{S+N}(x,y)$ is the signal-beam estimate with noise. Similarly, to calculate S/N, we made use of the following relationship:

$$S/N = \frac{\left\langle|\widehat{U}_{S+N}|^2 - |\widehat{U}_N|^2\right\rangle}{Var\{\widehat{U}_N\}} \tag{3.29}$$

where $\widehat{U}_N$ is the noise estimate associated with reconstructing only the strong-reference beam [cf. Eq. (3.12) along with Eqs. (3.3) - (3.5)].

With the results of Fig. 3.6 in mind, in Fig. 3.7 we compare the numerical field-estimated Strehl ratio S_F as a function of signal strength $\overline{m}_S$ to theory [cf. Eq. (3.25 - 3.23)]. Again, the observed error between theory and the numerical results is less than 1% for the Monte-Carlo averages from 40 independent realizations of turbulence and 30 independent realizations of noise for Scenario 1 and 5 in Table 3.2. From the results, we see that the four-step method is the most efficient phase-shifting strategy, despite having the most required signal-beam splits. The complete sampling of the phase in $\pi/2$ steps, in practice, results in a more-precise estimate of the complex-optical field. Put another way, the ζ term within the total-noise variance $\zeta\sigma_n$ [cf. Eq. (3.16)] introduces less noise into the estimate for the four-step method.

It is important to note that the the results contained in Figs. 3.6 and 3.7 made use of a FPA with 256 pixels across the simulated demagnified pupil image (i.e., $M_T = 1$). With that said, Fig. 3.8 shows the relative percent difference between the theoretical and numerical field-estimated Strehl ratios for Scenarios 1 and 5 from Table 3.2 and the four-step method. Here, M_T varied such that the modeled, square FPA size ranged from 16 - 256 pixels across (N_p), and as such, the signal-beam estimate's grid size varied from 16x16 to 256x256. To compare the signal-beam estimate to the simulated signal-beam truth (256 pixels across), we upsampled via linear interpolation. We plot the results as a function of the FPA sampling N_p (y axis) and the signal strength $\overline{m}_S$ (x axis). In Fig. 3.8, we calculate the relative percent difference as

$$\Delta S_F = \frac{S_F - S_F^{(4)}}{S_F^{(4)}} \times 100, \tag{3.30}$$

where $S_F^{(4)}$ is the theoretical result [cf. Eq. (3.23)]. Provided Eq. (3.30), positive values represent the case where $S_F > S_F^{(4)}$, whereas negative values represent the case

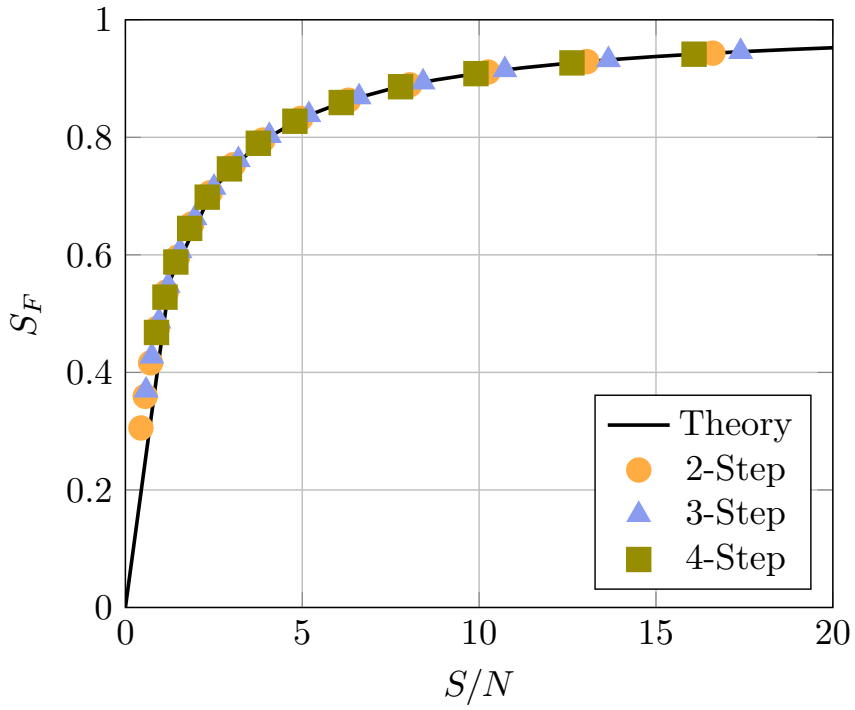

Figure 3.6. The numerical field-estimated Strehl ratio S_F versus the numerical SNR S/N with a comparison to theory. Shown here is the Monte-Carlo averages from 40 independent realizations of turbulence and 30 independent realizations of noise for all of the scenarios given in Table 3.2 and the three separate phase-shifting strategies of interest in this paper. Note that $N_p = 256$ for all of these results.

where $S_F < S_F^{(4)}$.

With Fig. 3.8 in mind, a couple features become apparent in the analysis. First, we reach steady-state differences between the theoretical and numerical results when $\overline{m}_S \gtrsim 10$, which is where the $S/N \gtrsim 10$ and $S_F \gtrsim 0.9$. As we increase the turbulence strength, the induced sampling errors also increase, and the results for Scenarios 2-4 also follow this trend. Thus, turbulence strength only affects the FPA sampling requirements. The largest differences occur with smaller values of N_p and stronger turbulence strengths. Secondly, at low SNR's ($S/N < 10$), the differences vary greatly with N_p. This outcome is due to the smoothing that occurs given the coarser FPA sampling [cf. the 2D convolution in Eq. (3.12)]. It also shows that when we properly sample the Fried parameter [cf. Eq. (3.27)], digital holography estimates

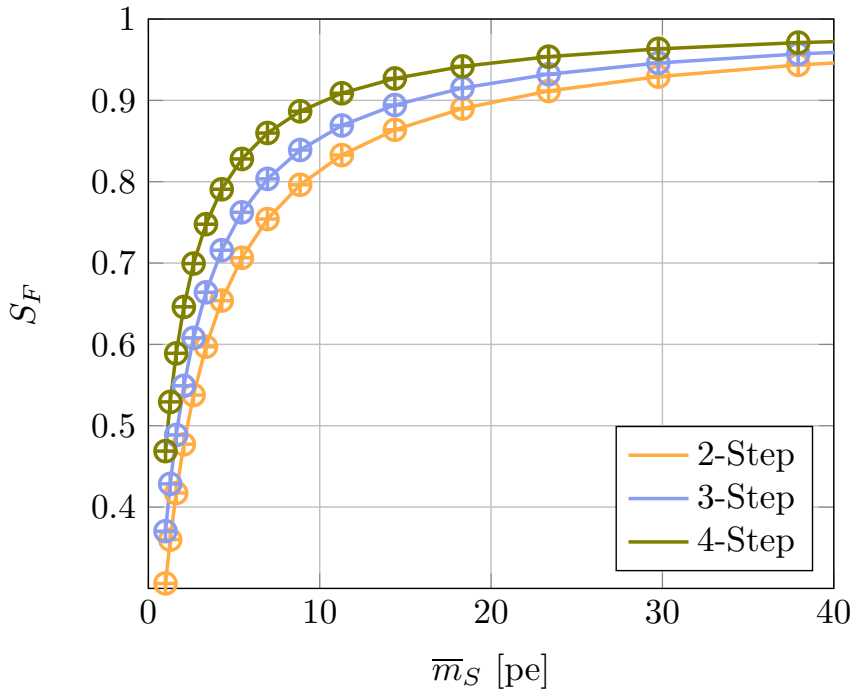

Figure 3.7. The numerical field-estimated Strehl ratio S_F versus the the signal strength $\overline{m}_S$ with a comparison to theory. Shown here is the Monte-Carlo averages from 40 independent realizations of turbulence and 30 independent realizations of noise for Scenario 1 and Scenario 5 in Table 3.2 and the three separate phase-shifting strategies of interest in this paper. Note that $N_p = 256$ for all of these results. Also note that the $\circ$'s represent the results from Scenario 1, whereas the $+$'s represent the results from Scenario 5.

the complex-optical field exceptionally well [62].

3.4 SRI Comparison

As discussed above, the SRI is an alternative interferometric wavefront-sensing method [47]. The primary difference between digital holography and the SRI is that the SRI splits the received signal beam to create a reference beam via spatial filtering, typically with a single-mode optical fiber. With that said, Rhoadarmer and Klein provide further discussion on the design of an SRI [55]. Various phase-shifting strategies also exist for the SRI, but similar to digital holography in the on-axis PSRG, the

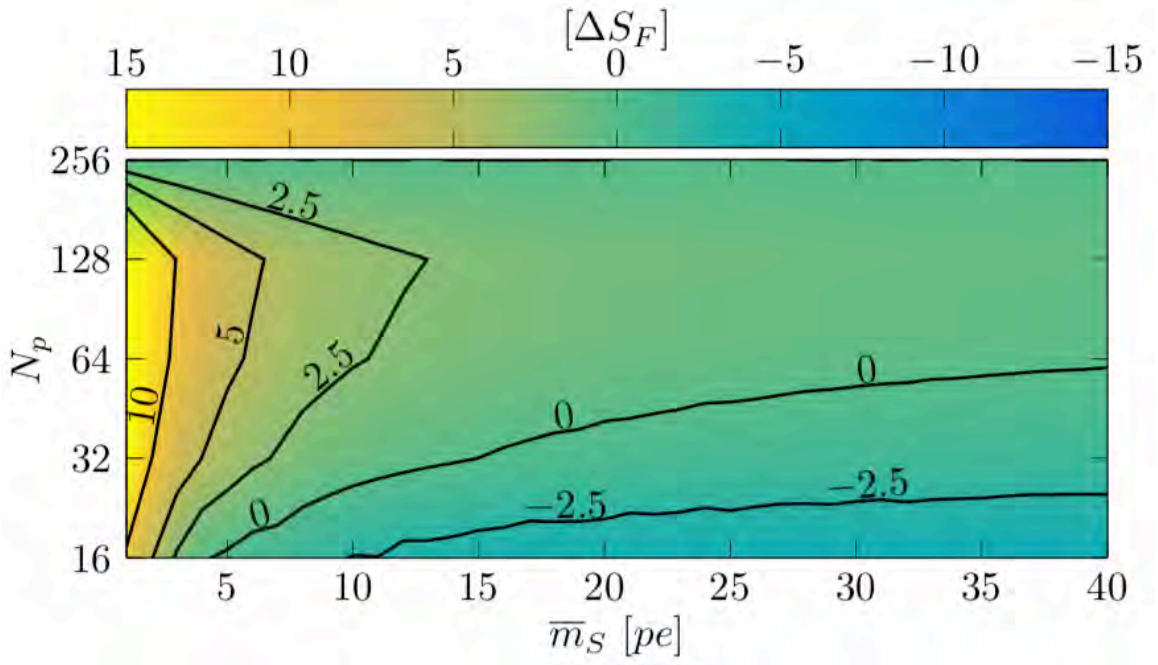

(a)

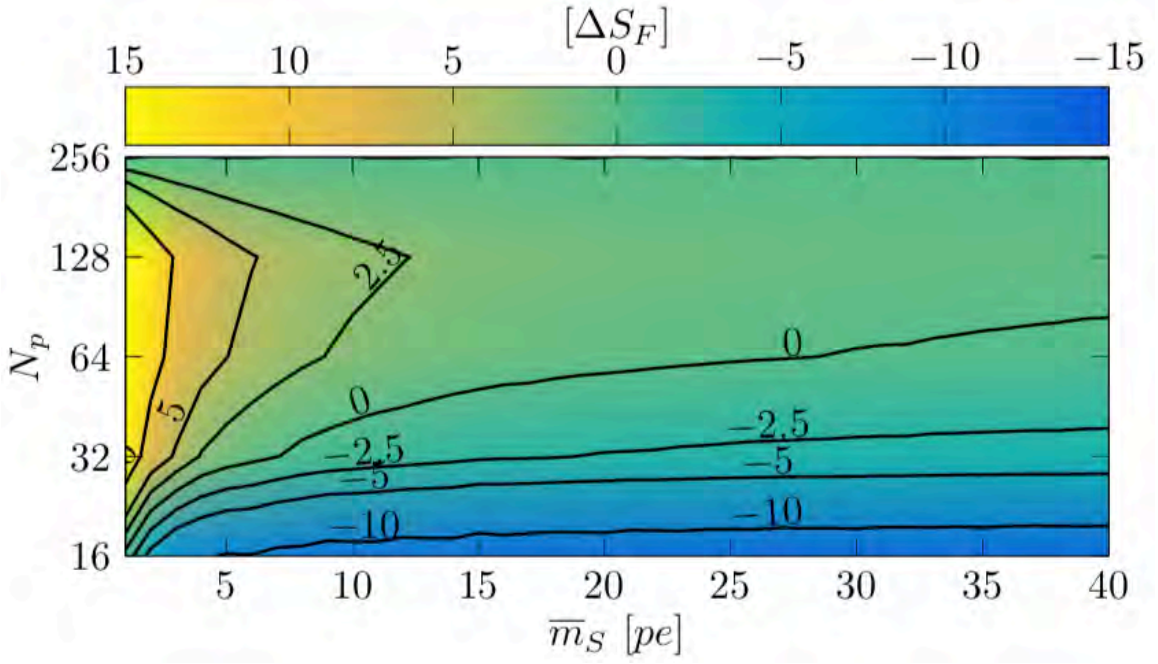

(b)

Figure 3.8. The relative percent difference (ΔS_F) between the theoretical and numerical field-estimated Strehl ratios for (a) Scenario 1 and (b) Scenario 5 from Table 3.2. We plot the results as a function of the FPA sampling N_p and mean signal strength $\overline{m}_S$ for the four-step method [cf. Eq. (3.23)]. Shown here is the Monte-Carlo averages from 40 independent realizations of turbulence and 30 independent realizations of noise.

four-step method has the best performance [63].

In this section, we model deep-turbulence wavefront sensing using the SRI in the same fashion as the four-step method for digital holography in the on-axis PSRG (i.e., in an open-loop configuration) with a few exceptions. The first exception is that we set the beam-splitter ratio β, which splits the signal beam to create the reference beam, so that $\overline{m}_S = \overline{m}_R$. This choice maximizes the SNR [64]. Additionally, we include the effects of a fiber-coupling efficiency η_c. Wheeler and Schmidt [50] showed that this efficiency depends on the spatial coherence radius ρ_0 or the coherence length r_0, since $r_0 \approx 2.1\rho_0$ [35], relative to the pupil diameter D. From Table 3.2, the corresponding η_c for Scenario 1 and Scenario 5 is 10% and 1%, respectively. Therefore, in the analysis that follows, we make use of the following three cases: $\eta_c = 100\%$ for the ideal case, $\eta_c = 10\%$ for Scenario 1, and $\eta_c = 1\%$ for Scenario 5.

Because of the losses encountered with the fiber-coupling efficiency η_c, we need to introduce a new term: $\overline{m}_i$, which is the mean number of incident photoelectrons. For digital holography in the on-axis PSRG, $\overline{m}_i = \overline{m}_S$, since we use 100% of the signal beam. On the other hand, for the SRI, $\overline{m}_S = \beta\overline{m}_i$, which is the percent of the incident light split for the signal beam, and $\overline{m}_R = (1-\beta)\eta_c\overline{m}_i$, which is the percent of the incident light both split and coupled into the single-mode optical fiber for the reference beam. In turn, $\overline{m}_L = (1-\beta)(1-\eta_c)\overline{m}_i$ is the percent of the incident light lost do to fiber coupling, so that $\overline{m}_i = \overline{m}_S + \overline{m}_R + \overline{m}_L$ for the SRI.

Similar to the analysis presented above (cf. Section 3.2), Rhodarmer and Barchers formulated closed-form expressions for the SRI [57]. With respect to the four-step method, the SNR $S/N^{(4)}_{SRI}$ and field-estimated Strehl ratio $S^{(4)}_{F,\,SRI}$ follow as

$$S/N^{(4)}_{SRI} = \frac{1}{4}\frac{\overline{m}_S^2}{\overline{m}_S/2 + \sigma_r^2}, \tag{3.31}$$

and

$$S_{F,\,SRI}^{(4)} = \frac{\overline{m}_S^2}{\overline{m}_S^2 + 2\overline{m}_S + 4\sigma_r^2}, \tag{3.32}$$

respectively. Provided Eqs. (3.31) and (3.32), we compare the performance of digital holography in the on-axis PSRG to the SRI.

For the comparison, we formulated results from two perspectives, as shown in Figs. 3.9 and 3.10. Here, we verified the use of the closed-form expressions for the SRI [cf. Eqs. (3.31) and (3.32)]. Note that the differences between the theoretical lines and data points are less than 1% for the Monte-Carlo averages from 40 independent realizations of turbulence and 30 independent realizations of noise. Also, we made use of a FPA with 256 pixels across the simulated demagnified pupil image. With that said, the results show that digital holography in the on-axis PSRG outperforms the SRI with respect to the numerical field-estimated Strehl ratio S_F (cf. Fig. 3.9) and the numerical SNR S/N (cf. Fig. 3.10) by multiple orders of magnitude. As shown in Fig. 3.10, for example, there are notable differences in the incident mean number of incident photoelectrons $\overline{m}_i$ required to reach an $S/N = 10$ with approximately 21 dB difference for the ideal case (green to yellow), 28 dB difference for Scenario 1 (green to orange), and 37 dB difference for Scenario 5 (green to red). These differences represent the necessary SRI signal amplification needed to achieve similar performance to digital holography in the on-axis PSRG due to the lack of a strong-reference beam from the LO provided by digital holography.

3.5 Conclusion

The results presented here showcase the strengths of digital holography in the on-axis PSRG for the purposes of deep-turbulence wavefront sensing. Throughout this paper, we develop closed-form expressions for the field-estimated Strehl and signal-

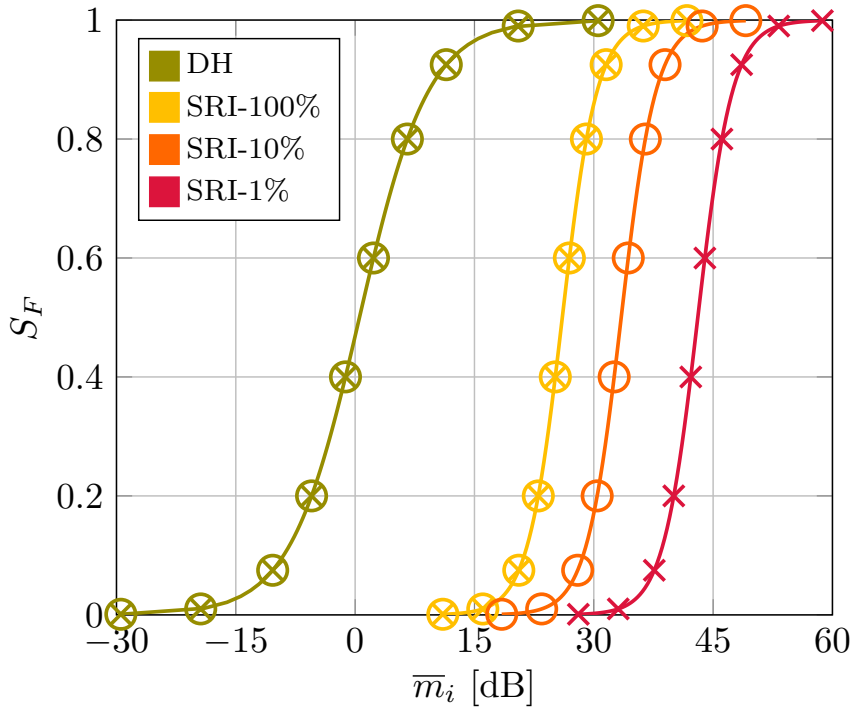

Figure 3.9. The numerical field-estimated Strehl ratio S_F versus the mean number of incident photoelectrons $\overline{m}_i$ for digital holography in the on-axis PSRG and the SRI with 100%, 10% and 1% fiber-coupling efficiency. Here, the solid lines represent the theoretical results for the four-step method [cf. Eq. (3.23) for digital holography in the on-axis PSRG and Eq. (3.32) for the SRI]. The ∘'s represent the numerical results for Scenario 1, whereas the x's represent the numerical results for Scenario 5 (cf. Table 3.2). Shown here is the Monte-Carlo averages from 40 independent realizations of turbulence and 30 independent realizations of noise.

to-noise ratios for the two-, three-, and four-step methods. Using detailed wave-optics simulations, which propagate a point-source beacon through deep-turbulence conditions, model digital holography with noise, and calculate the Monte-Carlo averages associated with increasing turbulence strengths and decreasing focal-plane array sampling, we also verify the use of these closed-form expressions. Overall, the results show the four-step method is the most efficient phase-shifting strategy and deep-turbulence conditions only degrade performance with respect to insufficient FPA sampling and low SNRs.

The first result is somewhat counterintuitive since the four-step method requires the most signal-beam splits. However, the results of the closed-form expressions and

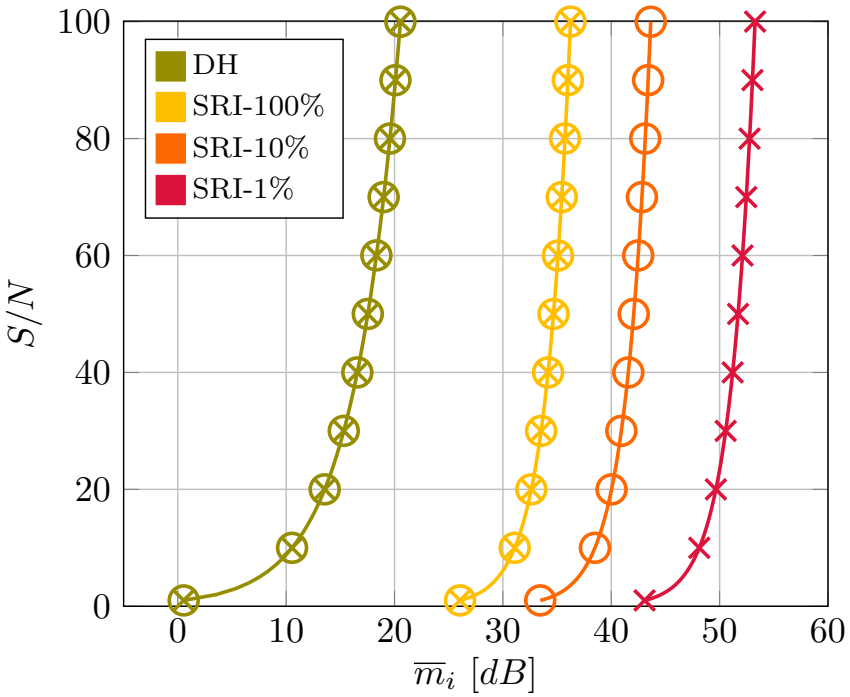

Figure 3.10. The numerical SNR S/N versus the mean number of incident photoelectrons $\overline{m}_i$ for digital holography in the on-axis PSRG and the SRI with 100%, 10% and 1% fiber-coupling efficiency. Here, the solid lines represent the theoretical results for the four-step method [cf. Eq. (3.19) for digital holography in the on-axis PSRG and Eq. (3.31) for the SRI). The ∘'s represent the numerical results for Scenario 1, whereas the x's represent the numerical results for Scenario 5 (cf. Table 3.2). Shown here is the Monte-Carlo averages from 40 independent realizations of turbulence and 30 independent realizations of noise.

detailed wave-optics simulations show the four-step method is more concise with less noise in estimating the complex-optical field. Furthermore, when the FPA sampling and SNR is sufficient, the percent difference between the theoretical results and the numerical results is negligible, regardless of the turbulence strength. In general, the results show when the FPA sampling is greater than 32 pixels and the SNR is greater than 10, the field-estimated Strehl ratios are greater than 0.9 (with respect to the four-step method).

A comparison to the SRI also shows the benefits of using a strong-reference beam to perform interferometric wavefront sensing. For this purpose, we modeled the SRI in an ideal way and included the effects of a fiber-coupling efficiency to provide more-

realistic SNRs with increasing turbulence strengths. In the low-SNR regime, the SRI needs 10's of dB more signal-beam power to achieve similar performance to digital holography in the on-axis PSRG. As such, this comparison provides a performance benchmark for applications involving deep-turbulence conditions.

In summary, this paper evaluates the performance of digital holography in the on-axis PSRG and enables the optimal design of such a deep-turbulence wavefront sensor. By employing four $\pi/2$ phase shifts, we minimized the total noise and improved system performance in terms of both the SNR and field-estimated Strehl ratio. System performance also approached theoretical limits when we sampled the four digital holograms with at least five pixels across the Fried parameter. Since digital holography provides a strong-reference beam from a LO, we then showed it outperforms the SRI in low signal-to-noise conditions for deep-turbulence applications. In turn, this paper provides the necessary analysis needed to design and conduct future deep-turbulence experiments using digital holography in the on-axis PSRG.

IV. Digital holography efficiency measurements with excess noise

The contents of this chapter was submitted to the *Digital Holography and 3-D Imaging* feature issue of *Applied Optics* on June, 24 2019 [65].

In this paper, we use digital holography (DH) in the off-axis image plane recording geometry with a 532 nm continuous-wave laser to measure the system efficiencies (multiplicative losses) associated with a closed-form expression for the signal-to-noise ratio (SNR). Measurements of the mixing efficiency (36.8%) and the reference-noise efficiency (74.5%) provide an expected total-system efficiency of $22.7\% \pm 6.5\%$ and a measured total-system efficiency of $21.1\% \pm 6.5\%$. These total-noise efficiencies do not include our measurements of the signal-noise efficiency (3%-100%), which are highly dependent on the signal strength and become significant for SNRs > 100. These results confirm that the mixing efficiency is generally the dominate multiplicative loss with respect to the DH system under test; however, excess reference and signal noise are significant multiplicative losses as well. Previous results also agree with these experimental findings.

4.1 Introduction

Digital holography (DH) has various remote-sensing applications including long-range imaging[10], 3D imaging [11], and wavefront sensing[66]. In particular, DH offers distinct benefits over traditional wavefront-sensing methods, such as a Shack-Hartmann wavefront sensor, given deep-turbulence conditions [20, 21, 39]. These conditions often arise from long, horizontal-propagation paths through the atmosphere and yield low signal-to-noise ratios (SNRs).

With low SNRs in mind, DH uses a strong reference to boost the weak signal above the noise and provide access to the complex-optical field. Since the SNR limits

the effective ranges of a fielded DH system, it is convenient to treat each source of loss as multiplicative factors in the derived SNR expression to estimate performance. Moving forward we need to quantify these multiplicative losses in order to characterize the performance of a fielded DH system.

In terms of performance, the dominate multiplicative loss or system efficiency is typically the mixing efficiency (i.e., the detected visibility of the signal and reference interference). For example, depolarization from rough-surface scattering reduces the SNR by 50% [67] and the pixel modulation transfer function (MTF) reduces the SNR by approximately 66%[68], yielding a mixing efficiency of 33%. Even with highly efficient focal plane arrays (FPAs) and highly transmissive optics, the ideal, total-system efficiency is generally below 30%. This last statement also assumes ideal laser coherence and noise, providing an upper bound on the total-system efficiency one can expect from a DH system.

While SNR measurements of coherent-lidar systems are available [69, 70, 71], there are distinct differences between these and the SNR measurements associated with DH systems. For example, DH uses spatial modulation, while coherent lidar uses temporal modulation. Since the demodulation techniques are different, some of the system efficiencies are different. To our knowledge, there has not been an examination of the system efficiencies associated with a DH system. Therefore, this paper presents a comparison between the expected and measured SNRs, a quantification of the major system efficiencies, and an examination of excess-noise sources all with respect to our DH system under test. In what follows, Section 4.2 provides the closed-form expressions needed for a comparison between expected and measured SNRs, Section 4.3 provides an overview of the experimental methods and data processing, Section 4.4 provides the results presented with discussion, and Section 4.5 provides a conclusion.

4.2 Closed-form expressions for SNR

In this section, we present the details associated with closed-form expressions for the SNR associated with DH in the off-axis image plane recording geometry (IPRG). Figure 4.1 shows an illustration of a DH system in the off-axis IPRG. Note that the detailed development of these closed-form expressions can be found in [23] and [72]. Also note that we experimentally measure the SNR in the next section to analyze the validity of our model and our assumptions.

4.2.1 Estimated signal and noise variance

Recall that we illustrate and explain DH in the off-axis IPRG in Fig. 4.1. At the FPA, the signal and reference interfere to produce the hologram irradiance, i_H, such that

$$i_H(x,y) = \left|U_S(x,y) + U_R(x,y)\right|^2, \tag{4.1}$$

where U_S and U_R are the complex-optical fields of the signal and reference, respectively. In units of Watts per square meter, i_H is spatially continuous and real valued. Throughout the remaining analysis, we assume that the reference uniformly illuminates the FPA, such that $|U_R(x,y)|^2 = |A_R|^2$, where A_R is the complex amplitude of the reference.

Provided Fig. 4.1, the FPA records the hologram on an $M \times N$ array of pixels as a per-pixel mean number of hologram photoelectons, $\overline{m}_H(x,y)$, in units of photoelectrons (pe). In turn, we model the noise as being additive with variance σ_n^2. We then digitize the hologram with a corresponding pixel gain, $g_{A/D}$, to produce the digital hologram with noise, $d_H^+(x,y)$, in units of digital numbers (DN). Then, we demodulate the hologram, as illustrated and explained in Fig. 4.2.

After the demodulation process, we ideally obtain our estimated signal, $\widehat{U}_S$. In

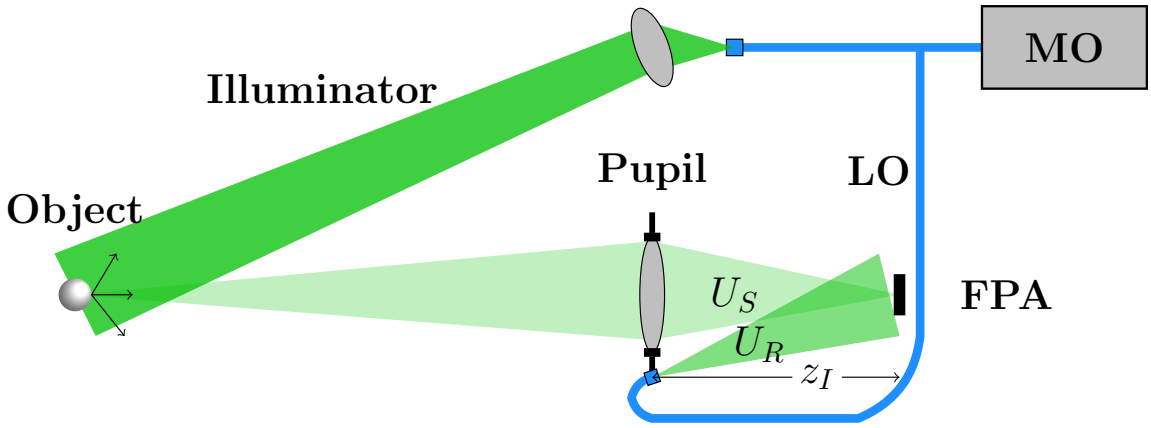

Figure 4.1. A DH system in the off-axis IPRG. Here, we split the light from the master oscillator (MO) laser into two paths: the illuminator and local oscillator (LO). Given the illuminator, we illuminate an object with an optically rough surface, and we collect the scattered speckle in a pupil given the appropriate receiver optics. Denoted as the signal complex-optical field, U_S, the pupil focuses the received speckle onto the FPA. In the other path, the LO provides the reference complex-optical field, U_R, and we inject the LO off axis in the pupil plane at (x_R, y_R) to illuminate the FPA.

particular,

$$\begin{aligned}\widehat{U}_S(x,y) =& g_{A/D}\frac{t_i p^2}{h\nu}U_R^* U_S(x,y) \\ &+ g_{A/D}\frac{\pi}{4q_I^2}\frac{\sigma_n(x,y)}{\sqrt{2}}\mathcal{N}_k(x,y),\end{aligned} \tag{4.2}$$

where t_i is the integration time, p is the square-pixel width, h is Planck's constant, ν is the MO laser frequency, q_I is the image-plane sampling quotient, σ_n^2 is again the total-noise variance, and $\mathcal{N}_k$ is the kth realization of circular-complex Gaussian random numbers with zero mean and unit variance for both the real and imaginary components (hence the $\sqrt{2}$ factor). In Eq. (4.2), q_I represents the number of circular-pupil diameters across the Fourier plane. Additionally, qI represents the number of pixels across the halfwidth of the Airy disk, such that

$$q_I = \frac{\lambda z_I}{p d_p}, \tag{4.3}$$

where λ is the MO laser wavelength, z_I is the image distance, and d_p is the pupil diameter. Therefore, the factor of $\pi/4q_I^2$ accounts for the portion of the noise win-

dowed from the Fourier plane. To account for σ_n^2, we include the shot noise from the reference and signal, in addition to the read noise with variance, σ_r^2, viz.

$$\sigma_n^2(x,y) = \overline{m}_R + \overline{m}_S(x,y) + \sigma_r^2, \tag{4.4}$$

where $\overline{m}_R$ is the mean number of reference photoelectrons and $\overline{m}_S(x,y)$ is the per-pixel mean number of signal photoelectrons. Note that the shot noise from the reference is not spatially varying, since we have assumed a uniform reference. We neglect quantization noise, since it is typically much less than σ_r^2 for high-bit-depth FPAs. Other noise sources exist [28, 26], but we assume they are also negligible.

4.2.2 Signal-to-noise ratio

In the analysis that follows, we make use of the power definition for the signal-to-noise ratio, S/N, such that

$$S/N\,(x,y) = \eta_T \frac{\mathcal{E}\left\{\left|\widehat{U}_S\,(x,y)\right|^2\right\}}{\mathcal{V}\left\{\widehat{U}_S\,(x,y)\right\}}, \tag{4.5}$$

where η_T is the total-system efficiency, $\mathcal{E}\{\cdot\}$ is the expectation operator, and $\mathcal{V}\{\cdot\}$ is the variance operator. Provided Eq. (4.2), the numerator follows as

$$\mathcal{E}\left\{\left|\widehat{U}_S\,(x,y)\right|^2\right\} = g_{A/D}^2\;\overline{m}_S\,(x,y)\,\overline{m}_R, \tag{4.6}$$

and the denominator follows as

$$\mathcal{V}\left\{\widehat{U}_S\,(x,y)\right\} = g_{A/D}^2 \frac{\pi}{4q_I^2}\sigma_n^2\,(x,y)\,. \tag{4.7}$$

Substituting Eq. (4.4) into Eq. (4.7), S/N becomes

$$S/N\left(x,y\right)=\eta_T\frac{4q_I^2}{\pi}\frac{\overline{m}_S\left(x,y\right)\overline{m}_R}{\overline{m}_R+\overline{m}_S\left(x,y\right)+\sigma_r^2}. \tag{4.8}$$

When we assume a strong reference, $\overline{m}_R \gg \overline{m}_S(x,y)$ and $\overline{m}_R \gg \sigma_r^2$, and we reach the shot-noise limit, such that

$$S/N\left(x,y\right)\approx\eta_T\frac{4q_I^2}{\pi}\overline{m}_S\left(x,y\right). \tag{4.9}$$

Similarly, we can derive the ideal, radiometric SNR, S/N_R. Using [72], we obtain the following closed form expression:

$$S/N_R\left(x,y\right)=\frac{\rho}{\pi}\frac{\lambda^2 t_i}{h\nu}\frac{P_o\left(M_T x_o, M_T y_o\right)}{A_o}, \tag{4.10}$$

where ρ is the surface reflection coefficient, the factor of π accounts for the Lambertian scattering, the factor of λ^2 accounts for the speckle [67], P_o is the power incident on the object, A_o is the area of the uniform object, and the coordinates $(M_T x_o, M_T y_o)$ are the magnified object-plane coordinates to convert to image-plane coordinates. Note that we can derive Eq. (4.10) from Eq. (4.9) with the proper radiometry and geometric- or ray-optics substitutions to satisfy imaging. Also note that we will use Eq. (4.10) in the analysis that follows as the expected SNR without multiplicative losses. The ratio of S/N_R with our measured SNR, S/N', will then enable us to calculate η_T.

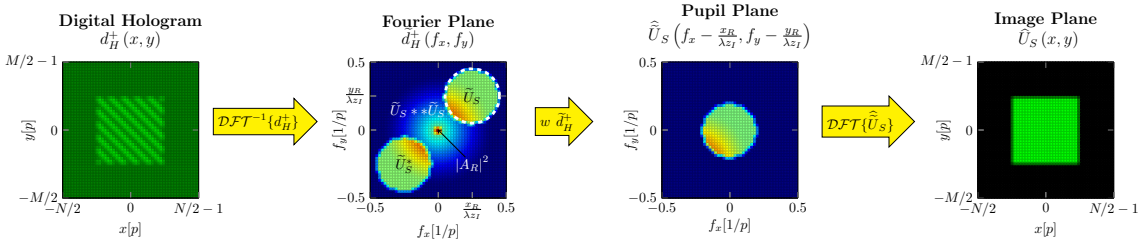

Figure 4.2. An illustration of the demodulation process for a digital hologram. The reference spatially modulates the signal (see the far-left fringes on top of the square image) and the FPA records the digital hologram with noise (i.e., d_H^+). Next, we perform an inverse discrete Fourier transform, $\mathcal{DFT}^{-1}$, on d_H^+, which produces $\widetilde{d}_H^+$ in the Fourier plane (magnitude shown). Four terms arise in the Fourier plane: a strong DC term from the reference irradiance (i.e., $|A_R|^2$); the autocorrelation of the pupil, $\widetilde{U}_S**\widetilde{U}_S$ (centered at DC), which produces a 2D chat profile [73]; the signal complex-optical field, $\widetilde{U}_S$ (shifted off-axis), since the image and pupil planes are Fourier-transform pairs; and the conjugate of the signal complex-optical field, $\widetilde{U}_S^*$ (shifted off axis in the opposite direction), since the Fourier transform has Hermitian symmetry. We then shift and window the Fourier plane to obtain the estimated signal, $\widehat{\widetilde{U}}_S$, in the pupil plane. Lastly, we preform a discrete Fourier transform, $\mathcal{DFT}$, to obtain the estimated signal, $\widehat{U}_S$, in the image plane (magnitude shown).

4.2.3 System Efficiencies

To account for the expected total-system efficiency, η_T, we comprise η_T in terms of several independent system efficiencies, viz.

$$\eta_T(x,y) = \eta_t\eta_q\eta_m\eta_R\eta_S(x,y). \tag{4.11}$$

Here, η_t is the transmission efficiency (atmospheric and optical), η_q is the quantum efficiency of the FPA, η_m is the mixing efficiency, η_R is the reference-noise efficiency, and $\eta_S(x,y)$ is the signal-noise efficiency. The mixing efficiency represents how well the detected reference and signal interfere to produce the spatial modulation known as fringes. It is compromised of two other efficiencies: the polarization efficiency, η_p, and spatial-integration efficiency, η_s. In what follows, we assume that there is the ideal temporal coherence between the signal and reference, otherwise, non-ideal coherence would factor into η_m.

Recall that the signal becomes fully depolarized via rough-surface scattering from our optically rough object, which we assume is comprised of a dielectric material. Therefore, only half of the signal interferes with the polarized reference [67], so that $\eta_p = 50\%$. The spatial-integration efficiency accounts for the detection of the spatial modulation with finite pixels. Using [24], we can mathematically realize the pixel-spatial integration of the hologram irradiance as a 2D convolution of the hologram irradiance with the spatial extent of the pixel. In the Fourier plane, this convolution turns into a multiplication with the pixel MTF. Given a square pixel, we estimate the pixel MTF with a 2D sinc function, where $\mathrm{sinc}(x) = 1$ when $x = 0$ and $\mathrm{sinc}(x) = \sin(\pi x)/(\pi x)$ when $x \neq 0$. We, in turn, approximate η_s as

$$\eta_s = \left\langle w\left(f_x, f_y\right) \mathrm{sinc}^2\left(p\, f_x, p\, f_y\right) \right\rangle, \tag{4.12}$$

where $w\left(f_x, f_y\right)$ is the window function for the pupil in the Fourier-plane coordinates (f_x, f_y) and $\langle \cdot \rangle$ denotes spatial average. Note that the pixel MTF is squared because of our SNR definition [cf. the sinc-squared term in Eq. (4.12)]. Also note that the value of η_s is dependent on the pupil-window size and pupil location in the Fourier plane. For example, our experiment had a $q_I = 2.70$ and the pupil centered at $(f_x, f_y) = (x_r/\lambda z_I, y_r/\lambda z_I) = (0.25, 0.26)$, which yields an $\eta_s = 64.4\%$.

In Eq. (4.9), we assume the use of a uniform, strong reference with Poisson-distributed shot noise. However in practice, the reference is not spatially uniform and single-mode lasers typically have some excess amplitude noise [74, 75]. Thus, we include the reference-noise efficiency, η_R, which is the ratio of reference shot noise (i.e., $\overline{m}_R$) to the demodulated-reference noise.

We also quantify the strong-reference approximation in Eq. (4.9) by introducing the signal-noise efficiency, $\eta_S\left(x, y\right)$. At high SNRs, the strong-reference approximation becomes less valid with a stronger signal. Not only does the signal shot noise

increase, but the amplitude of the pupil autocorrelation in the Fourier plane increases, which is sampled by the window function (cf. Fig. 4.2), and provides excess signal shot noise. Therefore, as the signal and SNR increases, the strong-reference approximation weakens. We quantify the excess signal noise with the signal-noise efficiency, η_S, which is the ratio of the demodulated-reference noise to the sum of the demodulated-reference and demodulated-signal noises.

Before moving on to the next section, we first report the initial-expected values for the various system efficiencies in Table 4.1. Assuming ideal coherence between the signal and reference, $\eta_m = 32.2\%$, since $\eta_p = 50\%$ and $\eta_s = 64.4\%$. In addition, we assume no excess noise from the reference, signal, or other noise sources, which allows us to simplify the SNR expression [cf. Eq. (4.8)] to be dependent only on the signal [cf. Eq. (4.9)]. The same goes for the radiometric SNR [cf. Eq. (4.10)].

Table 4.1. Expected system efficiencies

Name	Value	Source
transmission, η_t	99.7%	Vendor
quantum, η_q	83%	Vendor
mixing, η_m	32.2%	Eq. (4.12) & $\eta_p = 50\%$
reference noise, η_R	100%	Ideal [cf. Eq. (4.4)]
signal noise, η_S	100%	Ideal [cf. Eq. (4.9)]
total, η_T	27.5%	Calculated

4.3 Experimental methods and data processing

This section describes the experimental methods and procedures used in this paper. In order to compare the recorded data to our model, we performed the appropriate data processing in order to quantify the system efficiencies or multiplicative losses associated with our closed-form expressions for SNR. Recall that we formulated these expressions and multiplicative losses in the previous section [cf. Eqs. (4.9) - (4.11)].

4.3.1 Experimental setup

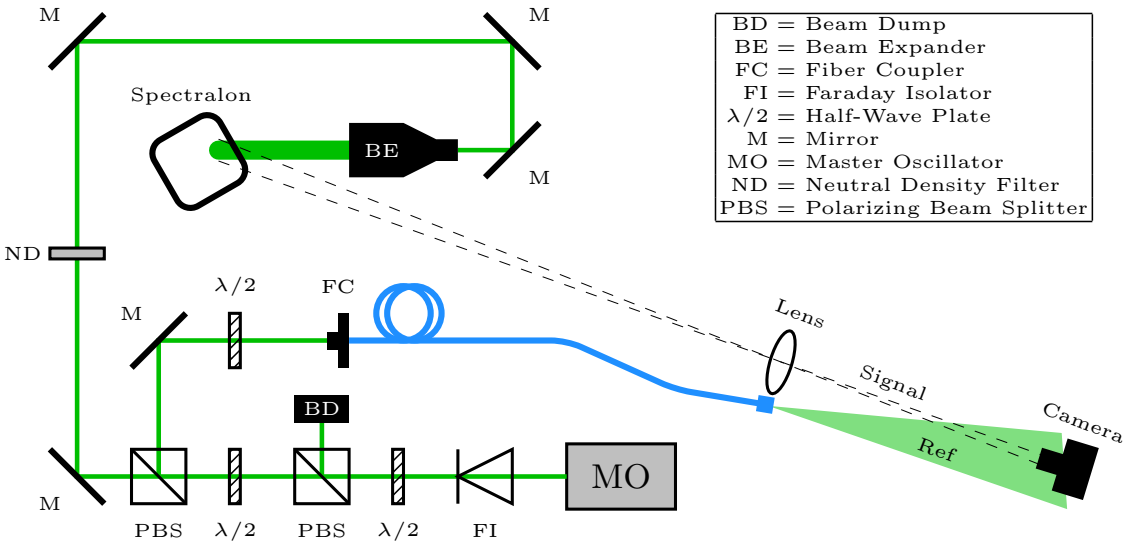

Figure 4.3. The experimental setup for our DH system under test.

As depicted in Fig. 4.3, we implemented a DH system in the off-axis IPRG. The MO laser was a Cobalt Samba 1000 continuous-wave diode pumped solid state laser with a wavelength of 532.1 nm, a linewidth of < 1 MHz, and an output power of 1 W. The MO laser output beam was nearly Gaussian ($M^2 < 1.1$) and collimated (full-angle divergence < 1.2 mrad) with a diameter of 700 μm at the laser-exit aperture. A Faraday isolator (FI) prevented back reflections from getting back into the MO laser, and a half-wave plate (HWP) and polarizing beam splitter (PBS) split a portion of the MO laser to a beam dump (BD), allowing us to adjust the MO laser's power. Another HWP and PBS split the MO laser into two paths for the LO and illuminator. To create the LO, we rotated the incident linear polarization state with a HWP to match the stress-rod orientation of the polarization-maintaining fiber before coupling with the appropriate optics. We adjusted the illuminator-path strength with a neutral density (ND) filter and directed it through a 20x beam expander to illuminate a sheet of Labsphere Spectralon with an approximate 4 cm spot diameter. The rough-surface scattering that resulted was approximately Lambertian with 99%

reflectivity. As such, to create new speckle realizations, we placed the sheet of Labsphere Spectralon on a tilted rotation stage.

A 1-inch lens with a focal length of 350 mm imaged the scattered-signal light (with an object distance of 2.46 m) to a monochrome Point Grey Grasshopper3 camera. The lens had a 532 nm anti-reflective coating and a transmission of 99.7%. We injected our LO near the lens and angled it such that we centered the resulting fiber-reference light near the center of the FPA. This geometry gave a measured $q_I = 2.70$ with the lens nearly centered in the top right quadrant of the Fourier plane at $(f_x, f_y) = (x_R/\lambda z_I, y_R/\lambda z_I) = (.25, .26)$, since $(x_R,\, y_R) = (1.56\,\text{cm},\, 1.62\,\text{cm})$.

To mitigate vibrational effects, we placed the entire experimental setup on a floating optical table. In turn, we verified the MO laser linewidth was < 1 MHz with a Fabry-Perot (FP) interferometer with a free spectral range of 1.5 GHz, a finesse of > 1500, and a spectral resolution of also < 1 MHz. Next, we measured the full width at half max to be about 1.2 MHz of an approximate Lorentzian profile. Since the observed lineshape is the convolution of the FP and laser lineshapes, this measurement agreed with the manufacture's specified linewidth and coherence length. The path difference between the signal and reference was 0.1 m, and we therefore assumed negligible coherence losses. In addition, the variation in laser power was $< 1\%$ with a power-meter measurement. We also conducted the same measurement for the fiber-reference light and we observed similar results. Furthermore, we verified the polarization of the signal and reference. We measured the fiber-output polarization with a polarizer and two power meters over an hour and it was $> 99\%$ polarized. Measuring the scattered-signal light reflected from the Spectralon in the same way, and we found that it was $> 99\%$ unpolarized.

The Grasshopper3 camera (GS3-U3-32S4M-C) was a 2048 x 1536 CMOS array with a specified 100% fill-factor and 3.45 μm square pixels. The camera had two cover

glasses, where the transmission losses were incorporated into the η_q specification (cf. Table 4.1). We used the camera in mode 7, which has a $\eta_q = 76\%$, but we removed the front cover glass to reduce the reference etaloning effects. The cover glass had a transmission of 91.7%, which gave an effective quantum efficiency of $\eta_q = 83\%$ for the camera. We recorded frames of data using Matlab. Along with the floating optical table, we set the camera integration time to 1 msec, which stabilized our SNR measurements. The camera-pixel gain was 1/0.17, which converts the received photoelectrons to 16-bit digital numbers on the camera [76]. We used camera mode seven, which converts the 16-bit digital numbers to 12-bit digital numbers and Matlab reads the pixel values as 16-bit digital numbers. Therefore, the first four bits of the recorded 16-bit digital numbers are padded. This outcome translates to a quantization-noise variance of $\sigma_q^2 = 21.3\,DN^2$. Note that the read-noise variance for mode 7 was about $5.5\,pe^2$ or $189.5\,DN^2$, and the pixel well depth was $10,482\,pe$. The reference strength was set to approximately $2,500\,pe$ or about a quarter of the pixel-well depth.

To perform speckle averaging, we rotated the Labsphere Spectralon stage between the recording of the hologram and signal frames to obtain different speckle realizations. We recorded twenty speckle realizations and twenty shot-noise averaging frames for each speckle realization, totaling 400 hologram and signal frames for each dataset. Additionally, we recorded 100 reference and 100 background frames for each dataset. In total, we collected six datasets with different signal strengths while approximately maintaining the fiber-reference-light and background-light levels.

4.3.2 Data processing

We show example recorded and demodulated frames in Fig. 4.4. Here, we demodulate each recorded frame according to Fig. 4.2 in MATLAB. We also demodulated the background frames. In turn, we calculated the frame-averaged background frame

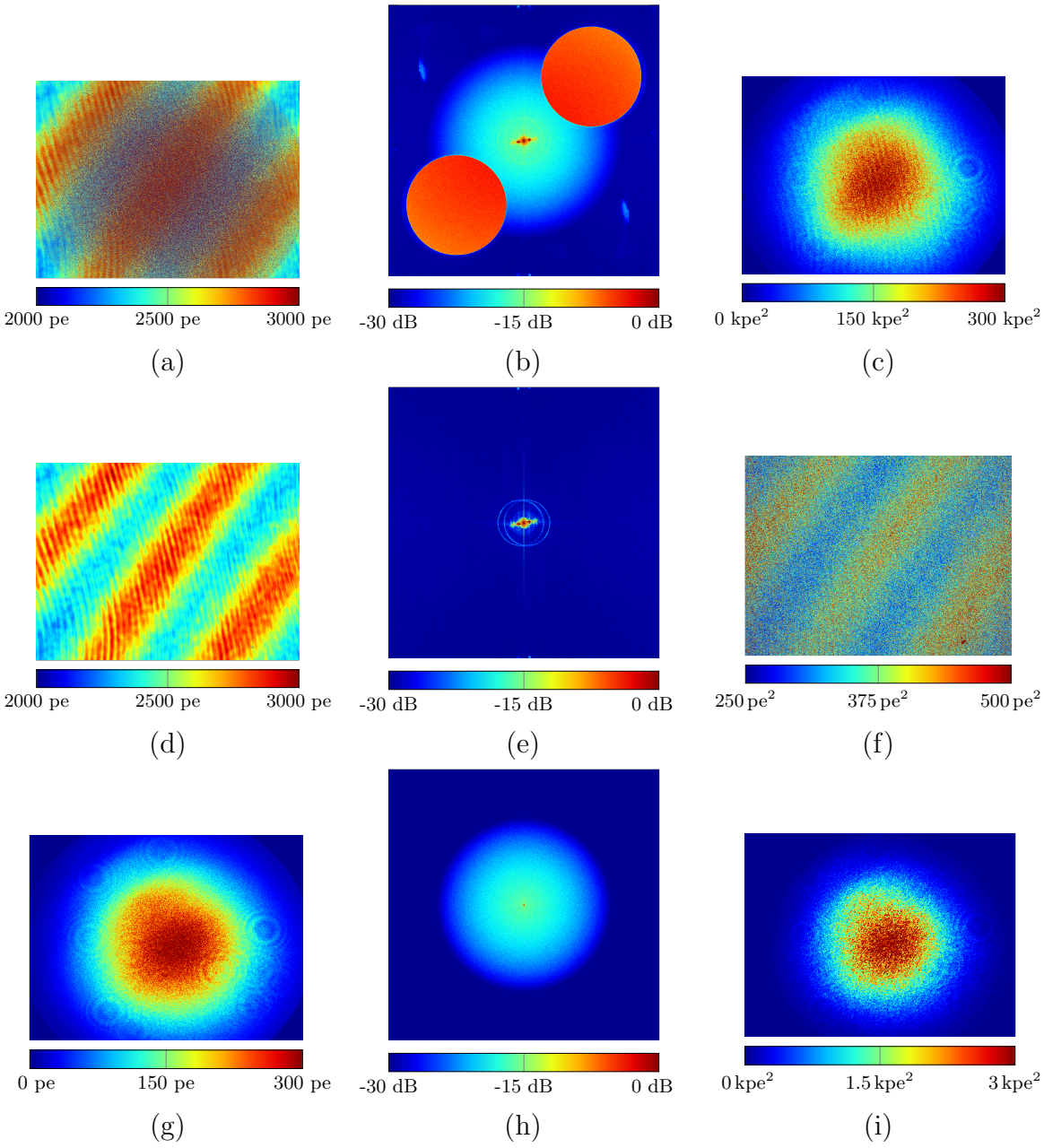

Figure 4.4. Each plot is from dataset 5, where $\overline{m}_S = 96\,pe$, and represents the full frame. Here, (a) shows a single hologram frame, (b) shows the mean hologram energy in the Fourier plane, (c) shows the mean hologram energy in the image plane $\overline{E}_H(x,y)$, (d) shows the mean number reference photoelectrons $\overline{m}_R(x,y)$, (e) shows the mean reference energy in the Fourier plane, (f) shows the mean reference-noise energy in the image plane $\overline{E}_R(x,y)$, (g) shows the mean number signal photoelectrons $\overline{m}_S(x,y)$, (h) shows the mean signal energy in the Fourier plane, and (i) shows the mean signal-noise energy in the image plane $\overline{E}_S(x,y)$. Note that the first and third columns have square pixels with a rectangular array, which gives rise to rectangular pixels with a square array in the second column.

(i.e., $\overline{m}_B(x,y)$) and subtracted it from the reference and signal frames prior to demodulation to eliminate background noise. We did not modify the hologram frames with background subtraction, so the spatial modulation was not altered. Then, we converted each frame from DN to pe using the manufacturers specification for gain: $g_{A/D} = 1/0.17$. Since the gain cancels out in Eq. (4.9) and is in terms of pe, this conversion provided a better comparison between the recorded frames and demodulated energies. We did not perform any non-uniformity correction since the pixel-to-pixel performance variation was likely averaged out with the 3.2 mega-pixel array. Table 4.2 shows the pixel- and frame-averaged values for the background, signal, reference, and hologram number of photoelectrons (i.e., $\overline{m}_B$, $\overline{m}_S$, $\overline{m}_R$, and $\overline{m}_H$, respectively).

We defined the pupil window in the Fourier plane by using the definition of the image-plane sampling quotient q_I [cf. Eq. (4.3)]. In addition, we used the same pupil window to demodulate the reference, signal, and background frames. We then averaged the frames associated with the squared magnitude of the demodulated hologram, reference, signal, and background frames, which yielded the mean hologram energy, $\overline{E}_H(x,y)$, mean reference-noise energy, $\overline{E}_R(x,y)$, and mean signal-noise energy, $\overline{E}_S(x,y)$. As such, the mean total-noise energy, $\overline{E}_N(x,y)$, was the sum of the our mean noise energies, such that $\overline{E}_N(x,y) = \overline{E}_R(x,y) + \overline{E}_S(x,y)$, and Table 4.2 provides pixel-averaged values for these noise energies. Note that we excluded the background noise energy from $\overline{E}_N(x,y)$ because it was insignificant.

4.3.3 Signal fit

Figure 4.5 shows the radial profile of the per-pixel mean number of signal photoelectrons, $\overline{m}_S(x,y)$, for the six datasets provided in Table 4.2. For comparisons to the radiometric SNR [cf. Eq. (4.10)], we needed a profile for the signal to estimate the power at the object, P_o. For this purpose, we considered the signal's speckle noise.

Table 4.2. Pixel- and frame-averaged values with respect to the six datasets.

dataset	1	2	3	4	5	6
$\overline{m}_B$ $[pe]$	0.17	0.16	0.16	0.17	0.16	0.18
$\overline{m}_S$ $[pe]$	4.0	10.3	15.5	54.2	96.3	230
$\overline{m}_R$ $[pe]$	2,509	2,576	2,572	2,548	2,560	2,536
$\overline{m}_H$ $[pe]$	2,511	2,583	2,584	2,601	2,661	2,764
$\overline{E}_S$ $[pe^2]$	0.6	5.9	13.4	157	527	2,523
$\overline{E}_R$ $[pe^2]$	375	369	360	365	375	358
$\overline{E}_N$ $[pe^2]$	375	375	374	522	901	2,881
$\overline{E}_H$ $[pe^2]$	2,494	9,460	14,598	51,873	88,159	209,920

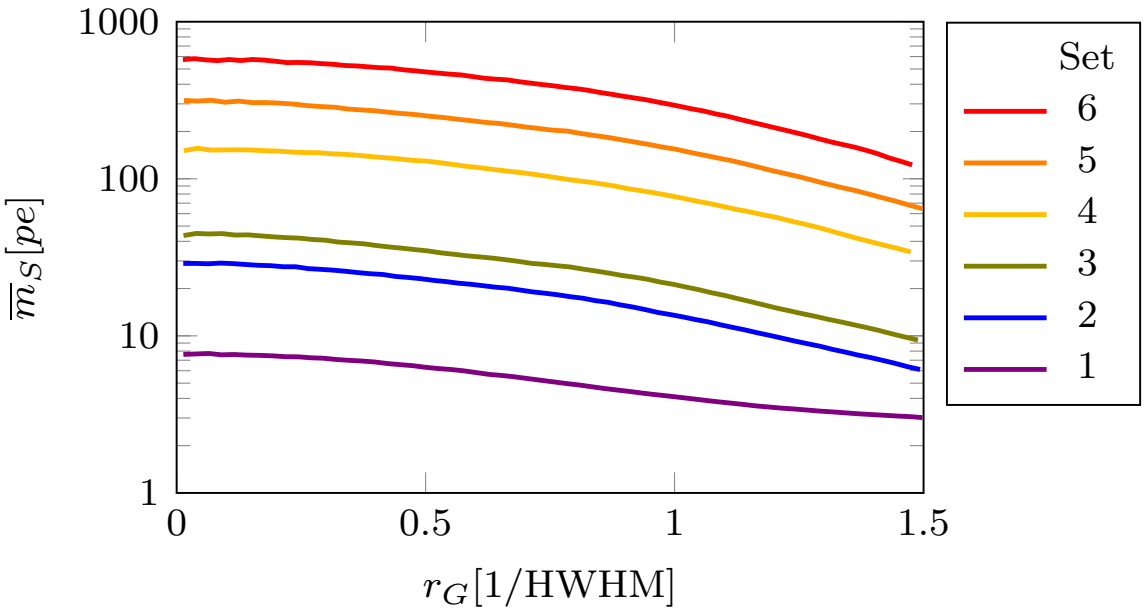

Figure 4.5. The azimuthal average of $\overline{m}_S$ for the six datasets.

The speckle area was approximately $9.7\,p^2$ with a measured squared speckle contrast, C^2 (i.e., the ratio of the pixel variance to the squared mean), of approximately 0.45, which was within 1% to Goodman's theory [77][1] . Speckle averaging reduced the measured C^2 by approximately 80% to 0.024. Along with the smoothness of Fig. 4.5, we concluded that speckle averaging was sufficient enough to fit a profile to $\overline{m}_S(x, y)$.

With the above details in mind, we fit a 2D-Gaussian profile, $G(x, y)$, to $\overline{m}_S(x, y)$,

[1]Goodman uses the rms (or amplitude definition) of SNR and the speckle contrast is the inverse of the SNR (i.e., the standard deviation to the mean). Since we used the power definition of SNR, C^2 enables a better comparison to our measurements.

such that

$$G(x,y) = A\exp\left(-\frac{1}{2}\left[\left(\frac{x-x_c}{\sigma_x}\right)^2 + \left(\frac{y-y_c}{\sigma_y}\right)^2\right]\right), \tag{4.13}$$

where the fitting parameters were: A, the Gaussian amplitude; x_c and y_c, the Gaussian center location; and σ_x and σ_y, the Gaussian widths in the x and y directions. We provide some fit parameters of interest in Table 4.3, along with the r-squared (r^2) fitting metric. The reported uncertainty of each fit parameter was within a few percent. We believe the stark difference of dataset 1's ($\overline{m}_S = 4.0\,pe$) fit parameters was due to the wings of the beam being below the noise floor of the detector. In addition, we believe the variations between datasets 2-5 was due to realignment with the illuminator and beam expander between dataset collections. Figure 4.6 shows the relative percent error in the fit for dataset 5, where $\overline{m}_S = 96\,pe$. Here, we observed some structure from an imperfect Gaussian beam, which we believe is due to minor misalignment of the beam expander, the input beam diameter over filling the input aperture of the beam expander, but not significant laser multi-modal behavior.

In what follows, we show multiple figures with azimuthally averaged measurements (cf. Fig. 4.5). We performed the azimuthal averages with respect to the normalized Gaussian radius, r_G. Because of the slightly different x and y widths from the tilted Labsphere Spectralon stage. We then normalized the radius to the x and y half width at half max (HWHM), viz.

$$r_G(x,y) = \sqrt{\left(\frac{x-x_c}{\sqrt{2\ln(2)}\sigma_x}\right)^2 + \left(\frac{y-y_c}{\sqrt{2\ln(2)}\sigma_y}\right)^2}, \tag{4.14}$$

where the factor of $\sqrt{2\ln(2)}$ converts $\sigma_{x,y}$ to the HWHM. Therefore, $r_G = 1$ corresponds to the Gaussian profile at half the maximum value, which provides a spatial comparison.

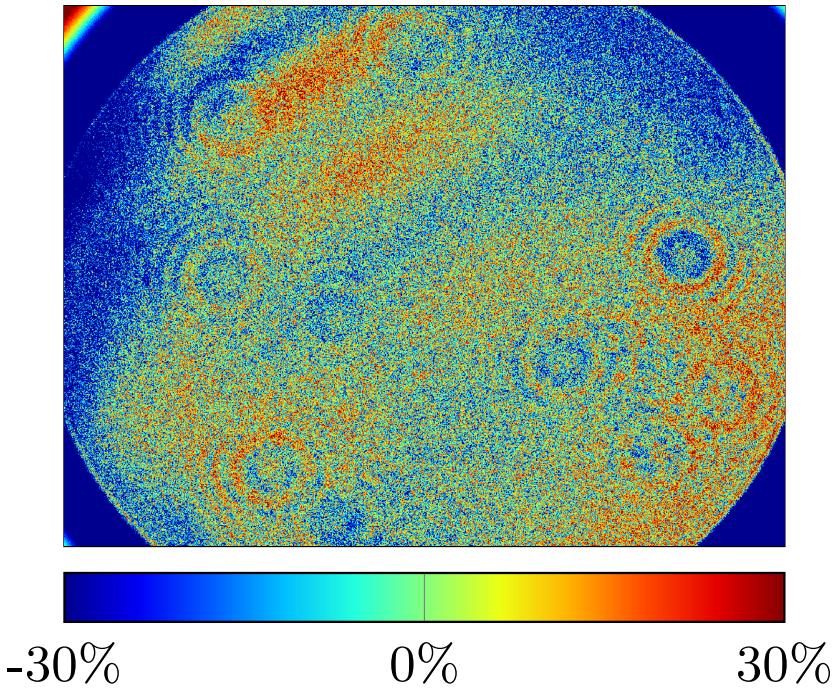

Figure 4.6. The relative percent error of the fit for dataset 5, where $\overline{m}_S = 96pe$.

Table 4.3. Gaussian fit results with respect to the six datasets.

dataset	1	2	3	4	5	6
A $[pe]$	7.6	27.5	42.1	153	304	577
σ_x $[p]$	484	457	465	454	427	497
σ_y $[p]$	509	445	441	441	405	477
$r - squared$	0.53	0.90	0.90	0.90	0.92	0.88

4.3.4 Radiometric SNR

To calculate the radiometric SNR, S/N_R, for the measured total-system efficiency, we measured the power of the illuminator beam at the tilted Labsphere Spectralon stage over a minute and took a picture of the power meter location with the FPA. The power meter was a ThorLabs PM100D with S130C photodiode. It was 6 months into the calibration lifespan of 2 years and had a vendor specified uncertainty of $\pm 3\%$. In MATLAB, we drew a mask over the detector area of the power-meter picture. We then scaled $G(x, y)$ based on the average power measurement and the mask to obtain the spatial power distribution $P_o(x, y)$ in Eq. (4.10). Fig. 4.7 shows the azimuthally

averaged S/N_R for each of the six datasets. When compared to Fig. 4.5, the SNR's reported in Fig. 4.7 are almost an order of magnitude greater than the signal. This outcome is because of the $4q_I^2/\pi$ factor in Eq. (4.9), which was about 9.3.

4.4 Measurements, results, and discussion

In this section, we present three measured efficiencies: the mixing efficiency η'_m, which again is the product of the polarization efficiency, η_p, and spatial-integration efficiency, η_s; the reference-noise efficiency, η'_R; and the signal-noise efficiency η'_S. These measured efficiencies refined our expected total system efficiency η_T for comparison to our measured total system efficiency η'_T. Additionally, we present results from a previous experiment [68], where we corrected the camera integration time to 55 μsec. Appendix D contains additional details with respect to this previous experiment.

4.4.1 Measured mixing efficiency η'_m

To determine η'_m, we calculated the ratio of the hologram energy without noise to the product of the mean number of signal and reference photoelectrons, such that

$$\eta'_m(x,y) = \frac{\overline{E}_H(x,y) - \overline{E}_N(x,y)}{\overline{m}_R(x,y)\overline{m}_S(x,y)}. \tag{4.15}$$

As a reminder, η'_m represents how well the detected reference and signal interfere and is the product of the polarization efficiency ($\eta_p = 50\%$) and spatial-integration efficiency ($\eta_s = 64.4\%$). Additionally, η'_m would capture any losses not quantified earlier due to vibration or coherence effects, which we assume to be negligible in the present analysis. Figure 6.3(a) shows $\eta'_m(x,y)$ for dataset 5, where $\overline{m}_S = 96\,pe$, and Figure 6.3(b) shows the radial profile of η'_m for the six datasets.

In Fig. 4.8(a), we observed the measurement was noisy but uniform over the area

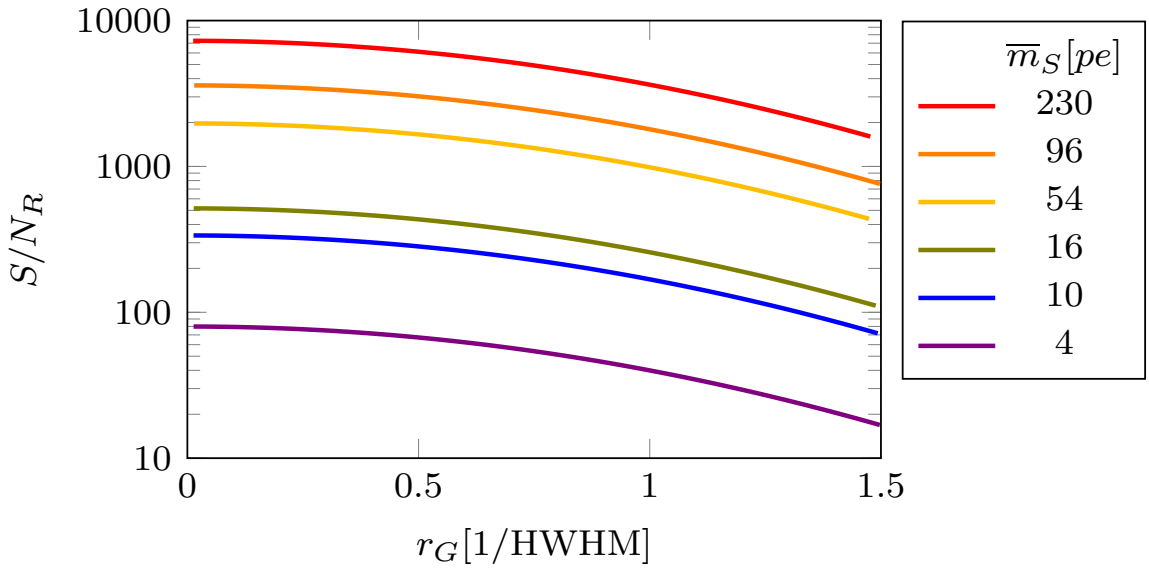

Figure 4.7. The azmuthial average of S/N_R for the six datasets.

of illumination. Furthermore, Fig. 4.8(b) shows the azimuthal average for the six datasets, where we saw η'_m was relatively constant for each dataset except for dataset 1. For dataset 1, $\overline{m}_S = 4\,pe$ and we determined that the FPA's absolute sensitivity threshold, where the camera SNR = 1, was $4\,pe$, so we recorded those signal frames at the detection limit of the FPA. More importantly, datasets 2-6 were 4.6% greater than the expected η_m of 32.2% from Section 4.2.3. Recall that we modeled the pixel as an ideal square with an ideal-sinc MTF. Since our FPA used microlenses to achieve a specified 100% pixel-fill factor, the ideal-sinc model MTF was different than expected. This increase in η'_m as compared to theory is fortunate, but shows that the pixel MTF can vary η_s by 10%.

We show a summary of the pixel averaged η'_m in Table 4.4. Here, we took the pixel average over the area of illumination in the frame. We excluded dataset 1 from the average because of the weak signal as mentioned before. In addition, we believe the large standard deviations are from the different speckle realizations between the recorded signal and hologram frames. The average η'_m for datasets 5 and 6 (the two

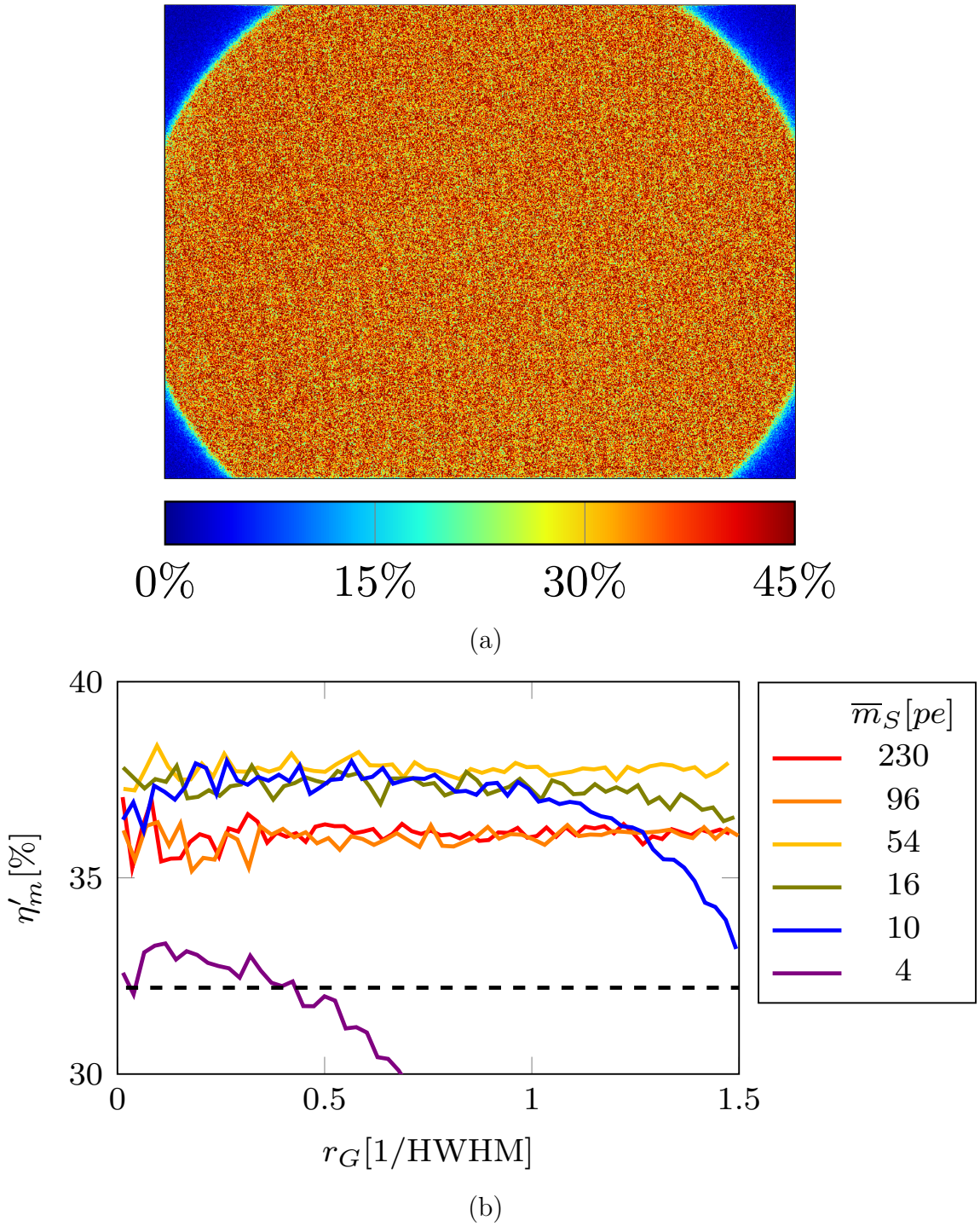

Figure 4.8. **(a) The mixing efficiency η'_m for dataset 5, where $\overline{m}_S = 96\,pe$. (b) The azimuthial average of η'_m for each dataset with the expected value of 32.2% in the black, dashed line.**

highest signal strengths) were about a percent less than datasets 2-4, which can also be seen in Fig. 6.3(b). We suspected this outcome was due to pixel nonlinearity in the signal frames. Thus, we used the results from datasets 2-6 to obtain an average mixing efficiency of $\eta'_m = 36.8\% \pm 10.2\%$ to incorporate into our estimated total-system efficiency for comparison to our measured total-system efficiency.

4.4.2 Measured reference-noise efficiency η'_R

We determined the reference-noise efficiency, η'_R, as

$$\eta'_R = \frac{\pi}{4q_I}\frac{\overline{m}_R}{\overline{E}_R}, \tag{4.16}$$

where the factor of $\pi/4q_i$ again accounts for the ratio of the window area to the total Fourier plane area, and the $\overline{m}_R$ and $\overline{E}_R$ quantities are both pixel- and frame-averaged values (cf. Table 4.2). Recall that η'_R represents excess reference noise, which means the reference noise is greater than the shot noise. Table 4.4 contains the results from each dataset.

The average η'_R of 74.5% corresponded to the measured reference noise being $\approx$34% greater than the shot noise (i.e., $1/\eta'_R$). To further investigate the source of this excess reference noise, we measured the per-pixel ratio of reference-light variance $\sigma^2_R(x,y)$ to $\overline{m}_R(x,y)$ and referred to as the shot-noise ratio. The average of this ratio across all the pixels was 1.11, which demonstrates that the reference noise was 11% greater than the shot noise. We also verified this outcome in the free-space beam to rule out the LO fiber as the source. However, we found that the shot-noise ratio increased > 2 times for shorter integration times $< 1\,msec$, where a temporal dependence is indicative of laser-amplitude noise. For comparison to the other experiment (cf. Appendix D), which used a different MO laser, $\eta'_R = 50\%$, and the average shot-noise ratio was 1.36, where the integration time was $55\,\mu sec$. However, the difference

between our shot-noise ratio and η_R led us to believe some of the excess reference noise arises from the demodulation process.

We initially assumed the nonuniformity in the reference was filtered in the Fourier plane by the pupil window because it contained low spatial frequencies outside of the window. However, the etalon pattern was still prominent in $\overline{E}_R(x, y)$ [cf. Fig. 4.4(f)], and therefore we did not filter out all of the reference nonuniformity with our Fourier-plane window. We also observed this etalon effect in the other experiment (cf. Fig. D.1 in Appendix D). Therefore, we suspected the non-uniform reference compounded the excess reference noise captured by η'_R.

These results showed that the shot-noise limit assumption for the reference [cf. Eq. (4.4)] can be insufficient. In the worst case, this efficiency loss can be as significant as the polarization loss $\sim 50\%$. This efficiency can be improved upon with better laser control electronics to reduce the laser-amplitude noise, choice of FPA integration time, anti-reflective coatings on the FPA cover glass, and other such measures to reduce the reference-etalon effect.

Table 4.4. Mixing and reference-noise efficiency measurements

		Pix. avg. ± st. dev.	
dataset	$\overline{m}_S[pe]$	η'_m	η'_R
1	4	31.2% ± 8.7%	71.8% ± 2.1%
2	10	36.8% ± 10.2%	74.9% ± 1.9%
3	16	37.3% ± 10.3%	76.5% ± 1.9%
4	54	37.8% ± 10.6%	74.8% ± 2.1%
5	96	36.1% ± 9.9%	73.3% ± 1.8%
6	230	36.1% ± 10.0%	76.0% ± 2.0%
	Avg.	36.8% ± 10.2%	74.5% ± 2.0%

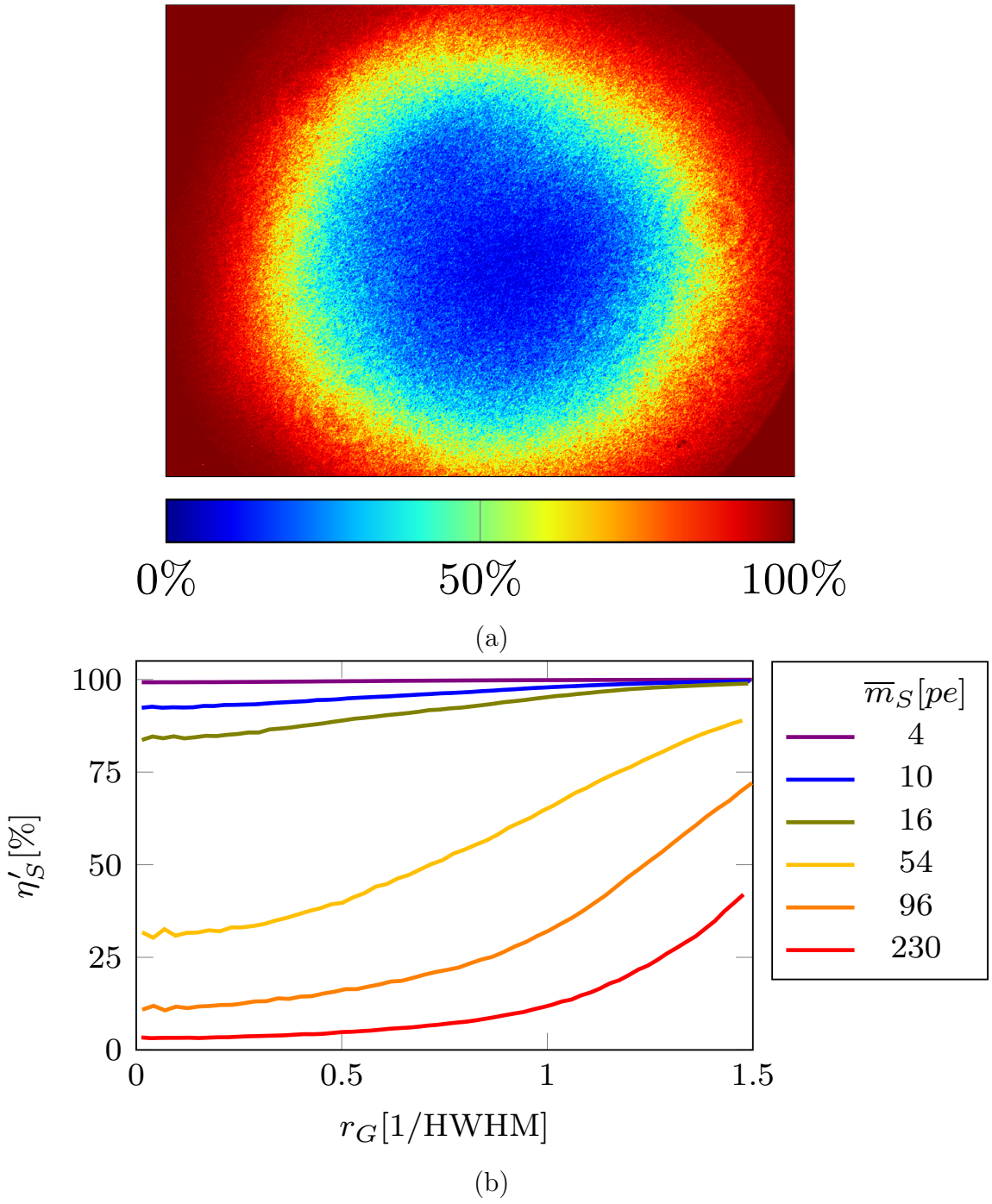

Figure 4.9. (a) A calculated frame of the signal-noise efficiency η'_S for dataset 5 where $\overline{m}_S = 96\,pe$. (b) The azimuthal average of η'_S for each dataset.

4.4.3 Measured signal-noise efficiency η'_S

For the signal-noise efficiency η'_S, we calculated the ratio of the reference noise energy to the total noise energy, such that

$$\eta'_S(x,y) = \frac{\overline{E}_R(x,y)}{\overline{E}_N(x,y)}. \tag{4.17}$$

As a reminder, η'_S represents the excess signal noise present in the signal-dependent SNR expression [cf. Eq. (4.9)]. Note that if we had significant background noise, detector noise, or other noise sources, then we could include the background noise energy in $\overline{E}_N(x,y)$ to capture other noise sources. We show the η'_S measurement for dataset 5, where $\overline{m}_S = 96\,pe$, in Fig. 4.9(a) and a radial comparison of the six datasets in Fig. 4.9(b).

In Fig. 4.9, we observed that η'_S is inversely proportional with the Gaussian-signal profile. When $\overline{m}_R \gg \overline{m}_S$, the signal shot noise was negligible as in dataset 1, where $\overline{m}_S = 4\,pe$ and $\eta'_S \approx 100\%$. In the other datasets, we observed η'_S was a minor efficiency loss for datasets 2 and 3 ($\overline{m}_S = 10\,pe$ and $16\,pe$, respectively) and became a major efficiency loss at the higher signal strengths (e.g., datasets 4-6, where $\overline{m}_S > 54\,pe$).

The majority of the excess noise came from the signal with the partially windowed pupil autocorrelation in the Fourier plane. As the strength of the signal shot noise increased, so did the strength of the pupil autocorrelation, which increased faster than the signal shot noise. We show this outcome in Fig. 4.10, where we preformed a power regression. On the log-log plot, we fit a line ($y = mx + b$) to the $\log_{10}$ of the data (i.e., $\overline{E}_S$ vs $\overline{m}_S$), where the average residual was $< 10\%$. The slope was $m = 2.04$ with a y-intercept of $b = -1.36$. This result corresponded to a quadratic line $y = 0.044x^2$ for the data, which demonstrated that $\overline{E}_S$ increased faster than the signal shot noise. As

such, this quadratic relationship is sound because the pupil autocorrelation energy is proportional to $\overline{m}_S^2$ and the signal shot noise energy is proportional to $\overline{m}_S$. The strong-reference assumption used in the closed-form SNR expression in Section 4.2, where the total noise is dominated by the reference noise, becomes less valid when $\overline{m}_R \lesssim 100\,\overline{m}_S$.

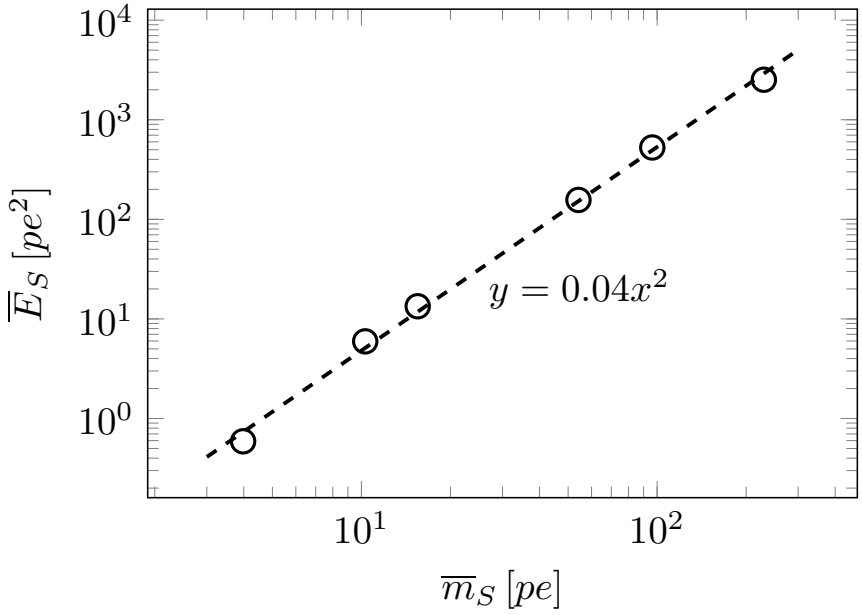

Figure 4.10. A power regression (dashed line) of $\overline{m}_S$ vs $\overline{E}_S$ showing the signal noise energy $\overline{E}_S$ was proportional to the square of the per-pixel mean number of signal photoelectrons $\overline{m}_S$ and not linear like shot noise.

4.4.4 Measured signal-to-noise ratio, S/N'

We determined S/N' as the ratio of the hologram energy without noise to the total noise energy, viz.

$$S/N'(x,y) = \frac{\overline{E}_H(x,y) - \overline{E}_N(x,y)}{\overline{E}_N(x,y)}, \tag{4.18}$$

where S/N' is equivalent to S/N [cf. Eq. (4.9)] when all of our assumptions are valid. We show $S/N'(x,y)$ for dataset 5, where $\overline{m}_S = 96\,pe$, in Fig. 4.11(a) and a radial

comparison for the six datasets in Fig. 4.11(b).

We observed the curves in Fig. 4.11(b) were approximately Gaussian at the lower signal strengths (datasets 1-3), but deviated from the Gaussian shape for the higher signal strengths (datasets 4-6). As seen previously with η'_S, $\overline{E}_S$ became a considerable noise source between datasets 3 and 4 ($\overline{m}_S = 16\,pe$ and $54\,pe$, respectively). This outcome occurred when $S/N' \gtrsim 100$, and the SNR drop was due to the excess signal shot noise, as previously discussed in Sec. 4.4.3. This outcome illustrates that the excess signal shot noise imposes an upper limit to the SNR, which was ≈ 140 from the peak of dataset 4 in Fig. 4.11(b). Additionally, η_S could appear to be an overwhelming efficiency loss, but it only becomes significant for high signal strengths where the SNR is substantial. For example, in dataset 6, $\overline{m}_S \approx 577$ (peak from the fit) and $\eta'_S \approx 3\%$, but the center of $S/N' \approx 50$. While the SNR upper limit and η_S could appear to be detrimental, we only need a SNR > 10 for applications like deep-turbulence wavefront sensing [20, 21, 39].

4.4.5 Measured total system efficiency η_T

To determine η'_T, we calculated the ratio of the SNRs, such that

$$\eta'_T(x,y) = \frac{1}{\eta'_S(x,y)} \frac{S/N'(x,y)}{S/N_R(x,y)}. \tag{4.19}$$

We included $\eta'_S(x,y)$ in Eq. (4.19) to counter the spatial- and signal- strength dependence in the noise as seen in the measured SNR (cf. Sec 4.4.4). With this last point in mind, we show $\eta'_T(x,y)$ for dataset 5, where $\overline{m}_S = 96\,pe$, in Fig. 4.12(a). The frame is mostly noisy in the center, but some similar structure exists towards the wings of the Gaussian profile that we observed in the fit residuals (cf. Fig. 4.6). We also did not observe any structure related to the non-Gaussian shape that we saw in Fig. 4.11(a) with respect to the measured SNR. Recall that the $\eta_S(x,y)$ factor

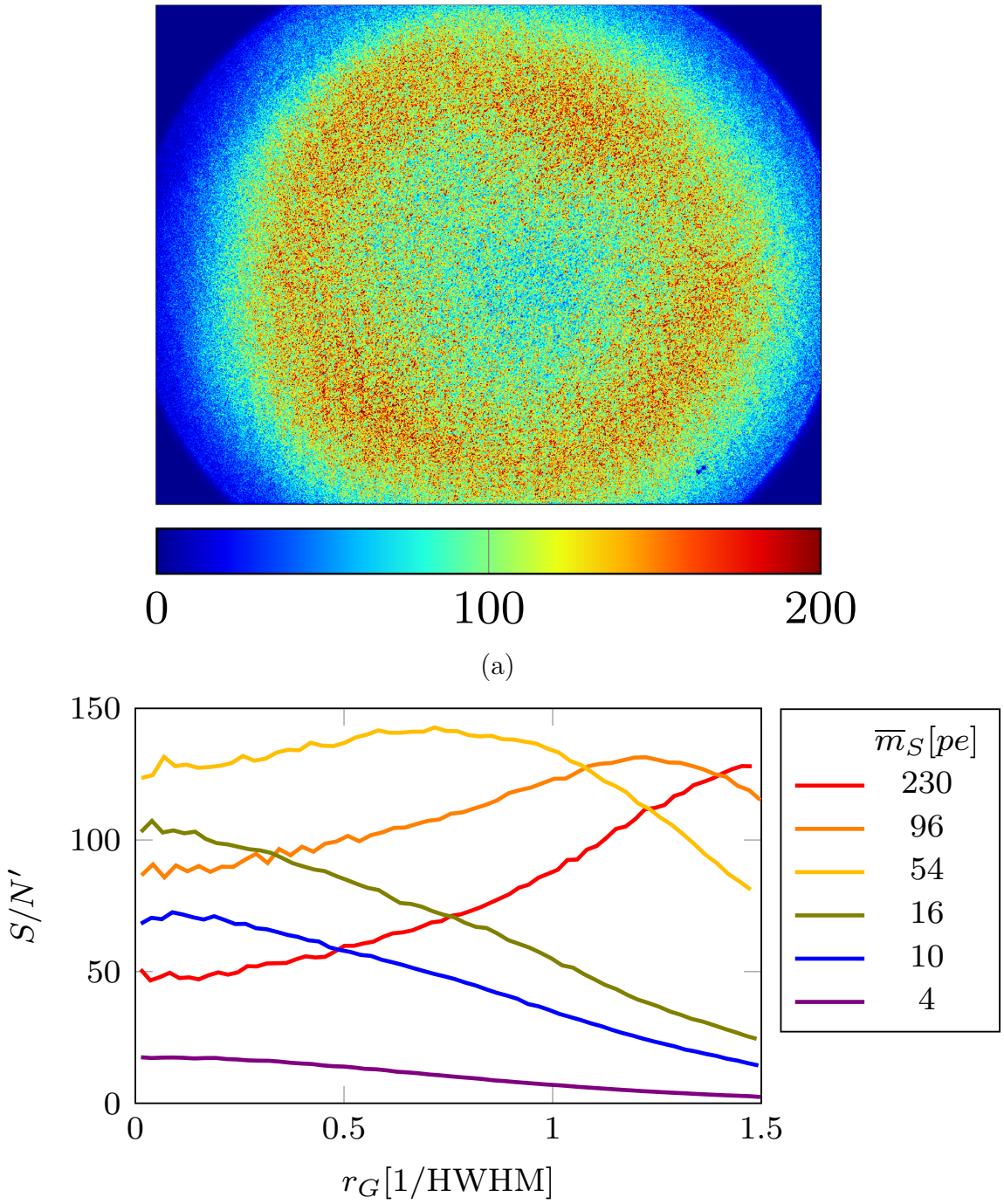

Figure 4.11. (a) The measured SNR S/N' for dataset 5, where $\overline{m}_S = 96\,pe$. (b) The azmuthial average of S/N' for each dataset.

quantifies the spatial effects of the non-Gaussian shape.

Next, we show a radial comparison across the datasets in Fig. 4.12(b). In dataset

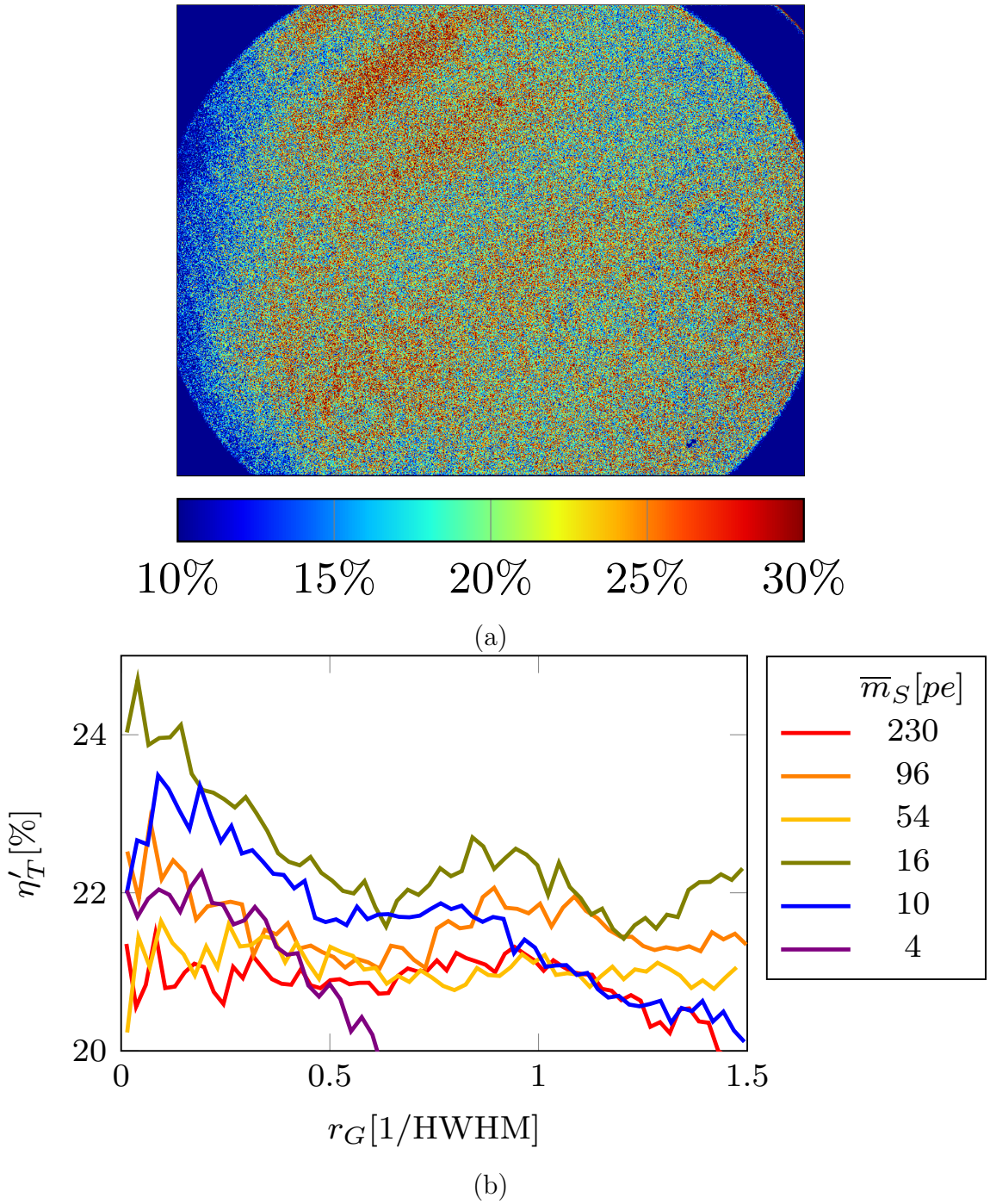

Figure 4.12. (a) The total system efficiency η'_T for dataset 5 where $\overline{m}_S = 96\,pe$. (b) The azmuthial average of η'_T for each dataset.

1, where $\overline{m}_S = 4\,pe$, we saw this calculation fall quickly from the Gaussian peak. This outcome was due to the very weak signal, where the signal fell below the camera

noise in the Gaussian profile wings. For the remaining datasets, the η'_T radial average exhibited a wave, which appeared consistent with the reference etalon pattern. We had assumed our measured SNR was directly proportional to the signal strength, which means we should have the same spatial distribution as the signal frame. The non-uniform reference affected $\overline{E}_H$, as seen in Fig. 4.4(b), as compared to the average signal frames in Fig. 4.4(g). This outcome led us to believe the non-uniform reference has some effect on the SNR even with subtracting out $\overline{E}_N$ and dividing out η'_n, which contains the spatial nature of the reference.

For a comparison to η'_T, we updated Table 4.1, which contained our major system efficiencies, with our measurements in Table 4.5. We excluded the signal-noise efficiency η'_S because we used it in Eq. (4.11). Multiplying all the efficiencies together gave an $\eta_T = 22.7\% \pm 6.5\%$.

To compare to our expected η_T of 22.7%, we took a spatial average of the $\eta'_T(x, y)$ frames from about $r_G = 0 - 1.5$ for datasets 2-6 and $r_G = 0 - 0.5$ for dataset 1, where there was detectable signal for the measurement. We show the results in Fig. 4.13. The error bars, whose widths are one standard deviation, are around 6 - 6.5%. Both the measured and expected total-system efficiency's uncertainty fall within a half of the standard deviation. Across the six datasets, the average was $\eta'_T = 21.2\%$ with $\sigma_{\eta_T} = 6.3\%$. We presumed the minor differences between datasets were due to minor laser or system fluctuations throughout the data collection, which occurred over several hours in two days.

In the previous experiment (cf. Appendix D), we had a $\eta_t = 99\%$, $\eta_q = 50\%$, $\eta_m = 30.9\%$, and $\eta_R = 50.0\%$, which yielded a $\eta_T = 7.7\%$ with an uncertainty of 1.1%. We took three datasets at $\overline{m}_S = 13.9\,pe$, $32.3\,pe$, and $39.5pe$. The measured total-system efficiencies were $\eta'_T = 8.5\%$, 7.6%, and 7.2%. This outcome resulted in an average $\eta'_T = 7.8\%$ with $\sigma_{\eta'_T} = 2.9\%$. The major differences with this experiment

Table 4.5. Updated system efficiencies

Name	Value ± Uncertainty	Source
transmission, η_t	99.7% ± 0.05%	Vendor
quantum, η_q	83% ± 0.5%	Vendor
mixing, η'_m	36.8% ± 10.2%	Table 4.4
reference noise, η'_R	74.5% ± 2.0%	Table 4.4
total, η_T	22.7% ± 6.5%	Calculated

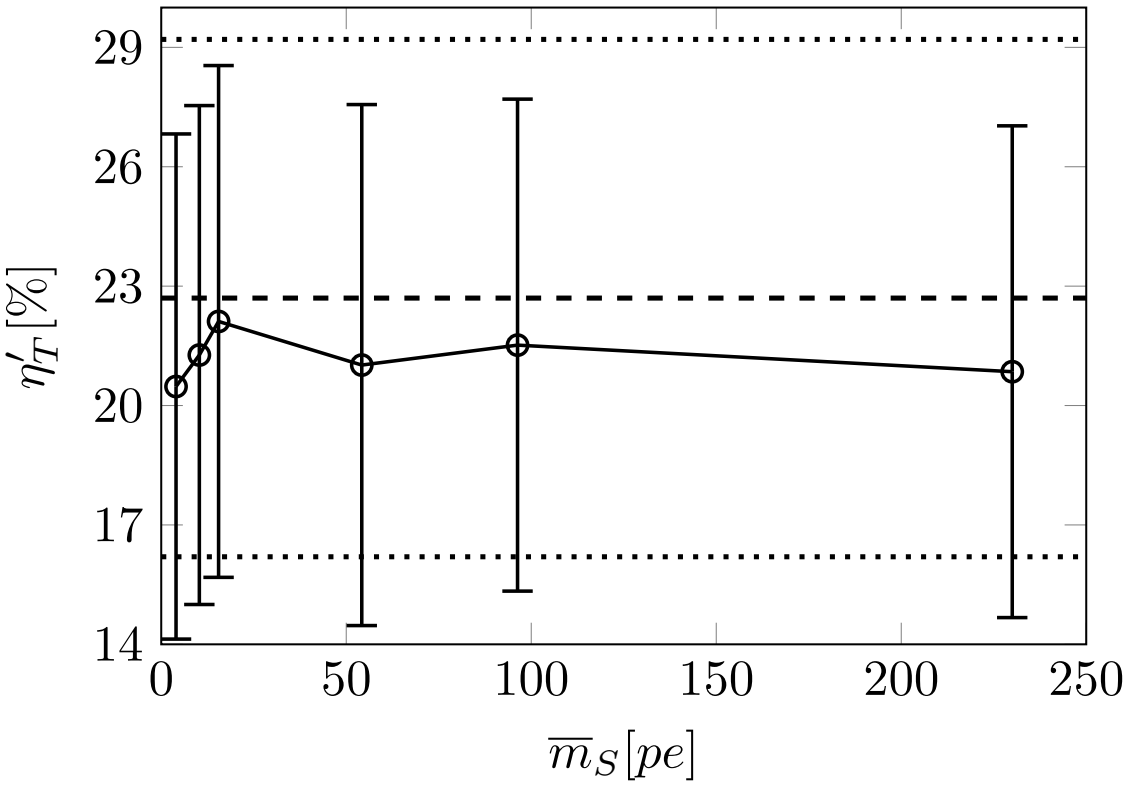

Figure 4.13. Pixel averaged measured total system efficiency η'_T for the six datasets, where the width of the error bars represent the standard deviation, the dashed line represents the expected value of 22.7% and the dotted lines are $\pm\sigma_{\eta'_T} = 6.5\%$.

was a different vendor for the MO laser and more noise (cf. Table D.1 in Appendix D). However, the results from two-separate experiments further supported that we have quantified all of the major system efficiencies.

4.5 Conclusion

In this paper, we showed that the major system efficiencies (multiplicative losses) of our DH system under test were the mixing, reference-noise, and signal-noise efficiencies (i.e., η_m, η_R, and η_S, respectively). From the collected experimental data, we measured the following values for these efficiencies using a DH system in the off-axis IPRG: $\eta'_m = 36.8\%$, $\eta'_R = 74.5\%$, and $\eta'_S = 3\% - 100\%$. In turn, our measured value of 36.8% for η'_m was 4.6% higher than our expected value of 32.2% for η_m using an ideal-sinc model for the pixel MTF. We suspected that our pixel MTF differs from an ideal-sinc model because the FPA used microlenses to achieve a 100% pixel-fill factor. Additionally, we found that the reference noise was about 34% greater than that obtained with Poisson-distributed shot noise. Along with laser-amplitude noise, we saw that the reference non uniformity compounds this excess noise. Next, we observed that the signal-noise efficiency was dependent on the signal strength at higher SNRs (e.g., an SNR > 100). Due to sampling of the pupil-autocorrelation term in the Fourier plane, we saw that the demodulated-signal noise was proportional to the square of the signal strength $\overline{m}_S$ and increased faster than the signal shot noise.

With these efficiency measurements, we modified our expected total-system efficiency η_T from 27.5% to 22.7% (cf. Table 4.1 and 4.5). As such, we measured the average total-system efficiency $\eta'_T = 21.1\%$, which was 1.6% less than expected. These measurements fell within the error bounds of both the expected and measured total-system efficiency. We also achieved similar results with the data from a previous experiment, where the η_T was 7.7% and η'_T was 7.8%.

Overall, our results show that reaching the ideal, mixing-efficiency limit for a DH system is difficult without consideration of the excess signal and reference noise. We can mitigate excess signal noise, in practice, by decreasing the Fourier-plane sampling ($q_I \gtrsim 4$) and moving the pupil location further from the Fourier-plane cen-

ter. However, when the excess signal noise becomes significant, the SNR $\gtrsim$ 100. With deep-turbulence wavefront sensing, for example, we generally need a SNR $>$ 10, and we desire maximum Fourier-plane sampling ($2 \lesssim q_I \lesssim 4$). We should also take precautions to increase the reference uniformity and reduce the laser-amplitude noise to maximize the reference-noise efficiency. Therefore, the DH system efficiency could approach the ideal mixing-efficiency limit under the strong-reference assumption with highly transmissive optics, highly efficient FPAs, and a near-uniform and low amplitude-noise reference.

V. Digital holography experiments with degraded temporal coherence

The contents of this chapter is a draft for submission to the *Holography* special section of *Optical Engineering* [78].

To simulate the effects of multiple-longitudinal modes and rapid fluctuations in center frequency, this paper uses sinusoidal phase modulation and linewidth broadening, respectively. These effects allow us to degrade the temporal coherence of our master-oscillator laser, which we then use to conduct digital holography experiments. In turn, our results show that the coherence efficiency decreases quadratically with fringe visibility and that our measurements agree with our models to within 1.8% for sinusoidal phase modulation and 6.9% for linewidth broadening.

5.1 Introduction

Recent results show that digital holography (DH) is an enabling technology for tactical applications, such as deep-turbulence wavefront sensing [20, 21, 39] and long-range imaging [79, 80, 17]. By flood illuminating a distant object and interfering the scattered signal with a local reference, we can reconstruct the amplitude and phase of the complex-optical field. Furthermore, we can approach the shot-noise limit, given a strong reference [81]. Recent experiments quantified the validity of this last statement in terms of system efficiencies [65]. While these experiments showed that DH is robust against weak signals often encountered in tactical applications, they assumed the use of fully coherent laser sources when formulating closed-form expressions for the signal-to-noise ratio (SNR).

With coherence in mind, Mandel evaluated the temporal coherence requirements for analog holography in 1966 [82]. From this foundational work, Harris et al. studied the role of coherence length in continuous wave (cw) coherent-lidar systems [83].

Recall that coherent lidar uses temporal modulation, whereas DH uses spatial modulation. Because of this difference, cw coherent-lidar systems can operate with ranges many orders of magnitude beyond the coherence length of the master-oscillator (MO) laser [84, 85, 86]. In contrast, DH systems cannot, since the hologram interference fringes wash out when the path length differences between the signal and reference are greater than the coherence length of the MO laser.

Claus et al. studied the coherence requirements associated with cw DH systems but with near-equal path lengths between the signal and reference [87]. In contrast to digital-holographic microscopy, where short laser coherence lengths enable three-dimensional imaging [5], the effective ranges for tactical applications becomes limited by both the coherence length and the signal strength. With this last point in mind, Marron et al. successfully conducted field experiments with a DH system using a coherence length >200 m and a range of 100 m [10]. It is unclear, however, whether the path length difference between the signal and reference reduced the fringe visibility, since this detailed information is absent from Ref. [10], in addition to an estimate of the system efficiencies (multiplicative losses), which degrade the achievable SNR.

From our work in Ref. [65], we know that the ideal total-system efficiency becomes limited to about 30%. This limit is primarily due to depolarization from rough surface scattering and the pixel modulation transfer function. Other efficiencies, including those caused by excess reference and signal noise, can further degrade the fringe visibility. On top of these system efficiencies, several independent phenomenon (not studied in Ref. [65]) can further degrade the temporal coherence of the MO laser, and subsequently, the fringe visibility of a DH system. For example, increasing the integration time on the focal-plane array (FPA) can reduce the fringe visibility due to fluctuations in the center frequency of the MO laser. High-power laser sources can also exhibit time-evolving longitudinal modes, leading to degraded temporal co-

herence. In our opinion, these independent phenomena have largely been ignored in previous studies and leads us to the DH experiments presented here.

This paper explores the effects of degraded temporal coherence, given a DH system in the off-axis image plane recording geometry (IPRG). To degrade the temporal coherence of our MO laser, we use two approaches: sinusoidal phase modulation and linewidth broadening. The sinusoidal phase modulation produces spectral side bands and allows us to simulate the effects of multiple-longitudinal modes in our MO laser. Phase modulation via pseudo-random bit sequences (PRBS) then allows us to broaden the linewidth of our MO laser and simulate the effects of rapid fluctuations in the center frequency. Before moving on to the next section, it is worth mentioning that the experimental setup used here may also enable the characterization of high-power fiber lasers, where one might broaden the linewidth of the seed to reduce the effects of stimulated Brillouin scattering [88, 89].

In what follows, we show that the coherence efficiency depends on the square of the complex-degree of coherence (Sections 5.2-5.4). In Section 5.2, we develop the relationship between coherence efficiency and the complex-degree of the coherence, whereas in Section 5.3, we describe our experimental setup and how we measure the coherence efficiency. Section 5.4 follows with analysis and results of the measured and modeled coherence efficiency. Last, Section 5.5 provides a conclusion for this paper.

5.2 Coherence efficiency, η_c

With DH, we interfere the signal with a reference, and we demodulate the resulting digital hologram to obtain an estimate of the amplitude and phase of the complex-optical field. As such, the instantaneous hologram irradiance, i_H, is the square magnitude of the sum of the signal complex-optical field, U_S, and reference

complex-optical field, U_R, such that

$$\begin{aligned} i_H(t,\tau) = &|U_R(t)|^2 + |U_S(t+\tau)|^2 \\ &+ U_R^*(t)U_S(t+\tau) + U_R(t)U_S^*(t+\tau), \end{aligned} \tag{5.1}$$

where t is time, τ is the time delay between the signal and reference, and * denotes complex conjugate. For simplicity in the notation, Eq. (5.1) neglects any spatial dependencies. Here, we assume that the instantaneous reference irradiance (first term) is spatially uniform and that the instantaneous signal irradiance (second term) is negligible given a strong reference and a weak signal. The third and fourth terms involving U_S have the important spatial content. For example, with the tilted reference provided by an off-axis local oscillator (LO), the third and forth terms of Eq. (5.1) produce the spatial fringes in i_H and shift these terms away from DC in the spatial Fourier domain of i_H. With these shifts in mind, we window the third term in the spatial Fourier domain and transform back to the spatial domain to obtain an estimate $\widehat{U}_S$. The precision of $\widehat{U}_S$ depends on the SNR of the DH system.

As with previous works, we use the power definition of the SNR, S/N [65], such that

$$S/N = \eta_T \frac{4q_I^2}{\pi} \frac{\overline{m}_R \overline{m}_S}{\overline{m}_R + \overline{m}_S}, \tag{5.2}$$

where η_T is the total-system efficiency, $4q_I/\pi$ is the noise compression factor, and $\overline{m}_R$ and $\overline{m}_S$ are the mean photoelectron count for the reference and signal, respectively. In practice, $\overline{m}_R$ and $\overline{m}_S$ follow as

$$\overline{m}_R = \frac{t_i p^2}{h\nu} \left\langle |U_R(t)|^2 \right\rangle \quad \text{and} \quad \overline{m}_S = \frac{t_i p^2}{h\nu} \left\langle |U_S(t+\tau)|^2 \right\rangle, \tag{5.3}$$

where $t_i p^2/h\nu$ is the irradiance to photonelectron conversion factor (assuming the quantum efficiency is 100%) and $\langle \cdot \rangle$ denotes a time average that is much longer than

the temporal period of the MO laser. In the last term of Eq. (5.2), the numerator is the heterodyne energy and the denominator is the noise energy. With respect to the noise energy, we include only the shot noise associated with the reference and signal and assume other noise sources, such as background noise and FPA read noise, are negligible. Furthermore, η_T contains all the system efficiencies (multiplicative losses) that degrade the fringe visibility, such as optical transmission losses through the atmosphere and receiver optics, the quantum efficiency of the FPA, the mixing efficiency of the signal and reference, etc. [65].

The mixing efficiency is how well the detected reference and signal interfere, and thus produce fringes. For example, phenomenon like rough-surface scattering from a dielectric object depolarizes the signal and decreases the mixing efficiency by 50%, thus decreasing the visibility of the fringes. A degradation in temporal coherence also leads to a reduction the fringe visibility. Given a cw laser source, the fringe visibility is equivalent to the magnitude of the complex-degree of coherence $\gamma(\tau)$ [37], which we can calculate in terms of U_S and U_R, viz.

$$\gamma(\tau) = \frac{\langle U_S(t+\tau)U_R(t)^* \rangle}{\langle U_S(0)U_R^*(0) \rangle}, \tag{5.4}$$

where $\langle \cdot \rangle$ represents a time average that is much longer than the temporal period of the laser. The numerator of Eq. (5.4) represents a cross correlation and the denominator normalizes γ. Thus, the magnitude of γ is a measurable quantity ranging from $\gamma = 1$ (ideal coherence) to $\gamma = 0$ (incoherent).

The heterodyne energy in Eq. (5.2) assumes ideal coherence between the reference and signal. To quantify the coherence effects in terms of a multiplicative efficiency factor for in the total-system efficiency, η_T, we introduce the coherence efficiency, η_c. Since we use a power definition for SNR, S/N, the complex degree of coherence, γ,

relates to η_c as

$$\eta_c(\tau) = |\gamma(\tau)|^2 . \tag{5.5}$$

Therefore, the S/N and heterodyne energy is proportional to the square of the fringe visibility. Note that this outcome is the same conclusion as Goodman for the amplitude interferometer [36]. For example, say the MO laser has a Lorentzian spectrum and the time delay τ between the reference and signal is equal to the coherence time, τ_c, (as defined by Mandel [38]). The MO laser spectrum (i.e., the power spectral density) and γ are Fourier transform pairs via the Wiener-Khinchin theorem [36]; thus, γ is a decaying exponential. This example results in $\gamma = 0.368$, $\eta_c = 13.5\%$, and the DH heterodyne energy and S/N reduces by 86.5%. In terms of the effective range of a practical DH system, here, the path length difference between the reference and signal, $\Delta\ell$, corresponds to the coherence length ,ℓ_c, where $\ell_c = \tau_c c$ and c is the speed of light. Therefore, operating a DH system at $\Delta\ell \geq \ell_c$ is detrimental to the achievable SNR and limits the effective range to $\lesssim \ell_c/2$, assuming the signal travels much further to the object and back as compared to the reference.

5.3 Experimental methods

The goal of the experiments presented here was to manipulate the MO laser spectrum with different phase modulation schemes and to quantify the temporal coherence effects in DH by measuring the coherence efficiency, η_c. To that end, we provide the details on the DH experimental setup and the η_c measurements in this section. This work builds upon the results from Mao [90], which contains additional details.

5.3.1 Experimental set-Up

In our experiments, we setup our DH system in the off-axis IPRG as illustrated in Fig. 5.1. Here, the MO laser was a Cobalt Samba 1000 cw diode pumped solid

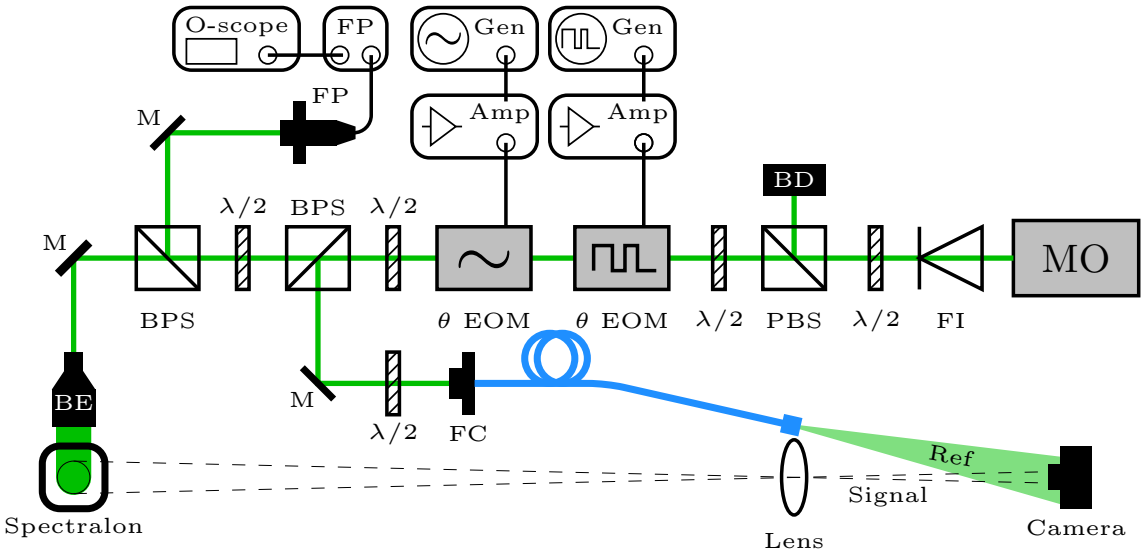

Figure 5.1. An overview of the experimental setup.

state laser with a wavelength of 532.1 nm, a linewidth of ¡ 1 MHz, a $\ell_c < 100\,\text{m}$, and an output power of 1 W. We used a Faraday isolator (FI) to isolate the MO laser from back reflections. To create the various optical trains found in Fig. 5.1, we used pairs of half-wave ($\lambda/2$) plates between a polarizing beam splitter (PBS) to direct (1) unneeded MO laser power to a beam dump (BD), (2) to a fiber coupler (FC) for the reference, and (3) to a Fabry-Perot (FP) interferometer. The $\lambda/2$ plates also allowed us to match polarization to the phase electro-optic modulators (θ EOM) and the polarization-maintaining fiber for the reference.

To create the signal, we used a mirror (M) to steer the MO laser into a 20x beam expander (BE) to illuminate a sheet of Lapsphere Spectralon. By design, the Spectralon was 99% Lambertian and provided an optically-rough dielectric object. After, we imaged the near-Gaussian spot scattered by the Labsphere Spectralon with a 1 in lens onto a Grasshopper3 camera (GS3-U3-32S4M-C). Here, the object distance and the focal length was 246 cm and 35 cm, respectively. To create the tilted reference, we placed the off-axis LO next to the lens. Next, we flood illuminate the camera with the tilted reference and collected digital holograms with a camera integration time

of 250 μsec. This integration time corresponds to a sampling frequency of 4 kHz and is more than three orders of magnitude less than lowest phase-modulation frequency. Therefore, we can safely assume our measurements were not dependent on the integration time.

The first phase EOM was a ConOptics 350-160 with a ConOptics 25D amplifier. We converted it from an amplitude EOM by removing the output polarizer and aligning the laser polarization to one of the EOM crystals' axis. This configuration gave a half-wave voltage, V_π, of 277 V at 532.1 nm. The 25D amplifier was a digital amplifier with a bandwidth from DC - 30 MHz and maximum output voltage of 175 V. To produce linewidth broadening on the MO laser, we used a PRBS input signal with a bit length of 2^{31} and frequencies from 15 MHz to 30 MHz. This broaden the MO laser energy by 62-68%.

The second phase EOM was a ConOptics 360-40 with $V_\pi = 155$ V at 532.1 nm. We used a ConOptics 550 amplifier with this EOM, which had a bandwidth of 20-500 MHz and maximum output of 125 volts peak-to-peak, V_{pp}. Using a sinusoidal input signal, we generated sidebands on the MO laser with modulation frequencies of 20-100 MHz and adjusted the sideband amplitudes by changing the input signal V_{pp}.

To measure the optical spectrum of the phase modulated MO laser, we used a ThorLabs SA30-52 Fabry-Perot interferometer with a finesse of 1500 and free-spectral range (FSR) of 1.5 GHz, which provided a spectral resolution of <1 MHz. The MO laser manufacturer specified linewidth was also <1 MHz. In turn, the FP mirrors were scanned over a range >FSR so that two peaks appeared per scan to convert the recorded FP signal time to relative frequency. We captured multiple scans on the oscilloscope to average the FP output signal and lower the noise. Figure 5.2 shows the averaged FP spectrum of the unmodulated MO laser spectrum fitted to a Lorentzian

lineshape $\mathcal{L}(\nu, \Delta\nu)$ as defined as

$$\mathcal{L}(\nu) = \frac{\pi}{2} \frac{\Delta\nu_L}{(\nu - \nu_0)^2 + \left(\frac{\Delta\nu_L}{2}\right)^2}, \tag{5.6}$$

where ν is the MO laser frequency, ν_0 is the center MO laser frequency, $\Delta\nu_L$ is the full width at half max (FWHM), and A_L is the Lorentzian lineshape amplitude. From Fig. 5.2, we observed some minor higher-order modes hidden in the noise after averaging, which we assumed to be from the FP alignment and not the MO laser. We chose to fit a Lorentzian lineshape because the lineshape of an FP interferometer of high finesse is well approximated by a Lorentzian lineshape [91] and we assumed the MO laser lineshape was near Lorentzian lineshape [92]. The observed unmodulated FHWM was $\Delta\nu_L = 1.2 \pm 0.05\,\text{MHz}$, which suggests the MO laser linewidth was narrower than specified because the observed linewidth is equal to the sum of the FP and MO laser linewidths. The FP manufacturer indicated that the typical best FP linewidth was 700 kHz. With these points in mind, we used a $\Delta\nu_L = 500\,\text{kHz}$ for the ensuing analysis with PRBS modulation.

5.3.2 Data measurements

To measure the coherence efficiency, η_c, for the different phase modulation schemes and path length differences, we measured the heterodyne energy in the Fourier plane. We maximized the heterodyne energy in the digital hologram by setting the reference at 50% of the pixel full-well depth and increased the signal strength slightly below pixel saturation. The unmodulated SNR was around 110-120 which gave us the desired dynamic range for the measurements. On each digital hologram, we performed an inverse discrete Fourier transform ($\mathcal{DFT}^{-1}$) and took the magnitude squared to convert the Fourier plane to real-valued energy quantities. Then, we windowed the total energy, E_T, contained in the circular pupil in the Fourier plane as depicted

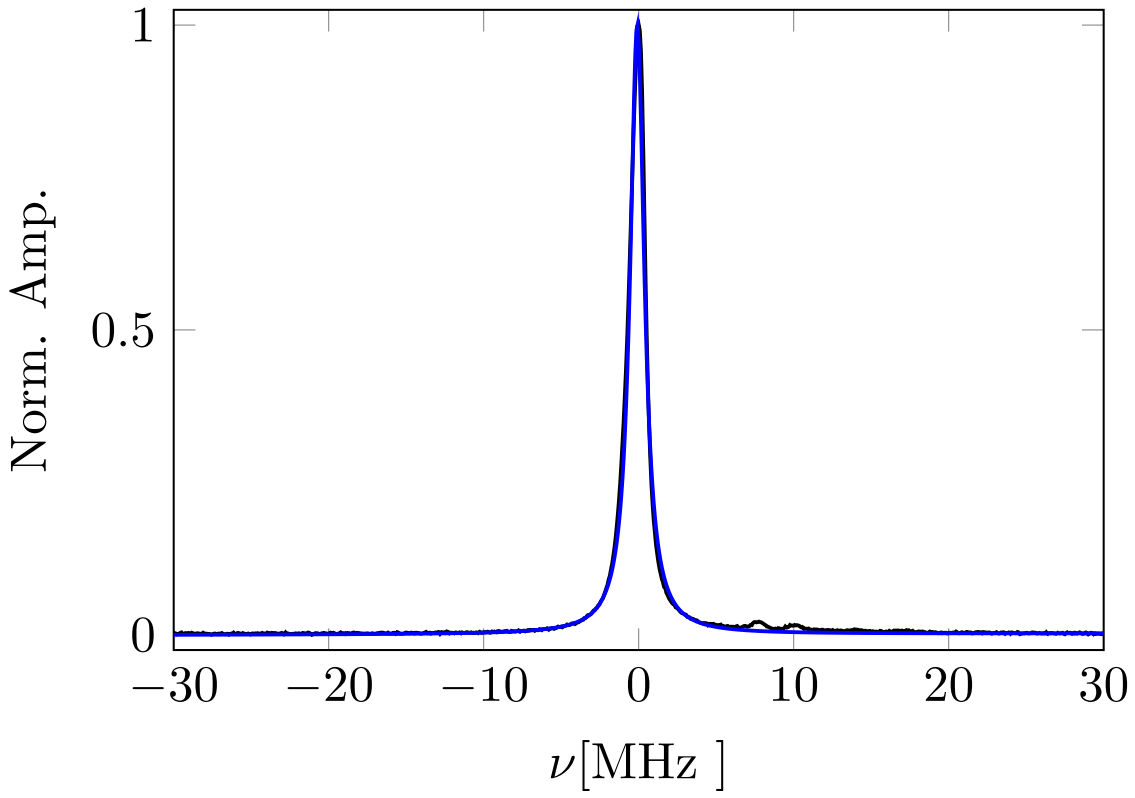

Figure 5.2. The average unmodulated MO laser spectrum from the FP interferometer (−) with a Lorentzian lineshape fit (−).

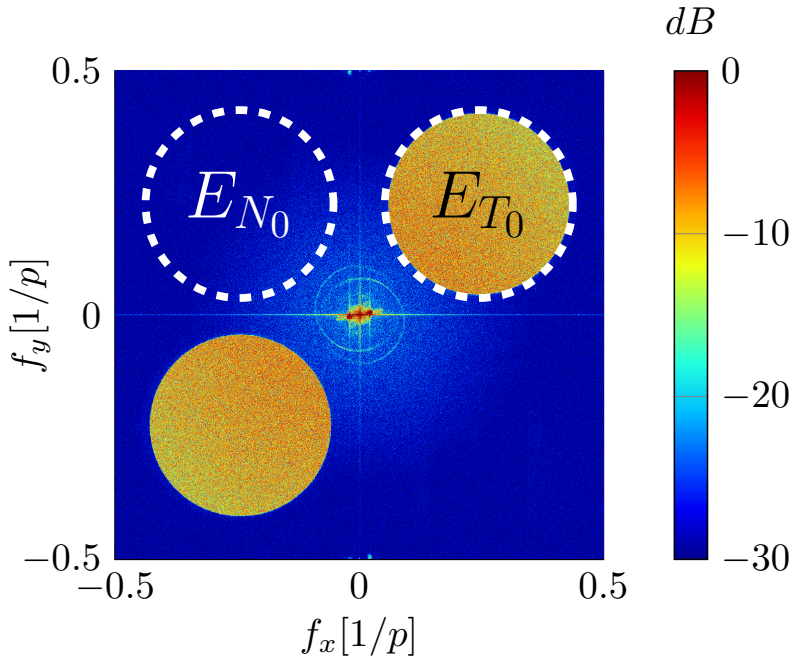

(a)

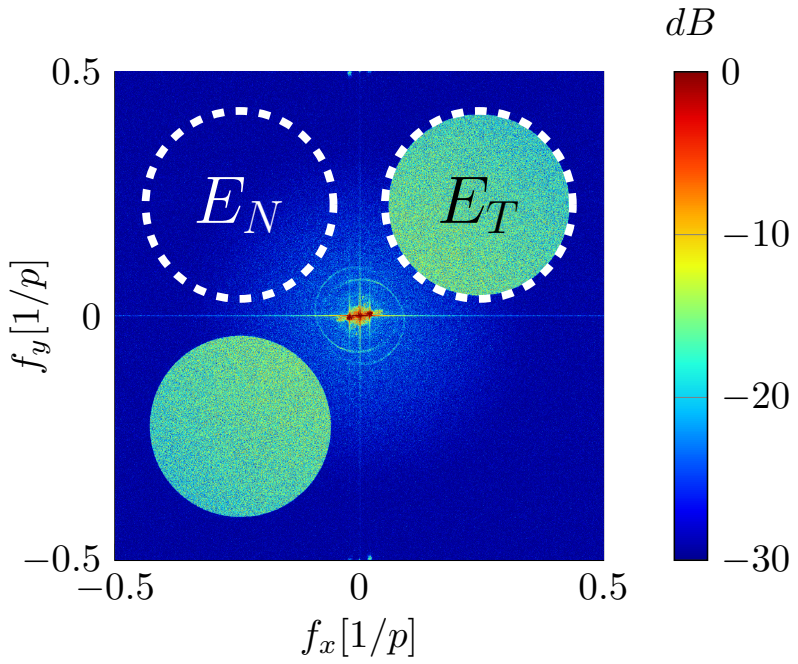

(b)

Figure 5.3. The Fourier plane of (a) an unmodulated digital hologram and (b) a 20 MHz sinusoidal modulated digital hologram with $\Delta\ell = 3.1\,\mathrm{m}$.

in Fig. 5.3. However, this window contained noise in addition to the heterodyne energy, E_H. To estimate the noise energy, E_N, we assumed that the Fourier plane was symmetric and windowed an adjacent quadrant that did not contain a circular pupil, also depicted in Fig. 5.3. Then, we flipped E_N and subtracted E_N from E_T to determine E_H.

Because the strengths of signal and reference were not identical at each $\Delta\ell$, we collected 100 unmodulated digital holograms and 100 modulated digital holograms at the various modulation frequencies. We then measured the relative coherence efficiency $\hat{\eta}_c'$, which is the ratio of the modulated E_H to the unmodulated E_{H_0}, viz.

$$\hat{\eta}_c'(\tau) = \frac{E_H}{E_{H_0}} = \frac{\eta_c(\tau)}{\eta_{c_0}(\tau)}, \tag{5.7}$$

where $\hat{\eta}_c'$ is also the ratio of the modulated η_c to the unmodulated η_{c_0}. Note that this relationship creates a relative measurement because E_{H_0} has a minor η_c loss due to the path length differences. However, we did observe some minor reference power loss when the phase EOMs were on. We suspect that this loss was due to a minor change in the beam quality through the EOM crystal, which produced a fiber-coupling loss for the reference. Therefore, we normalized the E_H and E_{H_0} measurements to the mean hologram photoelectron count which countered the minor reference power loss.

5.4 Analysis and results

This section presents the analysis and results for the measured relative coherence efficiency, $\hat{\eta}_c'$ (cf. Eq. 5.7), with respect to the sinusoidal, PRBS, and combined phase modulation schemes. Sinusoidal phase modulation produced sidebands on the MO laser spectrum while PRBS phase modulation produced linewidth broadening. Phase modulation, in general, is a non-linear process with respect to frequency [24]. As

such, non-ideal hardware performance produced spectra different from expected. In what follows, we first present the FP interferometer measurements, which we used to more accurately represent the actual spectra for our model of $\hat{\eta}_c$, so that we could compare to our measurements of $\hat{\eta}_c'$.

5.4.1 Sinusoidal modulation

To model the sinusoidal phase modulation, we represented the MO laser complex field $U(t)$ as a Bessel series [93], such that

$$\begin{aligned} U(t) =& U_o J_0(\phi) \cos\left[2\pi\nu_o t\right] \\ &+ U_o \sum_{k=1}^{\infty} J_k(\phi)\{\cos\left[2\pi\left(\nu_o + k f_{m,s}\right)\right] \\ &+ (-1)^k \cos\left[2\pi\left(\nu_o - k f_{m,s}\right)\right]\}, \end{aligned} \tag{5.8}$$

where U_o is the unmodulated MO laser amplitude, J_k is the sideband amplitude, ϕ is the depth of phase modulation, ν_0 is the MO laser frequency, and $f_{m,s}$ is the sinusoidal phase modulation frequency. Note that J_k are Bessel coefficients of the first kind and the sum of the squared Bessel coefficients equals 1 to conserve energy. Also note that we assumed monochromaticity with the cosines in Eq. (5.8). We approximated the sinusoidal phase modulated spectrum, $G_s(\nu)$, as

$$\begin{aligned} G_s(\nu) =& \mathcal{L}\left(\nu\right) \Big\{ J_0^2(\phi) \\ &+ \sum_{k=1}^{\infty} J_k^2(\phi)[\delta\left(\nu_o + k f_m\right) + \delta\left(\nu_o - k f_m\right)] \Big\}, \end{aligned} \tag{5.9}$$

where $\mathcal{L}(\nu_0)$ is the Lorentzian MO laser lineshape [cf. Eq. (5.6)] and $\delta(\nu)$ is the unit impulse function, which represents the phase modulation induced sidebands. Here, we assumed that the cross-terms are negligible since $\Delta\nu_L \ll f_m$.

We collected data from $f_{m,s} = 20$ - 100 MHz in five MHz steps at $\phi = 0.4\pi$ & 0.8π. Figure 5.4 shows a few of the collected FP spectra for the sinusoidal phase modulation. We observed that the sideband amplitudes did not align well with the theoretical Bessel coefficients, were asymmetric, and varied measurably for each $f_{m,s}$ and ϕ. In turn, we calculated the average absolute percent error of the sideband amplitudes, ΔA_k, as

$$\Delta A_k(\phi) = \frac{100}{17} \sum_{f_{m,s}=20\,MHz}^{100\,MHz} \frac{1}{2\alpha+1} \sum_{k=-\alpha}^{\alpha} \frac{|A_k\left(f_{m,s},\phi\right) - J_k^2(\phi)|}{J_k^2(\phi)} \tag{5.10}$$

where $f_{m,s}$ ranged from 20-100 MHz in 5 MHz increments, α is the number of sidebands included (i.e., $\alpha = 2$ for $\phi = 0.4\pi$ and $\alpha = 4$ for $\phi = 0.8\pi$), and A_k^2 was the FP measured sideband amplitude. These calculations resulted in $\Delta A_k(0.4\pi) = 16\%$ and $\Delta A_k(0.8\pi) = 241\%$. We believe that this discrepancy is due to the non-ideal performance of the hardware such as the input sinusoidal signal having some bandwidth and not significant FP alignment errors. Therefore, we measured the sideband amplitudes from the FP interferometer to substitute for the Bessel coefficients in the $\hat{\eta}_c$ model predictions. Each k^{th}-order sideband had two FP amplitude measurements, so we took the average of the two amplitudes for the corresponding A_k value.

Since $G(\nu)$ and $\gamma(\tau)$ are Fourier transform pairs, the γ_s for the sinusoidal phase modulation resulted in

$$\begin{aligned}\gamma_s(\tau,\phi,f_{m,s}) =& e^{-\pi\Delta\nu\tau}\left\{A_0(\phi,f_{m,s})\right. \\ &\left. +2\sum_{k=1}^{\infty} A_k(\phi,f_{m,s})\cos(2\pi k f_{m,s}\tau)\right\},\end{aligned} \tag{5.11}$$

where A_k was the sideband amplitude measurements from the FP, the exponential was from the unmodulated MO laser (i.e., the Lorentzian lineshape), and the cosine was the result of the spectral shifts from the sidebands in Eq. (5.9). Put another way,

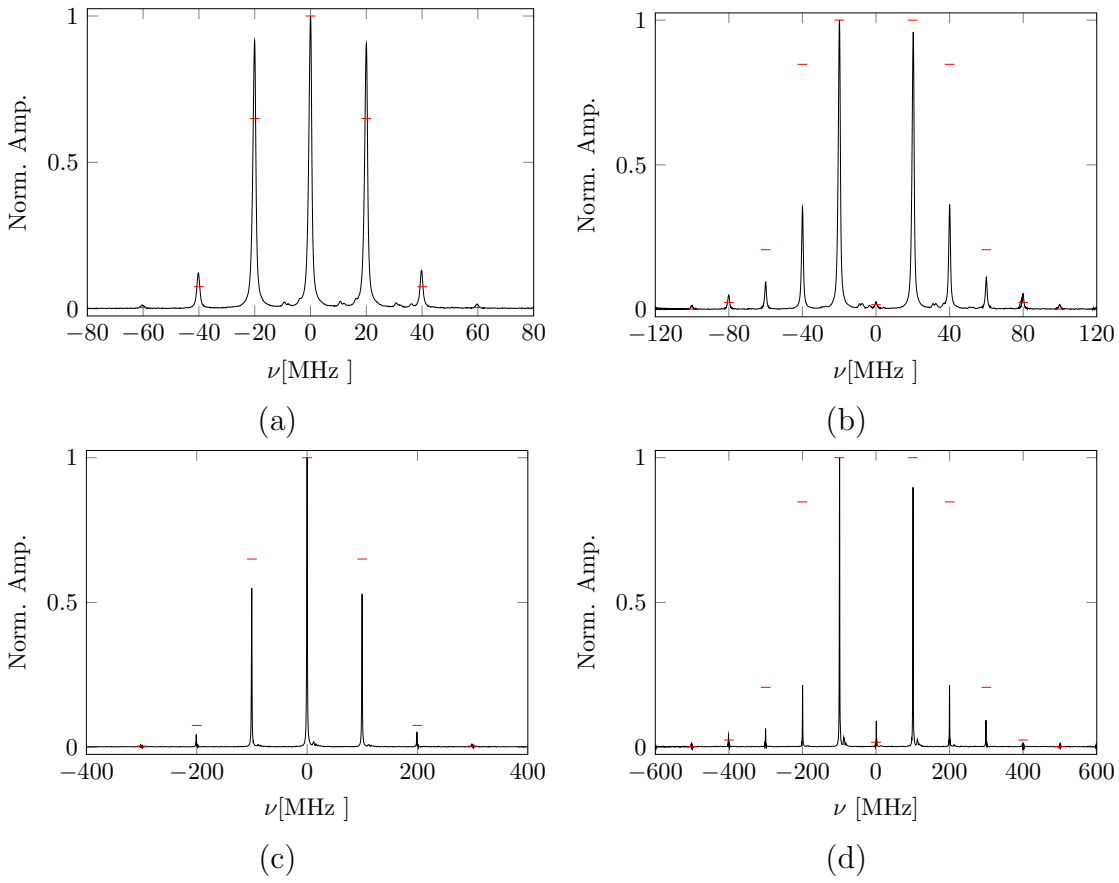

Figure 5.4. The average FP spectra (−) of the sinusoidal phase modulated MO laser at $f_{m,s}$ = 20 MHz in (a) and (b) and $f_{m,s}$ = 100 MHz in (c) and (d) with $\phi = 0.403\pi$ in (a) and (c) and $\phi = 0.806\pi$ in (b) and (d). The theoretical Bessel amplitudes are denoted as (−).

γ_s was a series of beating cosines resulting from the sidebands with an exponential decaying envelope from the MO laser linewidth. Note that we normalized the Bessel coefficients in Eq. (6.2) (i.e. $1 = J_0^2(\phi) + 2\sum_{k=1}^{\infty} J_k^2(\phi)$). As such, we normalized the measured $A_k's$ in a similar fashion, which also normalizes $\gamma_s(\tau)$, so that the values range from zero to one. Since the $\hat{\eta}_c'$ measurements were relative [cf. Eq. (5.7)], our model for $\hat{\eta}_{c,s}(\tau)$ was

$$\hat{\eta}_{c,s}(\tau, \phi, f_{m,s}) = \left\{ A_0(\phi, f_{m,s}) + 2\sum_{k=1}^{\infty} A_k(\phi, f_{m,s}) \cos(2\pi k f_{m,s}\tau) \right\}^2, \tag{5.12}$$

where the exponential from the unmodulated MO laser was divided out by E_{H_0}. Note that$\hat{\eta}_{c,s}$ shows our $\hat{\eta}'_{c,s}$ was solely dependent on the sinusoidal phase modulation and not the unmodulated MO laser linewidth.

Figure 5.5 shows $\hat{\eta}'_{c,s}$ compared to $\hat{\eta}_{c,s}$ [cf. Eq. (5.12)] with the FP measured amplitudes (A_k) and the theoretical (J_k). We observed in Fig. 5.5 (a-b) that $\hat{\eta}'_c$ approaches 0%, when the sidebands destructively interfere, and approaches 100%when the sidebands constructively interfere, due to the beating sidebands [cf. Eq. (5.11)]. As we increased $\Delta\ell$, the beating sidebands became more apparent as shown in Fig. 5.5 (c), where $\phi = 0.4\pi$ and $\Delta\ell = 22.4\,\mathrm{m}$. We took advantage of this sinusoidal structure to better determine the value of τ (i.e., $\tau = \Delta\ell/c$), since we had some uncertainty to the value of τ for Eq. (5.12). This uncertainty was from the reference fiber optical path length because we we didn't have the exact refractive index value at the MO laser wavelength. Therefore to estimate τ, we minimized the error between the DH measured $\hat{\eta}'_c$ and $\hat{\eta}_{c,s}$. The results yielded a $\Delta\ell = 3.1\,m$ for Fig. 5.5 (a -b) and $\Delta\ell = 22.4\,m$, which were within a few centimeters of the measured $\Delta\ell$ when assuming the fiber's refractive index ≈ 1.50. Note that this path length difference measurements was also used for the PRBS phase modulation analysis.

The average absolute difference $\hat{\eta}'_{c,s}$ and $\hat{\eta}_{c,s}$ is shown in Table 5.1. We found that our A_k's improved $\hat{\eta}_{c,s} \approx 10\%$ more for $\phi = 0.8\pi$ than for $\phi = 0.4\pi$. This improvement occurred not only because $\Delta A_k(0.4\pi) \ll \Delta A_k(0.8\pi) \ll$, but also because the difference in the energy distribution to the sidebands for each ϕ [cf. Eq. (5.10)]. For $\phi = 0.4\pi$, $\gtrsim 90\%$ of the energy was contained in the primary (k=0) and first-order sidebands (k=1) for both the theoretical and measured spectrum. For $\phi = 0.8\pi$, $\lesssim 50\%$ of the energy is contained in the first-order sidebands (k=1) for the theoretical spectrum as compared to $\gtrsim 70\%$ of the energy for the measured spectrum. Therefore, the differences in $\Delta A_k(0.8\pi)$ was more sensitive than for $\Delta A_k(0.4\pi)$ and our A_k's

provided a much better predictive model for $\hat{\eta}_{c,s}$.

The DH $\hat{\eta}_c$ measurements in Fig. 5.5 had standard deviations of less than a percent (hence the exclusion from the figures). Our analytic model $\hat{\eta}_{c,s}$ agreed with our $\hat{\eta}'_{c,s}$ measurements to within 1.8%, which showed the accuracy of our methodology. In practice, these results show the impracticality of multi-longitudinal mode MO laser. If such a MO laser was used, the SNR would be extremely noisy with moving object in tactical applications due to the beating sidebands and η_c fluctuating, even at ranges within the coherence length ℓ_c.

5.4.2 PRBS modulation

A change in phase leads to a change in the instantaneous frequency $\delta\nu$, since

$$\delta\nu = \frac{1}{2\pi}\frac{d\phi}{dt}, \tag{5.13}$$

where $d\phi/dt$ is the change in phase with respect to time. Eq. (5.13) shows that phase fluctuations in the MO laser phase results in the frequency fluctuations too. If these phase fluctuations occur on the order or greater than the MO laser natural line, then the MO laser spectrum will be broadened. Therefore, by imparting deterministic, rapid phase changes in the form of PRBS phase modulation, we partially broadened the MO laser linewidth with a sinc^2 spectral lineshape. The spectrum of the MO laser with 15 MHz PRBS phase modulation is shown in Fig. 5.6. A fully broaden spectrum was not achieved because we applied a random discrete phase shift $\Delta\phi \approx 0.6\pi$, where

Table 5.1. The relative difference between $\hat{\eta}'_{c,s}$ and $\hat{\eta}_{c,s}$ from Fig. 5.5.

ϕ [rad]	$\Delta\ell$ [m]	$\overline{\lvert\hat{\eta}'_{c,s} - \hat{\eta}_{c,s}\rvert}$	$\overline{\lvert\hat{\eta}'_{c,s} - \hat{\eta}_{c,s}\left(A_k = J_k^2\right)\rvert}$
0.4π	3.1	1.5%	2.6%
0.8π	3.1	2.2%	12.1%
0.4π	22.4	1.7%	2.6%

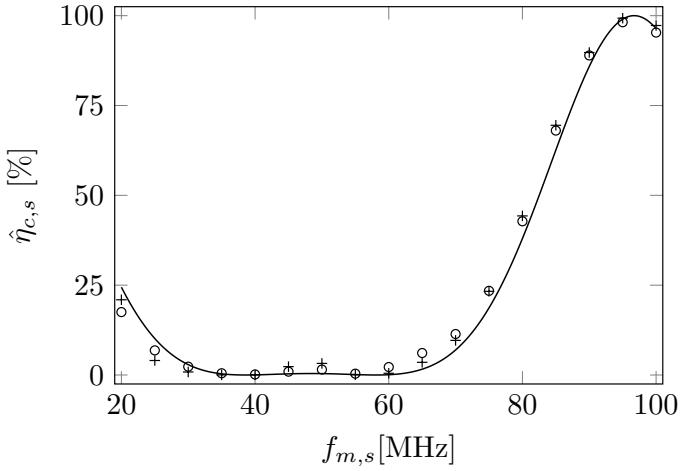

(a)

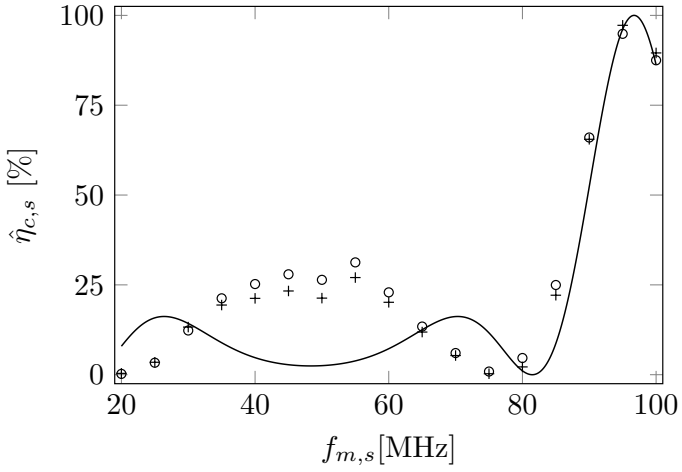

(b)

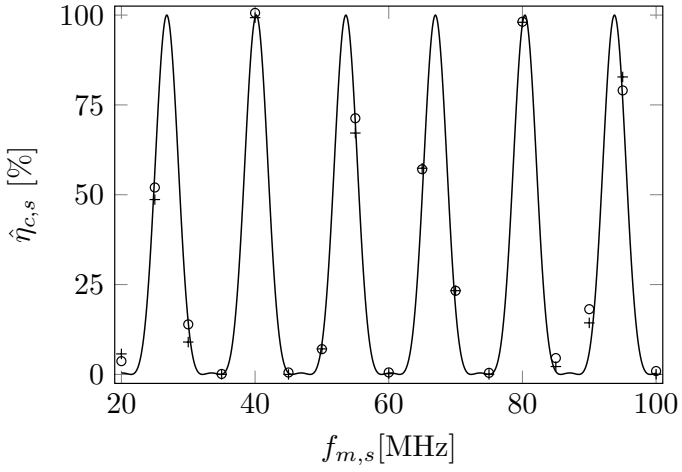

(c)

Figure 5.5. The $\hat{\eta}'_{c,s}$ (○) for sinusoidal phase modulation at a depth of modulation of (a & c) $\phi = 0.4\pi$ and (b) $\phi = 0.8\pi$ and at a path length difference of (a & b) $\Delta\ell = 3.1\,\mathrm{m}$ and (c) 22.4 m. These results show Eq. (5.12) with the FP measured sideband amplitudes (+) and Eq. (5.12) with $A_k(\phi, f_{m,s}) = J_k^2(\phi)$ from theory (−).

as previous work used $\Delta\phi \approx \pi$ [88] and produced a full sinc^2 profile. This is much like the sinusoidal modulation where increasing ϕ pushed more energy into the sidebands.

This led us to use a power spectral density, G_p, in the form of a summation of

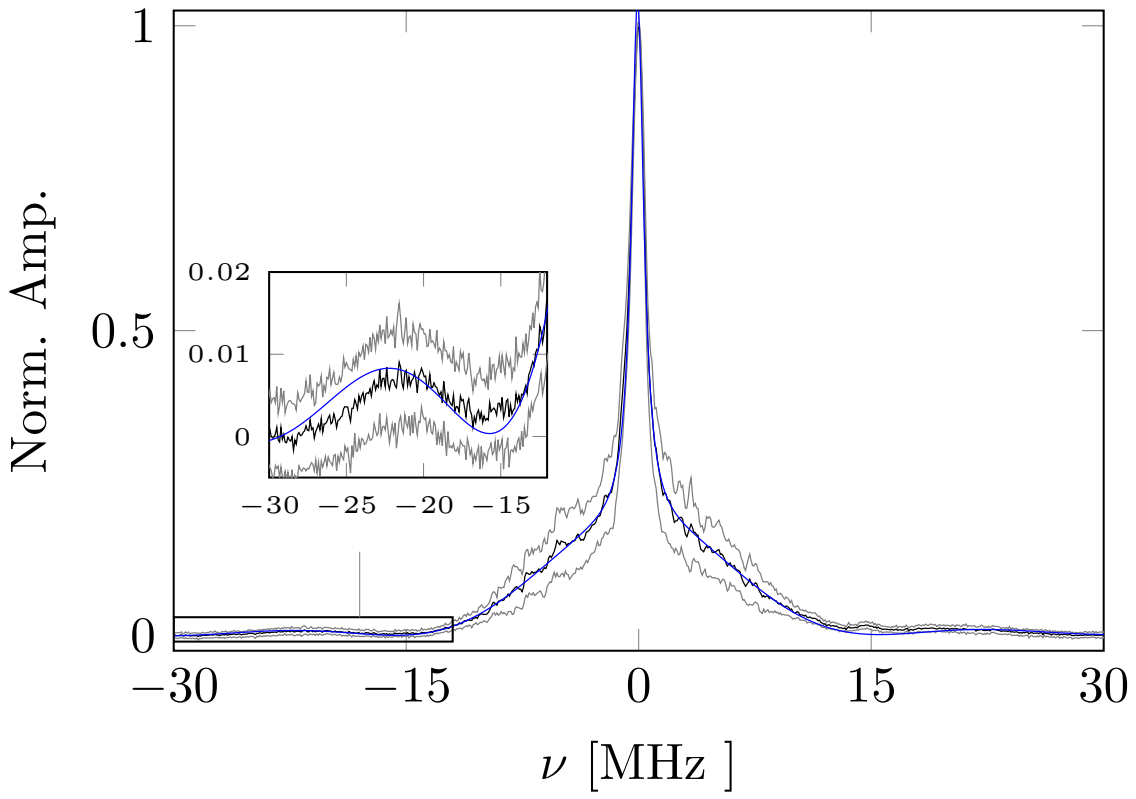

Figure 5.6. The average MO laser spectrum at 15 MHz PRBS phase modulation (–), the standard deviation (–), the fit with Eq. (5.14) (–).

the unmodulated and PRBS modulated spectrums, viz.

$$G_p(\nu) = \mathcal{L}(\nu) + A_p \text{sinc}^2\left(\frac{\nu - \nu_0}{\Delta\nu_p}\right), \tag{5.14}$$

where A_p is the sinc^2 amplitude and $\Delta\nu_p$ is the location of the sinc^2 nulls, which are ideally at $f_{m,p}$. We fit Eq. (5.14) with a baseline to the observed spectra shown in Fig. 5.6 for each $f_{m,p}$. These FP measurements were noisier despite the averaging as shown by the standard deviation of the scans in Fig. 5.6. The important fit results are shown in Table 5.2, where the values were rounded to the next decimal up from

the fit uncertainty (e.g., fit value = 0.86 with a fit uncertainty of 0.001). To quantify the amount of MO laser energy that was linewidth broaden, we included the factor β which is the ratio of the sinc^2 area to the total area of the spectrum. We observed that amount of the linewidth broadening slightly lessened with increasing $f_{m,p}$ and $\Delta\nu_L$ was 100-200 kHz less than the measured, unmodulated MO laser linewidth. We assumed this difference in the unmodulated MO laser linewidth was negligible since it is less than the spectral resolution of the FP (i.e., ¡ 1 MHz). From the Fourier transform of Eq. (5.14), we developed γ_p in the form of

$$\gamma_p(\tau) = (1-\beta)\exp(-\pi\Delta\nu\tau) + \beta\,\mathrm{tri}(\tau\Delta\nu_p), \tag{5.15}$$

where γ_p is a sum of the unmodulated and PRBS modulated $\gamma' s$. As such as before, our analytic model $\hat{\eta}_{c,p}$ became

$$\hat{\eta}_{c,p}(\tau) = \left[(1-\beta) + \beta\,\mathrm{tri}(\tau\Delta\nu_p)\exp(\pi\Delta\nu_L\tau)\right]^2, \tag{5.16}$$

where tri is the triangle function. We assumed a $\Delta\nu_L = 500\,\mathrm{kHz}$ consistent with the FP manufacturer specification for the typical best spectral resolution of ¡700 kHz. We also assumed $\Delta\nu_L$ is same for the unmodulated and modulated measurements despite the minor differences between the FP fits.

We measured $\hat{\eta}'_{c,p}$ at four different optical path length differences $\Delta\ell = 3.1\,\mathrm{m}$, 7.5 m, 14.9 m, and 22.4 m, which were estimated using the same sinusoidal phase

Table 5.2. Fit results of Eq. (5.14) on the MO laser spectrum with PRBS phase modulation.

f_m [MHz]	A_L	$\Delta\nu_L$ [MHz]	A_p	$\Delta\nu_p$ [MHz]	β
15	0.86	1.0	0.18	15.6	0.68
20	0.85	1.1	0.13	20.9	0.64
25	0.90	1.1	0.11	25.6	0.64
30	0.92	1.1	0.09	30.6	0.62

modulation technique as before. The results are shown in Fig. 5.7. These measurements were noisier than the sinusoidal phase modulation measurements. However, the trends in the $\hat{\eta}'_{c,p}$ agreed well with $\hat{\eta}_{c,p}$ and the spectral measurements. The slopes of the lines were well represented by the tri function in Eq. (5.16), where the average absolute error was 1.4%. Each $f_{m,p}$ leveled out at $\approx (1-\beta)^2$, which is beyond the PRBS phase modulation coherence length, and that level increased slightly with $f_{m,p}$, which was seen in the FP spectrum measurements. The DH measured $\hat{\eta}_c$ showed that β was slightly greater than the FP measured value because the data points fall below the line. However, the extrapolated β values from the data points using Eq. (5.15) were within a few percent of the FP measured values. These differences led to average absolute error of 6.9%, which was higher than the sinusoidal phase modulation.

This PRBS phase modulation of with $\Delta\phi \approx 0.6\pi$ at 15-30 MHz was representative of rapid frequency fluctuations. Effectively, this broadened the MO laser spectrum and shortens ℓ_c, since our t_i captured the hologram over many phase fluctuation (i.e., $t_i > 1/f_{m,p}$). Therefore, rapid phase fluctuations would decrease ℓ_c and the effective range of a practical DH system.

5.4.3 Sinusoidal with PRBS modulation

Lastly, we took measurements $\hat{\eta}'_{c,sp}$ with PRBS modulation at $f_{m,p} = 30$ MHz and combined with sinusoidal modulation at $f_{m,s} = 20 - 100$ MHz. We initially expected the two phase modulation effects to decrease $\hat{\eta}'_{c,sp}$ more than the product of $\hat{\eta}'_{c,s}$ and $\hat{\eta}'_{c,p}$ for low $f_{m,s}$ where the wings of the PRBS spectrum overlaps the sinusoidal phase modulation sidebands. Then as $f_{m,s}$ increased, $\hat{\eta}'_{c,sp} \approx \hat{\eta}'_{c,s}\hat{\eta}'_{c,p}$.

We show in Figure 5.8 the observed spectrum was decently approximated the $G_p(\nu)$ substitution for $\mathcal{L}(\nu)$ in Eq. (5.9) at $f_{m,s}$ =20 MHz and was better as $f_{m,s}$ increased. The small amplitude difference in the broad pedestal between the two

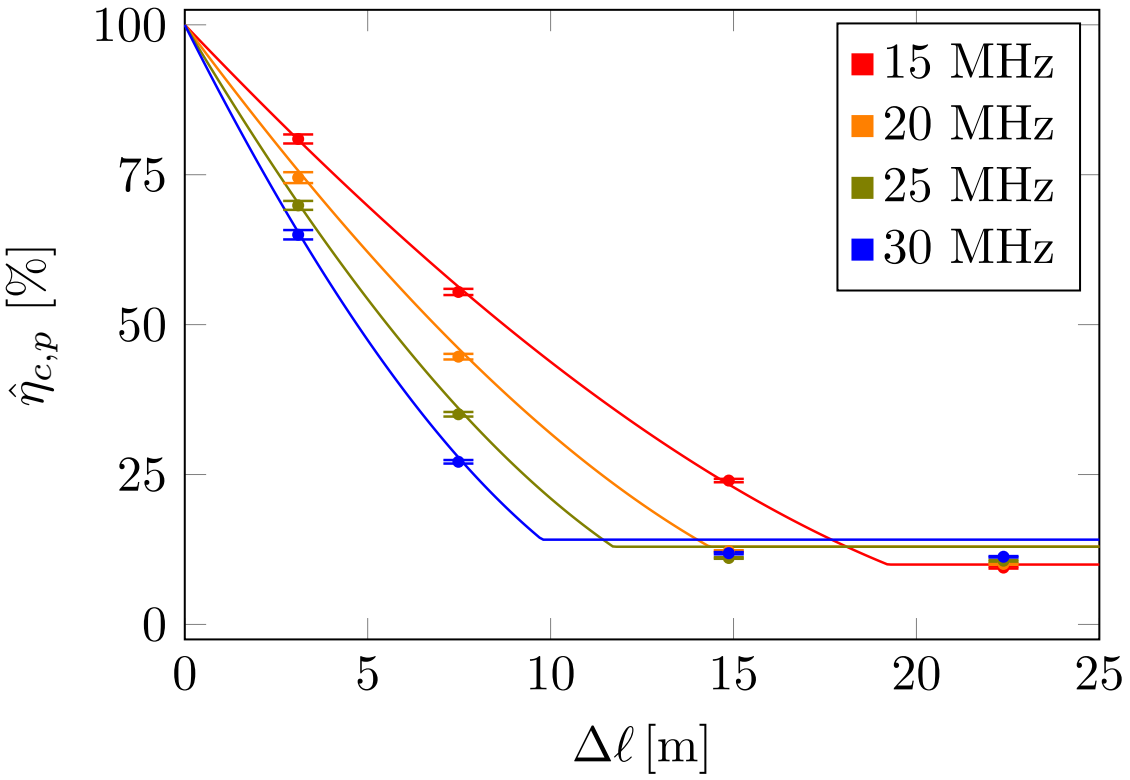

Figure 5.7. PRBS phase modulation results at various optical path length differences ($\Delta\ell$). The points represent the mean $\hat{\eta}'_{c,p}$, the error bars represent minimum and maximum measurement, and the lines represent Eq. (5.16) from the FP fits.

lines at $f_{m,s}$ =20 MHz was believed to be due to the exclusion of the cross-terms in Eq. (5.9). Otherwise, no correlation was observed between the two modulation types and the MO laser spectrums aligned well with our expectations from the previous FP measurements.

Figure 5.9 shows the results of $\hat{\eta}'_{c,sp}$ at $\Delta\ell = 3.1$ m. The product of $\hat{\eta}_{c,s}$ and $\hat{\eta}_{c,p}$ aligned well with $\hat{\eta}'_{c,sp}$ since the average absolute difference was 0.9%. Altogether, this shows that the efficiency losses associated with multiple coherence effects are multiplicative when there is no correlation between the coherence effects.

5.5 Conclusion

In this paper, we quantified different coherence effects on the heterodyne energy for DH in terms of a coherence efficiency η_c. We showed the quadratic relationship between the magnitude of the complex degree of coherence γ and η_c. Then, we experimentally measured the heterodyne energy losses using sinusoidal and PRBS phase modulation to change the coherence properties of the single-mode MO laser. The sinusoidal phase modulation produced sidebands on the MO center frequency, which is representative of the multi-longitudinal mode laser. The results show the impracticality of a multi-longitudinal mode laser, where the SNR will fluctuate rapidly with a moving object in tactical applications. The PRBS phase modulation produced a partially broaden spectrum, which is representative of rapid fluctuations of the MO laser's frequency. For both modulation types, the DH $\hat{\eta}_c$ measurements agreed well with the predictions from the FP spectral measurements with an average absolute error of 1.8% for sinusoidal and 6.8% for PRBS phase modulation. Such rapid phase fluctuations decreases the ℓ_c and thus the effective range of a DH system in practice.

We also combined the sinusoidal and PRBS phase modulation to investigate the total effect of two independent coherence effects. We observed no correlation between the two phase modulation types and the resulting measured $\hat{\eta}_c$ was well approximated by the multiplication of the two independent coherence effects with an average absolute error of 0.9%. These results also show DH is an effective technique to measure laser coherence effects.

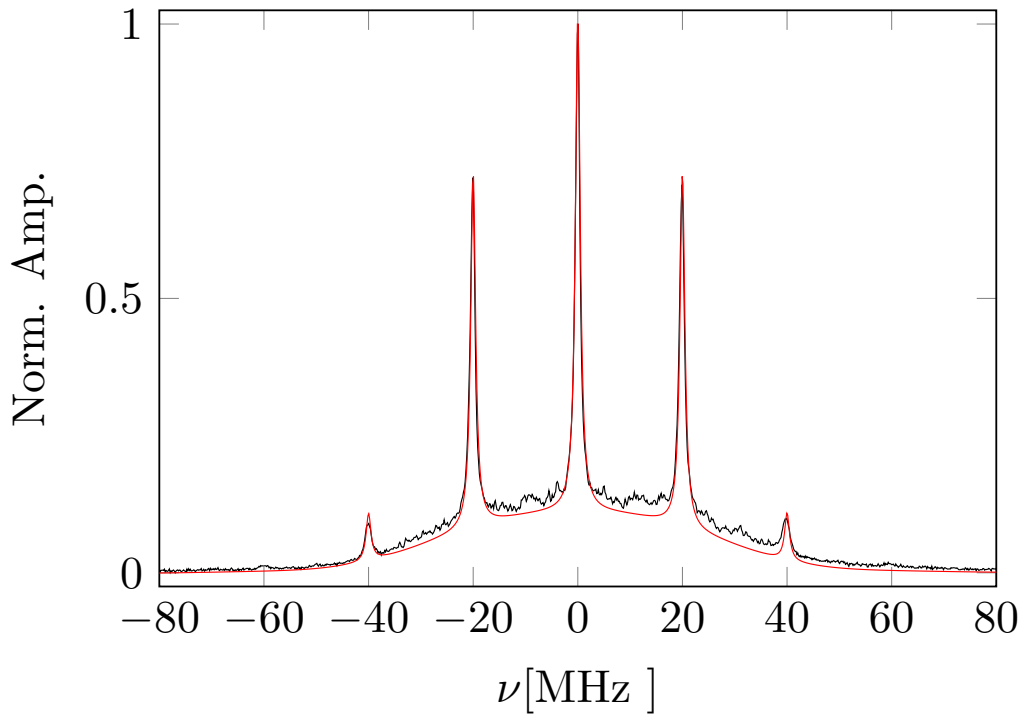

(a)

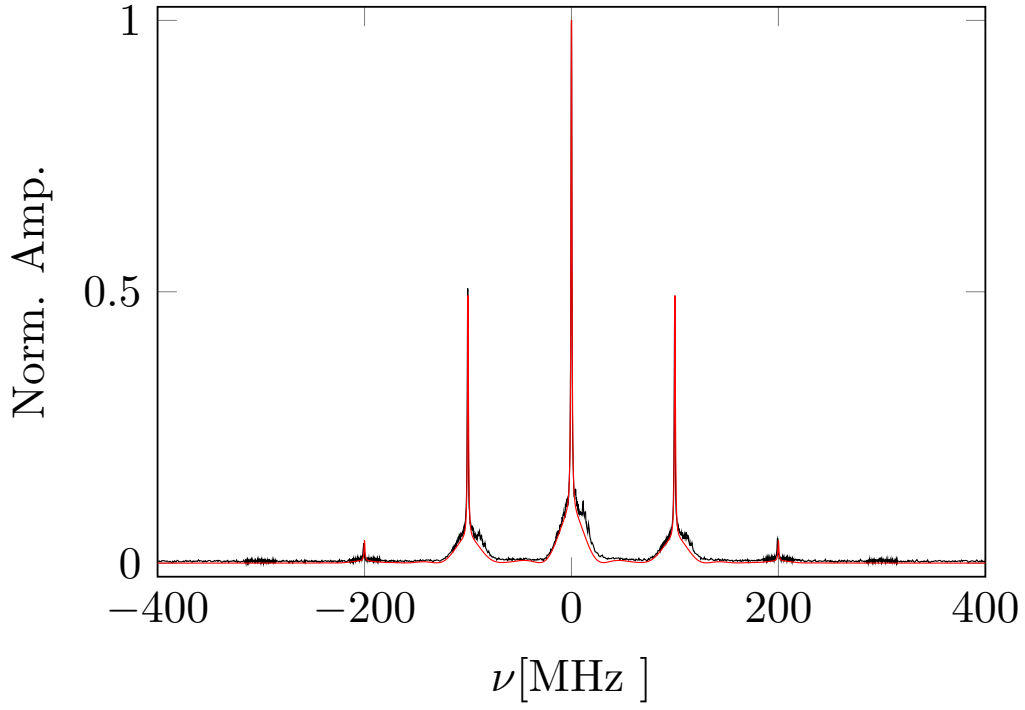

(b)

Figure 5.8. **The average MO laser spectrum (–) with PRBS phase modulation $f_{m,p}$ =30 MHz and sinusoidal phase modulation with $\phi = 0.4\pi$ and $f_{m,s}$ = 20 MHz (a) and 100 MHz (b). Also shown, Eq. (5.9) with $G_p(\nu)$ substituted for the Lorentzian lineshape (–).**

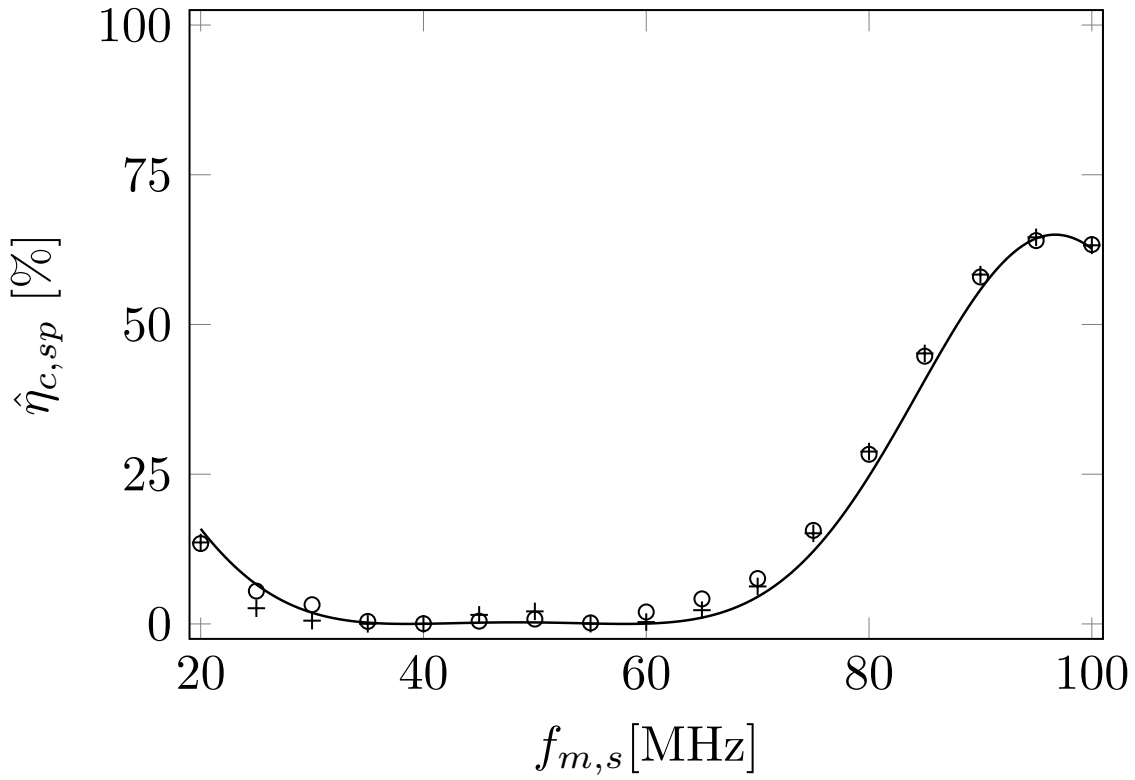

Figure 5.9. The $\hat{\eta}'_{c,sp}$ for the combination of PRBS phase modulation $f_{m,p}$ =30 MHz and sinusoidal phase modulation with $\phi = 0.4\pi$ and $f_{m,s}$ = 20-100 MHz ($\circ$). Also shown, the product of $\hat{\eta}'_{c,s}$ from Fig. 5.5(a) and $\hat{\eta}'_{c,p}$ for $f_{m,p} = 30$ MHz (+), and Eq. (5.12) with $A_k = J_k^2$ ($-$) multiplied by Eq. (5.16) for $\Delta\nu_p = f_{m,p}$ =30 MHz.

VI. Digital-holography mixing efficiency in the presence of vibrations and flicker noise

The contents of this chapter is a draft for submission to the *IEEE Journal of Quantum Electronics* [94].

This paper characterizes the mixing efficiency of digital holography, which is how well the detected signal and reference interfere, with respect to the hologram integration time-dependence for vibration and coherence losses. We measured the mixing efficiency of our DH system at various integration times and path length differences between the signal and reference. We observed a 94% vibration efficiency for an integration time of 100 ms and minimized vibration effects with an efficiency of 100% when the integration time $\leq$1 ms. We also observed the effective coherence length of the master oscillator laser increased by 280% when the integration time was decreased from 100 ms to 100 μs. To model this outcome, we present a model of the coherence efficiency based on the MO laser frequency noise. The model fit shows that the MO laser frequency was flicker noise dominated. For both the vibration and coherence efficiency, decreasing the integration time improves the efficiencies by acting as a high-pass filter.

6.1 Introduction

Applications for digital holography (DH) are diverse with significantly different system requirements. For near field applications, such as microscopy, the signal and reference are nearly path-length matched and are not limited by the signal-to-noise ratio (SNR). These applications can use laser sources with a short coherence length [5, 95] or even incoherent light sources [96]. However, for applications like wavefront sensing [20, 21, 39] and long-range imaging [79, 80, 17], the SNR and laser coherence is a range limiting factor. Therefore, understanding the effects of laser coherence for

DH is critical for these larger scale applications.

The mixing efficiency, which is how well the signal and reference interference fringes are detected, is typically the dominate efficiency loss of a DH system. Our previous experiments experimentally measured the mixing efficiency of a DH system with a path-length matched signal for near-ideal coherence and reference and no observed vibration effects [65]. Therefore, the mixing efficiency was only dependent on the polarization efficiency, which was a 50% from the depolarized signal, and the pixel modulation transfer function (MTF) loss from sampling the fringes, which was a 74% efficiency for our camera. For tactical applications however, the mixing efficiency can incur additional losses from vibrations and laser coherence over range.

Vibrations in a DH system causes the fringes to fluctuate across the camera pixels. The source of the vibrations can be from a range of phenomenon such as platform jitter, acoustic, etc. If the fringes fluctuate across the pixels over the course of the camera integration time, then the vibrations smooth the fringes and reduces the fringe visibility, which is proportional to the mixing efficiency. If the camera integration time is shorter than the rate of the fringe fluctuations, then fringes are static over the integration time and the vibration losses can be negated.

The coherence efficiency is quadratically dependent on the complex-degree of coherence [78]. The coherence length is inversely proportional to the laser linewidth, which provides a gauge for the distance when coherence losses become significant. The phenomenon contributing the linewidth of diode lasers, which is a common source for single-mode master oscillator (MO) lasers, has been studied [97]. The frequency and phase noise from diode lasers, which determines the laser linewidth, has been well studied [98, 99, 100]. Flicker noise (i.e., $1/f$ noise) in the laser frequency has been observed as early as 1967 [101], which is due to the lifetimes of the charge carriers [102], and has been studied [103, 104]. When laser frequency noise is dominated by

flicker noise, the observed linewidth is integration time dependent [105, 106]. Therefore, the laser frequency noise characteristics and t_i should also be considered when assessing the performance and capabilities of a DH system for long-range applications.

In what follows, we first provide our mixing efficiency model that characterizes the independent effects as multiplicative efficiency losses. Then we give the details on our DH experiment to measure our DH system's mixing efficiency with respect to t_i and $\Delta\ell$. Last, we present the analysis on the mixing efficiency measurements with respect to our model.

6.2 Mixing efficiency model

As a reminder, η_m is a measure of how well the signal and reference light interference is detected. We define η_m here to be comprised of four other efficiencies as described as

$$\eta_m(\tau, t_i) = \eta_p \eta_s \eta_v(t_i) \eta_c(\tau, t_i), \tag{6.1}$$

where τ is the time delay between the signal and reference, t_i is the hologram or pixel integration time, polarization efficiency η_p, spatial-fringe integration efficiency η_s, vibration efficiency η_v, and coherence efficiency η_c.

For η_p, the object scatters the illumination and depolarizes the recieved signal. For a dielectric material, like in our experiment, the signal is 100% depolarized. Since the depolarized signal interferes with the polarized reference, we assume $\eta_p = 50\%$ [67].

Additionally, we detect the fringes on discrete pixels, which smooths the detected fringes and imparts an efficiency loss, η_s. This spatial integration of the fringes can be mathematically described as the hologram irradiance convolved with the pixel. The convolution turns into a multiplication of the Fourier transform of the hologram irradiance with the pixel modulation transfer function (MTF) in the Fourier plane.

For a square pixel, the pixel MTF is sinc. We estimate η_s by averaging the magnitude squared of the pixel MTF over the pupil window in the Fourier plane. With an ideal square pixel, $\eta_s \approx 64\%$, but the pixel MTF can differ with the rise of microlenses and other novel FPA pixel designs (e.g., our previous results yielded an $\eta_s \approx 74\%$ [65]).

Furthermore, the vibration efficiency η_v captures the losses from the blurring of the fringes across the FPA pixels due to vibrations. If t_i is faster than the vibrations, then $\eta_v \approx 100\%$ and the fringes are stable over t_i. When vibrations occur during t_i, then $\eta_v < 100\%$. This is empirically estimated in our experiment.

For η_c, several MO laser coherence phenomenon can degrade $\mathcal{V}$ such as power fluctuations, center frequency mismatch, and phase fluctuations between the signal and reference. Of the three phenomena, only the MO laser power and phase fluctuations is dependent on the hologram integration time. However, evidence for MO laser power fluctuations would have to be significant for this phenomenon to be the dominate source for an integration time-dependent mixing efficiency measurements, which lacks from the ensuing experimental measurements. Therefore, we turn to the MO laser phase fluctuations, which is well documented as the dominate source for integration time-dependent linewidth measurements [105].

To begin our model for η_c, we model the cw MO laser field, $U(t)$, as

$$U(t) = U_o \exp(j2\pi\overline{\nu}t) \exp(j\phi(t)), \tag{6.2}$$

where U_o is the amplitude, $\overline{\nu}$ is the MO laser mean center frequency and $\phi(t)$ is the random phase fluctuations. With Eq. (6.2), the MO laser is a quasi-monochromatic light source with a linewidth due to $\phi(t)$ and constant amplitude. Next, we assume that $\phi(t)$ is a zero mean Gaussian random process. Therefore, the random phase of the signal light, $\phi_S(t_1)$, and the reference light, $\phi_R(t_2)$, are Gaussian, and so is the relative difference $\Delta\phi(t_1, t_2) = \phi_S(t_1) - \phi_R(t_2)$[36]. We also assume $\phi(t)$ is at least

stationary in first increments, so that $\Delta\phi$ is only dependent on τ. As a result, the mean $\langle\Delta\phi(\tau)\rangle = 0$ and the variance, $\sigma^2_{\Delta\phi}(\tau)$, is

$$\sigma^2_{\Delta\phi}(\tau) = \left\langle (\phi_S(t+\tau) - \phi_R(t))^2 \right\rangle . \tag{6.3}$$

Next, the normalized complex-degree of coherence, $\gamma(\tau)$, which is a normalized correlation, and $\mathcal{V} = |\gamma(\tau)|$ when the amplitude of the signal and reference are equal. We define $\gamma(\tau)$ in terms of the reference and signal as

$$\gamma(\tau) = \frac{\langle U^*_R(t) U_S(t+\tau)\rangle}{\langle U_R(0) U_S(0)\rangle}, \tag{6.4}$$

where U_R is the reference complex-optical field, U_S is the signal complex-optical field, and$\langle\cdot\rangle$ denotes expectation value. Then, we substitute Eq. (6.2) to represent the reference and signal into Eq. (6.4), which yields [107]

$$\gamma(\tau) = \langle \exp\left[j\Delta\phi(\tau)\right]\rangle = \exp\left[-\frac{1}{2}\sigma^2_{\Delta\phi}(\tau)\right]. \tag{6.5}$$

With this formulation in Eq. (6.2), we neglect effects due to MO laser amplitude fluctuations on $\gamma(\tau)$, but these effects have been considered [105].

To model $\sigma^2_{\Delta\phi}(\tau)$, we use the PSD of the laser frequency noise, $\mathcal{G}_{\delta\nu}(f)$, [108], as such

$$\sigma^2_{\Delta\phi}(\tau) = 4\pi^2\tau^2 \int_0^\infty \mathcal{G}_{\delta\nu}(f)\,\mathrm{sinc}^2(f\tau)\,df, \tag{6.6}$$

where $\mathrm{sinc}(0) = 1$ and $\mathrm{sinc}(x) = \sin(\pi x)/(\pi x)$ when $x \neq 0$. We see in Eq. (6.6) that even though the sinc^2 acts a low-pass filter ($f \lesssim 1/\tau$), $\sigma^2_{\Delta\phi}$ increases quadratically with τ. This quadratic relationship illustrates that as τ increases, $\phi(t)$ becomes more uncorrelated and the fluctuations of $\Delta\phi(t)$ increases for $f \lesssim 1/\tau$. As an approximation, we model $\mathcal{G}_{\delta\nu}(f)$, as a linear combination of flicker and white noise [109], which

is

$$\mathcal{G}_{\delta\nu}(f) = \frac{a}{f^{\alpha}} + \frac{\Delta\nu_o}{\pi}, \tag{6.7}$$

where a is the magnitude of the flicker noise, α is the log-power slope of the flicker noise ($1 \leq \alpha \leq 2$), and $\Delta\nu_o$ is the instantaneous linewidth due to white-phase noise only. In the case when $\mathcal{G}_{\delta\nu}(f)$ is dominated by white-phase noise, the MO laser PSD, $\mathcal{G}(\nu)$, has a Lorentzian lineshape and the integral in Eq. (6.6) converges. However, when $\mathcal{G}_{\delta\nu}(f)$ is dominated by flicker noise, $\mathcal{G}(\nu)$ has a Gaussian lineshape and Eq. (6.6) approaches infinity with a lower integration bound of zero. In reality, we have a finite measurement time, which acts as high-pass filter and $f \lesssim 1/t_i$ is not captured by the measured $\sigma^2_{\Delta\phi}(\tau, t_i)$. Therefore, we add the high-pass filter to Eq. (6.6) [108] and the measured $\sigma^2_{\Delta\phi}$ becomes

$$\sigma^2_{\Delta\phi}(\tau, t_i) = 4\pi^2\tau^2 \int_0^{\infty} \mathcal{G}_{\delta\nu}(f)\,\mathrm{sinc}^2(f\tau)\left\{1 - \mathrm{sinc}^2\left[f\left(t_i - \tau\right)\right]\right\}\, df, \tag{6.8}$$

so the frequency range of interest for $\mathcal{G}_{\delta\nu}(f)$ is essentially $1/t_i$ to $1/\tau$. Note that all the approximations leading to and including Eq. (6.8) assumes $t_i > \tau$ and $t_i > \tau_c$.

Since $\eta_c = |\gamma|^2$ [78], we substitute Eq. (6.8) in Eq. (6.5) and our model for η_c becomes

$$\eta_c(\tau, t_i) = \exp\left[-4\pi^2\tau^2 \int_0^{\infty} G_{\delta\nu}(f)\mathrm{sinc}^2\left(\pi f\tau\right)\left\{1 - \mathrm{sinc}^2\left[f\left(t_i - \tau\right)\right]\right\}\, df\right]. \tag{6.9}$$

While this description for Eq. (6.9) is adequate, other models may be possible. This closed-form expression in Eq. (6.9) is used here to characterize the experimental results due to MO laser frequency noise in our our DH system under test.

6.3 Experimental methods

This section details the experimental setup and data processing used to measure the mixing and coherence efficiency from the digital holograms. The experiment and data processing is similar to the those used in Thornton, et. al., where additional details maybe found [65, 78].

6.3.1 Experiment setup

The experimental setup is shown in Fig. 6.1. We used a cw, single-longitudinal mode, Cobalt Samba diode-pumped solid-state laser as the MO laser. The Samba provides 1W of power with a vendor specified linewidth <1 MHz and a coherence length $\ell_c > 100\,\text{m}$. From previous work [78], we characterized the MO laser linewidth as $\Delta\nu < 500\,\text{kHz}$, which corresponds to a minimum $\ell_c > 260\,\text{m}$ and a minimum $\tau_c > 875\,\text{ns}$. To divert MO laser power, we used pairs of half-wave ($\lambda/2$) plates and polarizing beam splitters (PBS) to adjust the total power to a beam dump (BD), to create the local oscillator (LO), and to adjust the illuminator power to another BD. The LO path was fiber coupled using another $\lambda/2$ to match the slow axis of the polarization maintaining (PM) fiber. We steered the illuminator using mirrors (M) and passed it through a beam expander (BE) to illuminate a sheet of Labsphere Spectralon which has 99% Lambertian reflectivity. The reflected light was then imaged onto a Grasshopper3 camera using a 1 in lens to create the signal light. The fiber-coupled LO was injected at the pupil lens and centered onto the camera to create the reference light.

With a 4 m LO fiber, the signal and reference paths were nearly matched to within a few centimeters. The refractive index for the slow axis of the PM fiber was experimentally determined to be ≈ 1.5 from previous work [78]. We inserted a combination of 5 m, 10 m, 50 m, and 100 m length fiber to vary the optical path length, $\Delta\ell$, for

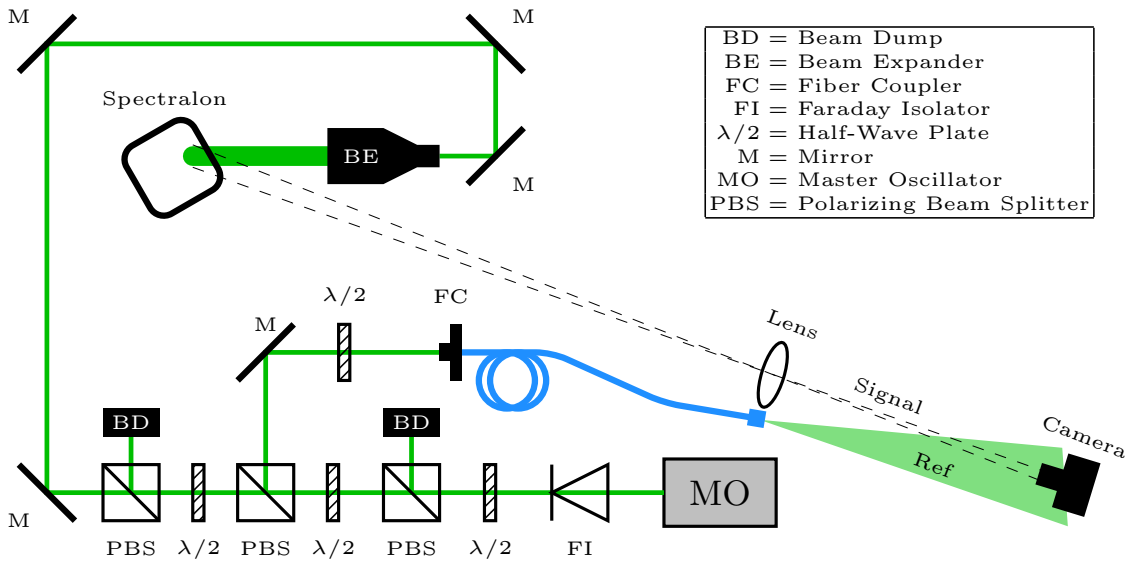

Figure 6.1. An illustration of the experimental setup

measurements at a $\Delta\ell = 0\,\text{m}$, $7.5\,\text{m}$, $15\,\text{m}$, $22.5\,\text{m}$, $50\,\text{m}$, $72.5\,\text{m}$, $150\,\text{m}$, $172.5\,\text{m}$, $225\,\text{m}$, and $247.5\,\text{m}$, which corresponds to a maximum $\tau = 825\,\text{ns}$. Additionally, we collected data at integrations times, t_i= $100\,\text{ms}$, $1\,\text{ms}$, and $100\,\mu\text{s}$. For comparison, t_i was greater than two to five orders of magnitude of the maximum τ and the suspected minimum τ_c.

For the collected data, we recorded a series of hologram, signal-only, and reference-only frames. We preformed speckle averaging by rotating the Spectralon between each speckle realization for a total of ten independent speckle realizations. Ten speckle realizations was determined to be sufficient to reduce the speckle noise to about 5% [65]. For each speckle realization, we collected twenty holograms and twenty signal-only frames for shot-noise averaging. Additionally, we collected twenty reference frames-only frames between each speckle realization. In total, we collected 200 holograms, signal-only, and reference-only frames at each $\Delta\ell$ and t_i.

6.3.2 Data processing

We measured the mixing efficiency η_m at each $\Delta\ell$ and t_i. To measure η_m, we used the 2D-Fast Fourier Transform (FFT) of each hologram and windowed the pupil in the Fourier plane. This windowed pupil also contained noise, so we flipped the 2D-FFT of the hologram and used the same pupil window to estimate the noise. Note that by measuring the noise this way, we assume the noise is symmetric in the Fourier plane over the window. Then, we subtracted the measured noise from the measured windowed pupil. The average over the Fourier plane windowed pupil without noise and over all frames was the average heterodyne energy $\overline{E}_H$. The average over all frames for the signal-only and reference-only frames was $\overline{m}_S$ and $\overline{m}_R$, respectively. Lastly, we measured the mixing efficiency, η'_m, using the following formula

$$\eta'_m = \frac{\pi}{4q_I^2} \frac{\left\langle \overline{E}_H\left(x,y\right)\right\rangle}{\left\langle \overline{m}_S\left(x,y\right)\overline{m}_R\left(x,y\right)\right\rangle}, \tag{6.10}$$

where $\langle\cdot\rangle$ is the spatial average over all pixels and $q_I = 2.7$ is the image plane sampling quotient [23]. The $\pi/4q_I^2$ term in Eq. 6.10 is the ratio of the total number of pixels to the number of pixels in the Fourier plane pupil window, since $\overline{E}_H$ is averaged over less pixels than $\overline{m}_S$ and $\overline{m}_R$.

6.3.3 Measured MO laser frequency noise

We measured the MO laser's center frequency over time with a HighFinesse WU-2 wavemeter, which has a measurement resolution of ≈2 MHz and samples at ≈20 Hz. We took three datasets during the course of a day: dataset 1, which was minutes after the laser was locked onto single-frequency operation; dataset 2, which was an hour after dataset 1 completion; and dataset 3, which was minutes after dataset 2 completion. Figure 6.2(a) shows these laser frequency measurements, where the

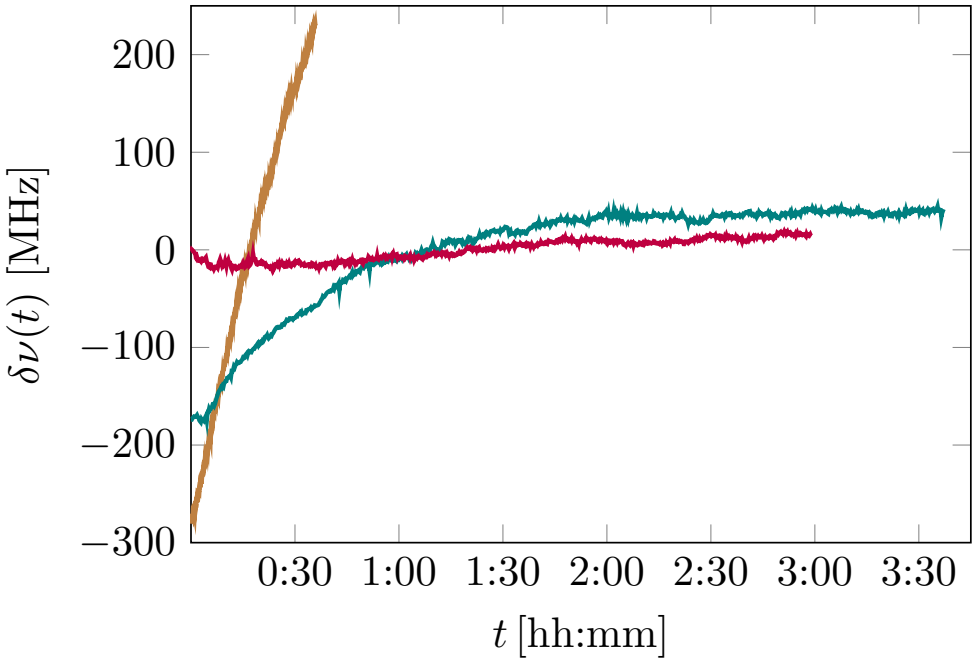

(a)

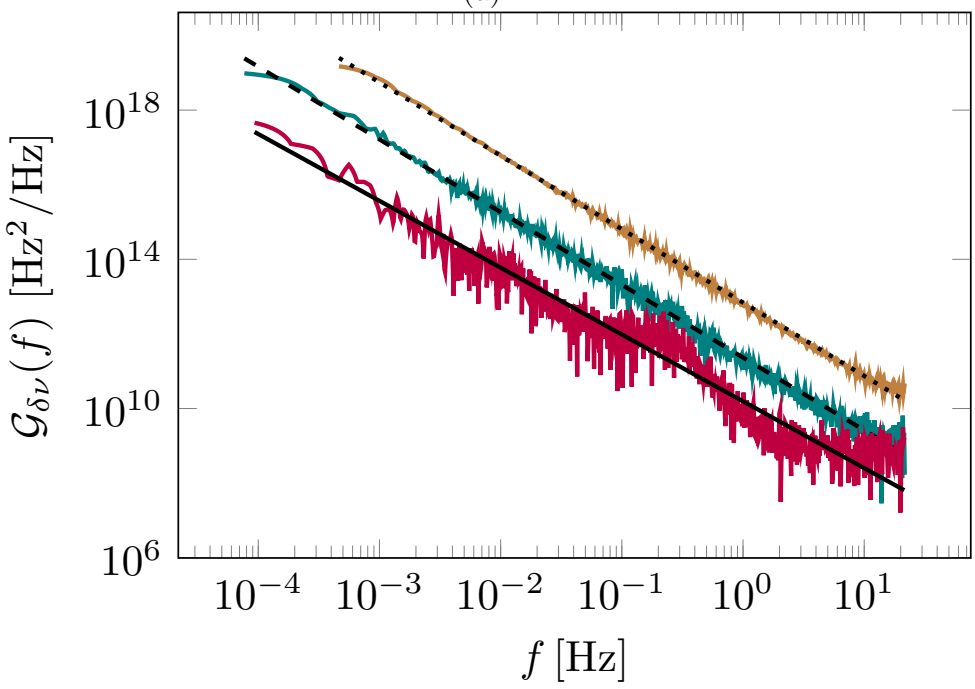

(b)

Figure 6.2. **(a) MO laser center frequency measurements for dataset 1 (—), dataset 2 (—), and dataset 1 (—). (b) The power spectral density of each data set from (a) with a fit of Eq. (6.11).**

mean of each dataset was subtracted from the each respective dataset to represent the frequency fluctuations $\delta\nu$. In dataset 1 of Fig. 6.2(a), we observed the center frequency rise on the order of 240 Hz/s for 30 minutes. Even though a difference in center frequency between signal and reference light would decrease η_c and the loss would increase over $\Delta\ell$, the maximum frequency difference over the maximum $\Delta\ell$ was less than 1 Hz. Therefore, this center frequency difference is negligible.

To further analyze the data, we calculated the PSD $G_{\delta\nu}$ of each data set as shown in Fig. 6.2(b). The PSD of each data set exhibited flicker noise. To quantify this flicker noise, we fit the following equation

$$\mathcal{G}_{\delta\nu}(f) = 10^a/f^{-\alpha}, \tag{6.11}$$

where a and α were the fit coefficients. The fit results of Eq. (6.11) are shown in Table 6.1, where the fit coefficients were rounded up from the fit uncertainty. We observed that the magnitude and slope of the flicker noise was different between datasets. The sampling frequency of the wavemeter was insignificant to obtain $\mathcal{G}_{\delta\nu}$ useful for our range of measurements ($1/t_i - 1/\tau = 10Hz - GHz$). However, the $\delta\nu$ measurements indicated that our MO laser frequency noise was dominated by flicker noise.

Table 6.1. Flicker noise fit coefficients

Dataset	1	2	3
a	12.8	11.3	10.2
α	1.98	1.96	1.79

6.4 Experimental results and analysis

In this section, we analyze our experimental results in two steps. For the first step, we show the η'_m results to analyze the measurements. Then, for the second step, we estimate η'_c from the first step to compare to our model using Eq. (6.9).

6.4.1 Mixing efficiency, η'_m

Figure 6.3 shows the η'_m results with error bars $\pm$ the standard deviation of the measurement, $\sigma_{\eta'_m}$. We fit each t_i dataset to the following Gaussian function

$$\eta'_m(\Delta\ell) = A\exp\left[-\left(\frac{\pi\Delta\nu c}{2\sqrt{\log(2)}\Delta\ell}\right)^2\right], \tag{6.12}$$

where $\Delta\nu$ is the observed laser linewidth and A is the relative amplitude. The mean of the residuals was 0.3%. As a reminder from our model in Eq. 6.1 and 6.9, only η_c is dependent on τ and $\Delta\ell$ and $\eta_c(\tau) = |\gamma(\tau)|^2$. Eq. (6.12) represents $|\gamma(\tau)|^2$ for a Gaussian lineshape of $\mathcal{G}(\nu)$. We chose to fit a Gaussian function because the fit results were much better than fitting to a decaying exponential function, where the mean of the residuals was 1.0%. Note that a decaying exponential function corresponds to a Lorentzian lineshape for $\mathcal{G}(\nu)$ and $\mathcal{G}_{\delta\nu}(\nu)$ is a constant [i.e. contains only white-phase noise (cf. Eq. (6.7))]. This outcome indicates that our MO laser was flicker noise dominated, as seen in the MO laser frequency measurements (cf. Section 6.3.3).

Table 6.2 shows the Eq. (6.12) fit results, where we rounded to the next digit up from the fit coefficient uncertainty. $\Delta\nu$ decreased by 65% when t_i decreased from 100 ms to 100 μs. This corresponded to τ_c increasing from 1.7 μs to 4.6 μs and ℓ_c increasing from 500 m to 1.4 km, which is a 280% increase.

Additionally, we observed that A increased 2.5% from t_i =100 ms to 1 ms and 100 μs. Even though our DH system was on a floated optical table, we believe this increase was due to some table or hardware vibrations. We believe the vibrations were mostly filtered out at t_i = 1 ms since the A's are approximately the same for t_i = 1 ms and 100 μs. Therefore, η'_v = 94% for t_i = 100 ms and η'_v = 100% for t_i = 1 ms and 100 μs. Additionally, the value of 37% for t_i = 1 ms and 100 μs agrees with our previous measurements [65].Note that later representations of this data will

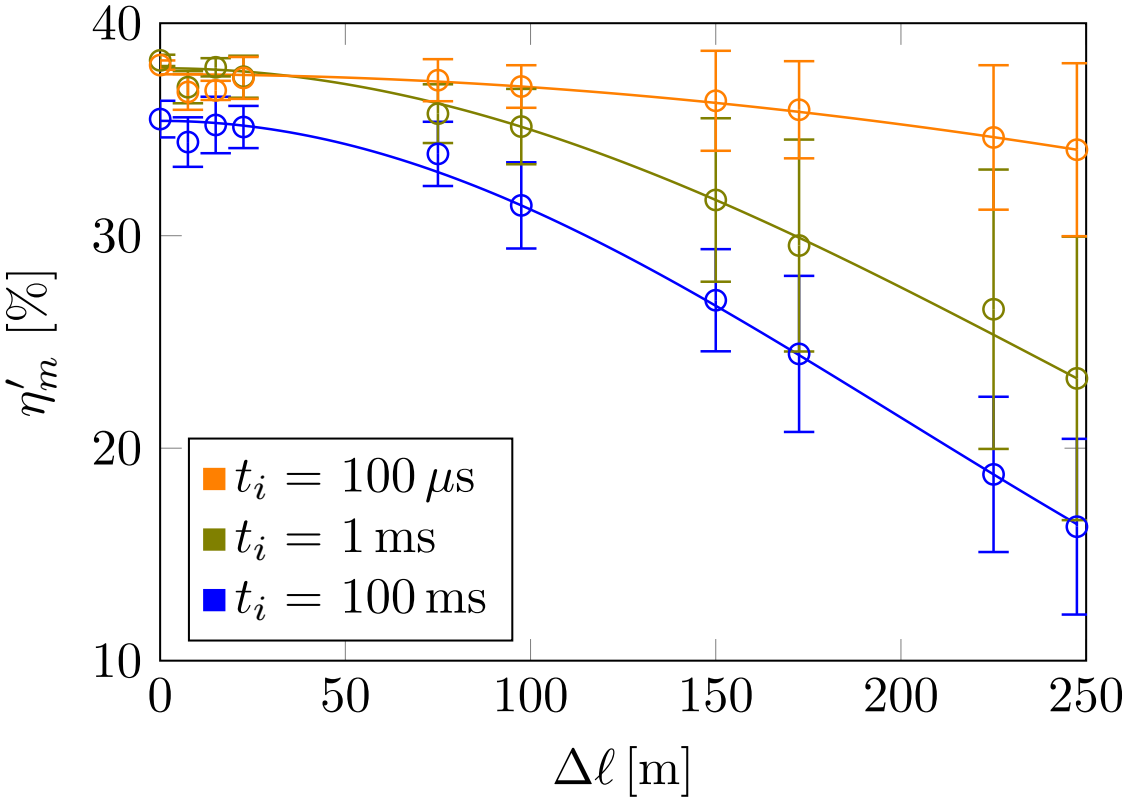

Figure 6.3. **The mixing efficiency measurements η'_m ($\circ$) with error bars $\pm\sigma$ and a Gaussian fit ($-$) to the data.**

be divided by the fit coefficient A to represent η_c'.

Additionally, we noticed a few features in Fig. 6.3. First, the dip in the datasets at 7.5 m was apparent in all three datasets. This illustrates that the laser PSD is probably not a smooth, symmetric Gaussian [110] and is not an experimental error. Secondly, we observed that $\sigma_{\eta_m'}$ increased as $\Delta\ell$ increased. This was expected because the random phase fluctuations become more uncorrelated as $\Delta\ell$ increases and the measurement becomes noisier. Thirdly, a few data points deviated a few percentage points from the Gaussian fit. We believe this is because the laser frequency noise varied slightly over the course of all measurements.

Table 6.2. Gaussian fit coefficients

t_i	100 ms	1 ms	100 μs
A [%]	35	37	37
$\Delta\nu$ [kHz]	400	320	140

6.4.2 Coherence efficiency, η_c'

The primary purpose to estimate and fit η_c' using our η_c model [cf. Eq. (6.9)] was to gain insight whether $\mathcal{G}_{\delta\nu}(f)$ was flicker noise dominated in all three t_i datasets. Obviously from Fig. 6.3, none of the data sets were white noise limited since a Gaussian function fit the data much better than a decaying exponential. However, if we were approaching the white noise limit (i.e., $\mathcal{G}_{\delta\nu}(f)$ was neither flicker nor white noise dominant), then η_c' lineshape would be a multiplication of a Gaussian and decaying exponential given by the Voigt spectral lineshape [109]. Therefore, by using Eq. (6.9) and including both flicker and white noise in $\mathcal{G}_{\delta\nu}(f)$ [cf.Eq. (6.7)], then the fits provide additional information. We estimated η_c' by dividing η_m' by A from Table 6.2. Note that the difference between η_m' and η_c' is the y-intercept and not the shape. In Figure 6.4, we show η_c' with a fit of Eq. (6.9), where the mean of the fit residuals was 0.8%. We chose a and $\Delta\nu_o$ to be the fit coefficients and $\alpha = 1.91$, which is the mean

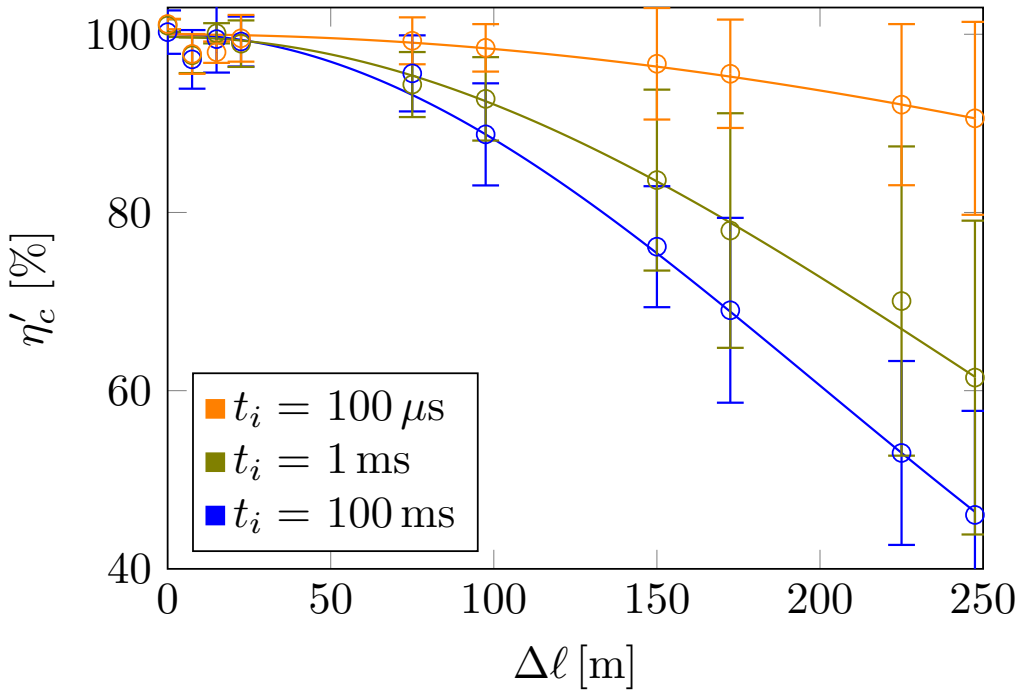

Figure 6.4. η_c' **results** ($\circ$) **with error bars** $\pm\sigma$ **and an independent fit for each** t_i **using Eq. (6.9)** ($-$)

from Table 6.1, for $\mathcal{G}_{\delta\nu}(f)$. Note that we fixed the value for α because the fits were over determined when α was a fit coefficient and the coefficient uncertainties were unreasonable. The $\mathcal{G}_{\delta\nu}(f)$ fit variables are shown in Table 6.3.

From our results, $\Delta\nu_o$ was minimized, which strongly indicates that our measurements were dominated by flicker noise. This outcome corroborates the Gaussian function fit of η_m' in Fig. 6.3 and the MO laser frequency noise measurements in Section 6.3.3. Therefore, we safely assumed that none of the measurements approached the white noise floor of the MO laser and a further reduction in t_i would decrease our observed linewidth and increase the τ_c and ℓ_c.

Table 6.3. Frequency noise fit coefficients

t_i	100 ms	1 ms	100 μs
a	10.9	12.5	12.5
$\Delta\nu_o$ [kHz]	0.00	0.00	0.00

6.5 Conclusion

In this paper, we presented a complete model for the mixing efficiency for DH to account for vibrational and laser frequency noise effects. Our mixing efficiency model is comprised of four independent efficiencies from different phenomenon: polarization (50%), spatial-fringe integration (74%), vibrations, and coherence. We experimentally measured the mixing efficiency at various optical path differences between the signal and reference, and at different integration times. At zero path length difference between the signal and reference, we observed the mixing efficiency decreased for the longest integration time, which we attributed to vibrations (94%). When the integration time was $\leq 1\,\text{ms}$, then the vibration efficiency was maximized (100%).

The measured mixing efficiency had a Gaussian shape with respect to the path length difference and the observed linewidth decreased by 65% when the integration time was decreased from 100 ms to 100 μs. This correlated to increasing the effective coherence length by 280%. These results indicated that the MO laser frequency noise was dominated by flicker noise. We developed a model for the coherence efficiency, which incorporates the effects of the laser frequency noise, and fit the model to the estimated the coherence efficiency from the mixing efficiency measurements. The results confirmed that the MO laser frequency noise was flicker noise dominated, not approaching the white noise limit, and further reduction in the integration time would increase coherence efficiency over range (i.e. increase the effective coherence length).

Overall, we show that the hologram integration time should be considered in the design of the DH system. Decreasing the integration time reduces vibration losses and increases the effective coherence length of the MO laser when the MO frequency noise is dominated by flicker noise. These hologram integration time effects present a trade space with respect to the vibration efficiency, coherence efficiency, and signal strength for the performance of a DH system

VII. Conclusions

This dissertation analyzed the system efficiencies (multiplicative losses) of a DH system for tactical applications in four submitted or accepted publications. The performance of DH in the on-axis phase shifting recording geometry was analyzed for deep-turbulence wavefront sensing and compared to a similar, well studied wavefront sensor, the self-referencing interferometer (SRI), with known efficiency losses. Closed-form expressions for the SNR and field-estimate Strehl ratio were developed for three phase shifting methods and deep-turbulence wave optics simulations with noise were conducted. The closed-form expressions were $< \pm 1\%$ of the simulations with ideal sampling and showed the 4-step method was the best. When the sampling was reduced, the simulations showed that a field-estimated Strehl ratio of 0.9 is achieved when the mean signal photoelectron is ≥ 10 and > 5 pixels/r_0. The SRI was modeled and simulated in similar fashion. A comparison of the results show that DH outperforms the SRI by 10's of dB due to DH's strong reference beam.

To quantify the major DH system efficiencies, an experiment with DH in the off-axis image plane recording geometry was conducted with a continuous-wave laser, where the signal and reference paths were matched for ideal coherence. The experimental results show that the mixing efficiency (37%) was the dominate efficiency loss and was 4.6% higher than expected. The cause for the increase is that the FPA used microlenses to achieve 100% pixel-fill factor, which would yield a slightly different MTF than the square-pixel model that was used. Additionally, excess reference noise (75%) was due to laser amplitude noise and a nonuniform reference, and excess signal noise (3%-100%) was signal strength dependent and originates from the Fourier plane window sampling a piece of the pupil autocorrelation. Both excess noise efficiencies could be considered significant losses, but the excess signal noise only became significant at measured SNRs > 100 and doesn't degrade performance. The measured

total-system efficiency was 21.1%, which was only 1.6% less than expected. These experimental results showed that a DH system could approach the mixing-efficiency limit if the other efficiencies are minimized.

The mixing efficiency includes the coherence efficiency of the master oscillator (MO) laser, which degrades over range, so additional experiments were conducted to explore the coherence effects of the MO laser. To do so, the MO laser was sinusoidally phase modulated to represent a multi-longitudinal mode MO laser, and was pseudo-random bit sequence phase modulated to induce rapid frequency fluctuations and line width broadening. The experimental results show that the DH effectively the measures the MO laser coherence efficiency to within 3.2% from the spectral models. When the two phase modulation schemes were combined, the results showed that the measured coherency efficiency was within 0.9% of the multiplication of the two independent coherence efficiencies since the two phase modulation types were uncorrelated. These results show that DH can measure coherence effects accurately. Conversely, the coherence efficiency can be estimated from the MO laser spectrum to quantify DH performance as a function of range.

Furthermore, the mixing efficiency was fully characterized to incorporate integration time-dependent effects. Platform and hardware vibrations reduced the mixing efficiency by 94%, but was filtered out when the integration time was faster than the vibrations. If the MO laser has significant low frequency laser frequency noise (e.g. $1/f$ or flicker noise is common in diode lasers), then the coherence efficiency can be increased over range. Essentially, the FPA integration time acts as a high-pass filter. Thus, by decreasing the hologram measurement time from 100 ms to 100 μs, the observed linewidth decreased from 400 kHz to 140 kHz and increased the coherence length (i.e. effective range) by 186%.

Overall, the DH system built for the experiments is the most efficient system

known to date. The quantification of the efficiencies presented provide a methodology to characterize the performance of a DH system. The dominate efficiency loss, the mixing efficiency, can also be well characterized to account for vibrational and coherence effects, which can be a range limiting factor.

7.1 Recommendations for future work

The first recommendation is to explore the spatial sampling requirements for the recording geometries of DH. Banet, et al. [62] and the work in Ch. III suggests that 4-5 pixels/r_0 in the pupil plane is required to estimate the signal complex-optical field adequately. Numerical simulations would be the easiest avenue to accomplish this study; however laboratory experiments would be a nice addition for real-world verification.

The second recommendation is to investigate another efficiency for Doppler compensation. For tactical applications, the imaged object will have relative motion to the DH system and the signal light's center frequency will be Doppler shifted. These losses are known in radar and can be modeled by the radar ambiguity function [111]. To minimize this loss, a separate control system would be utilized to shift the reference's center frequency to match the signal's center frequency and compensate for the Doppler shift. However, experimental verification is needed to compare to the hardware performance so it can be treated as another multiplicative efficiency loss, which is not readily found in the literature.

The third recommendation is to investigate the efficiency losses incurred with a pulsed DH system. The primary foreseen loss is the pulse overlap, which can also be captured by the radar ambiguity function. However, other unforeseen losses (e.g., the pulse shape changing from pulse to pulse) could be possible and experimental verification would be needed to compare to the hardware performance so the losses

can be well understood, which is also not readily found in the literature.

The fourth recommendation is using DH to characterize optical turbulence. Since DH can be used to estimate the phase along the optical path to resolve anisoplanatism [16, 17], the C_n^2 and r_0 can be calculated along the path from the estimated phase screens. Also, with a well calibrated DH system and target, the extinction along the path could be estimated in conjunction with the provided methodology in the second contribution. Field tests would require truth data to quantify the precision of DH to estimate these optical turbulence parameters. The last recommendation is to continue investigation of the observed MO laser coherence. In the last experiment, $t_i > \tau_c$ and $t_i > \tau$, so the ensuing research would investigate the effects of η_c when t_i approaches and becomes less than τ_c with respect to range (τ). Both an analytic treatment with experiments would facilitate a sound understanding.

Appendix A. Special functions

Kronecker Delta Function

$$\delta(x) = \begin{cases} 1, & x = 0 \\ 0, & x \neq 0 \end{cases} \tag{A.1}$$

Cardinal Sine Function[1]

$$\operatorname{sinc}(x) = \begin{cases} 1, & x = 0 \\ \frac{\sin(\pi x)}{\pi x}, & x \neq 0 \end{cases} \tag{A.2}$$

Circle Function[2]

$$\operatorname{circ}(r) = \begin{cases} 0, & r > 0.5 \\ .5, & r = 0.5 \\ 1, & r < 0.5 \end{cases}, \tag{A.3}$$

Rectangle Function[3]

$$\operatorname{rect}(x) = \begin{cases} 0, & |x| > 0.5 \\ .5, & |x| = 0.5 \\ 1, & |x| < 0.5 \end{cases} \tag{A.4}$$

Chat Function[4]

$$\operatorname{chat}(r) = \begin{cases} \frac{2}{\pi}\left[\arccos(r) - x\sqrt{1-r^2}\right], & r \leq 1 \\ 0, & r > 1 \end{cases} \tag{A.5}$$

Cauchy-Schwartz Inequality

$$\left|\left\langle U(x,y)\tilde{U}^*((x,y)\right\rangle\right|^2 \leq \left\langle |U(x,y)|^2\right\rangle \left\langle \left|\tilde{U}^*((x,y)\right|^2\right\rangle, \tag{A.6}$$

[1] See [112] for more details.
[2] $r = \sqrt{x^2 + y^2}$
[3] Also known as Heaviside Pi.
[4] Result from the autocorrelation of the circ function. See [36] for more details

Appendix B. Field-estimated Strehl ratio

The field-estimated Strehl ratio S_F is a performance metric that allows us to investigate the estimation accuracy of the various interferometric wavefront sensing methods [46, 57, 20, 21]. In practice, S_F results from the Cauchy-Schwartz Inequality, such that

$$|\langle U, V\rangle|^2 \leq \langle U, U\rangle\langle V, V\rangle, \tag{B.1}$$

where U and V are 2D arbitrary vectors in the field of complex numbers and $\langle\cdot,\cdot\rangle$ is the inner-product operator. By dividing both sides of Eq. B.1 by the right, we reach the following inequality:

$$1 \geq \frac{|\langle U, V\rangle|^2}{\langle U, U\rangle\langle V, V\rangle}, \tag{B.2}$$

which gives the properties of a Strehl ratio. This inequality ranges from 1, when $U = V$, to 0, when U is orthogonal to V, and is proportional to the similarity between the two complex vectors. However, the definition of S_F uses expectation values instead of inner products. The inner product for the complex vectors here is

$$\langle U, V\rangle = \sum_{i,j=1}^{m,n} U_{ij}V_{ij}^*, \tag{B.3}$$

where m, n is the number of elements in the corresponding i, j dimensions and the superscript $*$ denotes complex conjugate. We can ignore the customary transpose, since we desire a point-by-point comparison, and linearize the 2D vectors to 1D space. In this particular case, the expectation value is mathematically similar to the inner product, such that

$$\langle UV^*\rangle = \frac{1}{mn}\sum_{i,j=1}^{m,n} U_{ij}V_{ij}^* = \frac{1}{mn}\langle U, V\rangle. \tag{B.4}$$

Here, the nuance between the inner-product operator $\langle\cdot,\cdot\rangle$ and expectation-value operator $\langle\cdot\rangle$ is negligible in the calculation of S_F, since the factor of $1/(mn)^2$ cancels

in the numerator from the denominator. If we substitute the two complex vectors U and V with $\widehat{U}_S$ for the truth complex-optical field and $\widehat{U}_{S+N}$ for the estimated complex-optical field with noise, then S_F becomes

$$S_F = \frac{\left|\left\langle \widehat{U}_S(x,y)\widehat{U}^*_{S+N}(x,y)\right\rangle\right|^2}{\left\langle |\widehat{U}_S(x,y)|^2\right\rangle \left\langle |\widehat{U}_{S+N}(x,y)|^2\right\rangle}. \tag{B.5}$$

For all intents and purposes, we repeat Eq. B.5 above in Eq. 3.28.

Appendix C. Field-estimated Strehl ratio as a function of SNR

Rhoadarmer and Barchers [57] used the following relationship:

$$S_F = \frac{1}{1 + \frac{1}{S/N}} \tag{C.1}$$

to write the field-estimated Strehl ratio S_F as a function of the SNR S/N. Here, we show how these two metrics are related in Eq. C.1. For this purpose, $\widehat{U}_S$ is the estimated complex-optical field and $\widehat{U}_{S+N}$ is the estimated complex-optical field with noise, such that

$$\widehat{U}_{S+N}(x,y) = \widehat{U}_S(x,y) + \frac{\sigma_n}{\sqrt{2}} N_k(x,y), \tag{C.2}$$

where σ_n is the noise standard deviation and N_k is the kth realization of complex-circular Gaussian random numbers with zero mean and unit variance. Note that the factor of $\sqrt{2}$ in Eq. C.2 normalizes the variance since N_k has both real and imaginary parts. In turn, the numerator of S_F (cf. Eq. B.5) follows as

$$\left| \left\langle \widehat{U}_S(x,y) \widehat{U}^*_{S+N}(x,y) \right\rangle \right|^2 = \left| \left\langle \left| \widehat{U}_S(x,y) \right|^2 \right\rangle \right|^2, \tag{C.3}$$

since the additive-noise term has zero mean. Recall that $|U_R| \gg |U_S(x,y)|$; thus, we can assume that $\left|\widehat{U}_S(x,y)\right| \approx \left|\widehat{U}_S\right|$ in writing Eq. C.3. The second term in denominator of S_F then follows as

$$\left\langle \left| \widehat{U}_{S+N}(x,y) \right|^2 \right\rangle = \left\langle \left| \widehat{U}_S(x,y) \right|^2 \right\rangle + \sigma_n^2, \tag{C.4}$$

where the cross terms go to zero, since again the additive-noise term has zero mean. Substituting Eqs. C.3 and C.4 into Eq. B.5, the new form of S_F becomes

$$S_F = \frac{\left| \left\langle \left| \widehat{U}_S(x,y) \right|^2 \right\rangle \right|^2}{\left\langle \left| \widehat{U}_S(x,y) \right|^2 \right\rangle \left(\left\langle \left| \widehat{U}_S(x,y) \right|^2 \right\rangle + \sigma_n^2 \right)}. \tag{C.5}$$

Here, a factor of $\left\langle \left| \widehat{U}(x,y) \right|^2 \right\rangle$ in the numerator cancels the first term in denominator. Thus, we arrive at the following relationship:

$$S_F = \frac{1}{1 + \frac{\sigma_n^2}{\left\langle \left| \widehat{U}_S(x,y) \right|^2 \right\rangle}}, \tag{C.6}$$

where it is apparent that the second term in the denominator is the inverse of the SNR S/N, since

$$S/N = \frac{\left\langle \left| \widehat{U}_S(x,y) \right|^2 \right\rangle}{\sigma_n^2}. \tag{C.7}$$

For all intents and purposes, we repeat Eq. C.7 above in Eq. 3.16.

Appendix D. Previous efficiency experiment details

As summarized in Fig. D.1 and Table D.1, we carried out another experiment in a similar fashion to the one presented in this paper. The main hardware differences were a different vendor for the MO and FPA, but the majority of the specifications for each were comparable. Additional details can be found in Thornton et al. [68].

Table D.1. Previous Experiment Details

Quantity	Value	Source
Bit Depth	8	N/A
σ_r^2 $[pe^2]$	121	Vendor
η_q [%]	50	Vendor
ℓ $[pe]$	7,700	Vendor
$\overline{m}_B$ $[pe]$	3.3	Measured
$\overline{m}_R$ $[pe]$	4,116	Measured

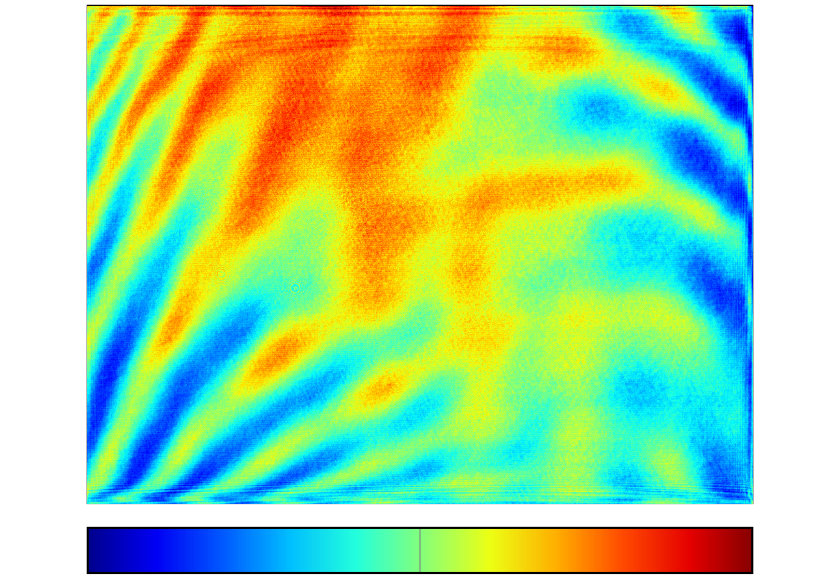

(a)

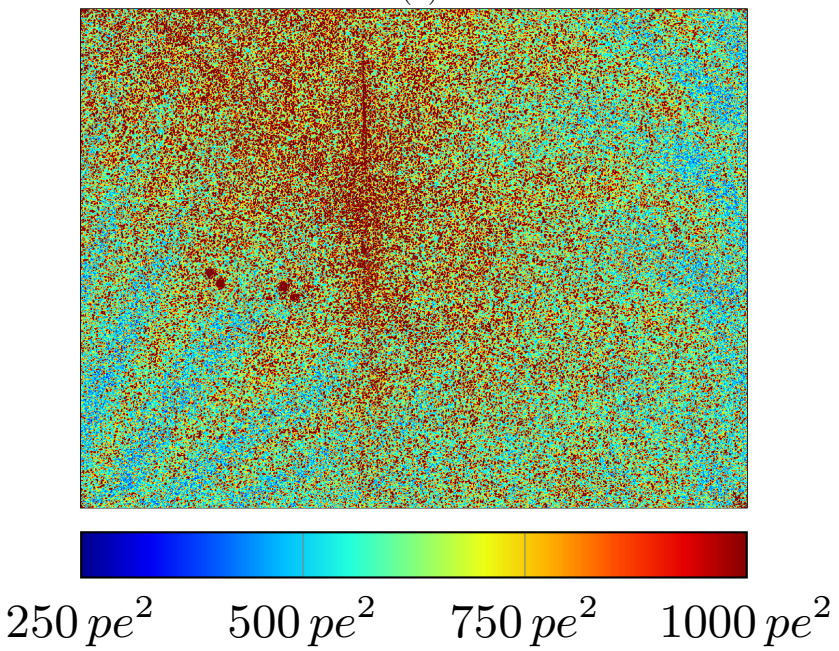

(b)

Figure D.1. (a) The mean number of reference photoelectrons $\overline{m}_R(x, y)$ and (b) mean reference-noise energy $\overline{E}_R(x, y)$ for the previously conducted experiment.

Bibliography

1. J. W. Goodman, W. H. Huntley, D. W. Jackson, and M. Lehmann, "Wavefront-reconstruction imaging through random media," *Appl. Phys. Lett.*, vol. 8, no. 12, pp. 311–313, 1966.

2. J. W. Goodman and R. W. Lawrence, "Digital image formation from elecronically detected holograms," *Appl. Phys. Lett.*, vol. 11, no. 3, pp. 77–79, 1967.

3. J. D. Gaskill, "Imaging Through a Randomly Inhomogeneous Medium by Wavefront Reconstruction," *J. Opt. Soc. Am. A*, vol. 58, no. 5, pp. 600–608, 1968.

4. J. W. Goodman, D. W. Jackson, M. Lehmann, J. Knotts, and A. P. Profile, "Experiments in Long-Distance Holographic Imagery," *Appl. Opt.*, vol. 8, no. 8, pp. 1581–1586, 1969.

5. G. Pedrini and H. J. Tiziani, "Short-coherence digital microscopy by use of a lensless holographic imaging system," *Appl. Opt.*, vol. 41, no. 22, pp. 4489–4496, 2002.

6. I. Yamaguchi and T. Zhang, "Phase-shifting digital holography," *Opt. Lett.*, vol. 22, no. 16, pp. 1268–1270, 1997.

7. P. Massatsch, F. Charrière, E. Cuche, P. Marquet, and C. D. Depeursinge, "Time-domain optical coherence tomography with digital holographic microscopy," *Appl. Opt.*, vol. 44, no. 10, pp. 1806–1812, 2005.

8. D. Hillmann, C. Lührs, T. Bonin, P. Koch, and G. Hüttmann, "Holoscopy holographic optical coherence tomography," *Opt. Lett.*, vol. 36, no. 13, pp. 2390–2392, 2011.

9. S. T. Thurman and J. R. Fienup, "Phase-error correction in digital holography," *J. Opt. Soc. Am. A*, vol. 25, no. 4, pp. 983–994, 2008.

10. J. C. Marron, R. L. Kendrick, N. Seldomridge, T. D. Grow, and T. A. Höft, "Atmospheric turbulence correction using digital holographic detection : experimental results," *Opt. Express*, vol. 17, no. 14, pp. 207–211, 2009.

11. J. C. Marron and K. S. Schroeder, "Holographic laser radar," *Opt. Lett.*, vol. 18, no. 5, pp. 385–387, 1993.

12. R. K. Tyson, *Introduction to Adaptive Optics*. SPIE Press, 2011.

13. D. L. Fried, "Branch point problem in adaptive optics," *J. Opt. Soc. Am. A*, vol. 15, no. 10, pp. 2759 – 2768, 1998.

14. S. T. Thurman and J. R. Fienup, "Correction of anisoplanatic phase errors in digital holography," vol. 25, no. 4, pp. 995–999, 2008.

15. A. E. Tippie and J. R. Fienup, "Phase-error correction for multiple planes using a sharpness metric," *Opt. Lett.*, vol. 34, no. 5, pp. 701–703, 2009.

16. A. E. Tippie and J. R. Fienup, "Multiple-plane anisoplanatic phase correction in a laboratory digital holography experiment," vol. 35, no. 19, pp. 3291–3293, 2010.

17. C. J. Pellizzari, M. F. Spencer, and C. A. Bouman, "Imaging through distributed-volume aberrations using single-shot digital holography," *J. Opt. Soc. Am. A*, vol. 36, no. 2, pp. 20–33, 2019.

18. M. F. Spencer and D. E. Thornton, "Signal-to-noise models for digital- holographic detection," *Proc. SPIE*, vol. 10650, pp. 1–17, 2018.

19. M. T. Banet and M. F. Spencer, "Multiplexed digital holography for atmospheric characterization," *Imaging and Applied Optics 2019 (COSI, IS, MATH, pcAOP)*, p. PTh1D.2, 2019.

20. M. F. Spencer, R. A. Raynor, M. T. Banet, and D. K. Marker, "Deep-turbulence wavefront sensing using digital-holographic detection in the off-axis image plane recording geometry," *Opt. Eng.*, vol. 56, no. 3, pp. 1–13, 2016.

21. M. T. Banet, M. F. Spencer, and R. A. Raynor, "Digital-holographic detection in the off-axis pupil plane recording geometry for deep-turbulence wavefront sensing," *Appl. Opt.*, vol. 57, no. 3, pp. 465–475, 2018.

22. J. C. Marron, R. L. Kendrick, S. T. Thurman, N. L. Seldomridge, T. D. Grow, C. W. Embry, and A. T. Bratcher, "Extended-range digital holographic imaging," *Proc. SPIE*, vol. 7684, pp. 2–7, 2010.

23. M. F. Spencer, "Spatial Heterodyne," *Encycl. Mod. Opt. II, Vol. IV*, pp. 369–400, 2017.

24. J. D. Gaskill, *Linear Systems, Fourier Transforms, and Optics*. Wiley, 1978.

25. B. E. A. Saleh and M. C. Teich, *Fundamentals of Photonics*. Wiley, 2007.

26. J. R. Janesick, *Photon Transfer*. SPIE Press, 2007.

27. D. Marco and D. L. Neuhoff, "The validity of the additive noise model for uniform scalar quantizers," *IEEE Trans. Inf. Theory*, vol. 51, no. 5, pp. 1739–1755, 2005.

28. E. L. Dereniak and G. D. Boreman, *Infrared Detectors and Systems*. Wiley, 1996.

29. J. W. Goodman, *Introduction to Fourier Optics*. Roberts & Company, 3rd ed., 2005.

30. A. N. Kolmogorov, "The local structure of turbulence in an incompressible viscous fluid for very large Reynolds numbers," *C. R. Acad. Sci. U.S.S.R.*, vol. 30, pp. 301–305, 1941.

31. D. L. Fried, "Statistics of a Geometric Representation of Wavefront Distortion," *J. Opt. Soc. Am.*, vol. 55, no. 11, pp. 1427–1435, 1965.

32. D. L. Fried, "Limiting Resolution Looking Down Through the Atmosphere," *J. Opt. Soc. Am.*, vol. 56, no. 10, pp. 1380–1384, 1966.

33. G. P. Perram, S. J. Cusumano, R. L. Hengehold, and S. Fiorino, *An Introduction to Laser Weapon Systems*. Directed Energy Professional Society, 2010.

34. J. D. Schmidt, *Numerical Simulation of Optical Wave Propagation with Examples in MATLAB*. SPIE Press, 2010.

35. L. C. Andrews and R. L. Phillips, *Laser Beam Propagation through Random Media*. SPIE Press, 2nd ed. ed., 2005.

36. J. W. Goodman, *Statistical Optics*. Wiley, 2nd ed., 2015.

37. E. Wolf, *Theory of Coherence and Polarization of Light*. Cambridge University Press, 2007.

38. L. Mandel, "Fluctuations of Photon Beams: The Distribution of the Photo-Electrons," *Proc. Phys. Soc.*, vol. 74, no. 3, pp. 233–243, 1959.

39. D. E. Thornton, M. F. Spencer, and G. P. Perram, "Deep-turbulence wavefront sensing using digital holography in the on-axis phase shifting recording geometry with comparisons to the self-referencing interferometer," *Appl. Opt.*, vol. 58, no. 5, pp. A179–A189, 2019.

40. J. D. Gaskill, "Atmospheric Degradation of Holographic Images," *J. Opt. Soc. Am*, vol. 59, no. 3, pp. 32–34, 1969.

41. J. W. Goodman, "Systems Application of Holography," *Proc. SPIE*, vol. 15, pp. 147–152, 1968.

42. D. L. Fried, "Optical Heterodyne Detection of an Atmospherically Distorted Signal Wave Front," *Proc. IEEE*, vol. 55, no. 1, pp. 57–67, 1967.

43. J. P. Moreland and S. A. Collins, "Optical Heterodyne Detection of a Randomly Distorted Signal Beam," *J. Opt. Soc. Am.*, vol. 59, no. 1, pp. 10–13, 1969.

44. J. D. Barchers, D. L. Fried, and D. J. Link, "Evaluation of the performance of Hartmann sensors in strong scintillation," *Appl. Opt.*, vol. 41, no. 6, pp. 1012–2021, 2002.

45. J. D. Barchers, D. L. Fried, and D. J. Link, "Evaluation of the performance of a shearing interferometer in strong scintillation in the absence of additive measurement noise," *Appl. Opt.*, vol. 41, no. 18, pp. 3674–3684, 2002.

46. J. D. Barchers and T. A. Rhoadarmer, "Evaluation of phase-shifting approaches for a point-diffraction interferometer with the mutual coherence function," *Appl. Opt.*, vol. 41, no. 36, pp. 7499–7509, 2002.

47. T. A. Rhoadarmer, "Development of a self-referencing interferometer wavefront sensor," *Proc. SPIE*, vol. 5553, pp. 112–126, 2004.

48. M. J. Steinbock, M. W. Hyde, and J. D. Schmidt, "LSPV+7, a branch-point-tolerant reconstructor for strong turbulence adaptive optics," *Appl. Opt.*, vol. 53, no. 18, pp. 3821–3831, 2014.

49. T. J. Brennan and T. A. Rhoadarmer, "Performance of a woofer-tweeter deformable mirror control architecture for high-bandwidth high-spatial resolution adaptive optics," *Proc. SPIE*, vol. 6306, pp. 1–12, 2006.

50. D. J. Wheeler and J. D. Schmidt, "Coupling of Gaussian Schell-model beams into single-mode optical fibers," *J. Opt. Soc. Am. A*, vol. 28, no. 6, pp. 1224–1238, 2011.

51. D. E. Thornton, M. F. Spencer, and G. P. Perram, "Deep-turbulence wavefront sensing using digital holography in the on- axis phase shifting recording geometry," *Proc. SPIE*, vol. 10410, pp. 1–13, 2017.

52. T. C. Poon and J. P. Liu, *Introduction to Modern Digital Holography.* Cambridge, 2014.

53. G. Nehmetallah, R. Aylo, and L. Williams, *Analog and Digital Holography with Matlab.* SPIE Press, 2015.

54. J. D. Schmidt, M. J. Steinbock, and E. C. Berg, "A flexible testbed for adaptive optics in strong turbulence," *Proc. SPIE*, vol. 8038, pp. 1–10, 2011.

55. T. A. Rhoadarmer and L. M. Klein, "Design of a spatially phase shifted self-referencing interferometer wave front sensor," *Proc. SPIE*, vol. 6306, pp. 1–12, 2006.

56. J. P. Liu, T. C. Poon, G. S. Jhou, and P. J. Chen, "Comparison of two-, three-, and four-exposure quadrature phase-shifting holography," *Appl. Opt.*, vol. 50, no. 16, pp. 2443–2450, 2011.

57. T. A. Rhoadarmer and J. D. Barchers, "Noise analysis for complex field estimation using a self-referencing interferometer wave front sensor," *Proc. SPIE*, vol. 4825, pp. 215–227, 2002.

58. T. J. Brennen, P. H. Roberts, and D. C. Mann, *WaveProp: A Wave Optics Simulation System for use with MATLAB, User's Guide Version 1.3*. Optical Sciences, 2010.

59. T. J. Brennen and P. H. Phillips, *AOTools: The Adaptive Optics Toolbox for use with MATLAB, User's Guide Version 1.4*. Optical Sciences, 2010.

60. M. F. Spencer, I. V. Dragulin, D. S. Cargill, and M. J. Steinbock, "Digital holography wave-front sensing in the presence of strong atmospheric turbulence and thermal blooming," *Proc. SPIE*, vol. 9617, pp. 1–17, 2015.

61. M. T. Banet, M. F. Spencer, R. A. Raynor, and D. K. Marker, "Digital holography wavefront sensing in the pupil-plane recording geometry for distributed-volume atmospheric aberrations," *Proc. SPIE*, vol. 9982, pp. 1–18, 2016.

62. M. T. Banet and M. F. Spencer, "Spatial-heterodyne sampling requirements in the off-axis pupil plane recording geometry for deep-turbulence wavefront sensing," *Proc. SPIE*, vol. 10410, pp. 1–13, 2017.

63. M. S. Corley and T. A. Rhoadarmer, "Evaluation of phase-shifting techniques for a self-referencing interferometer wavefront sensor," *Proc. SPIE*, vol. 5894, pp. 1–12, 2005.

64. T. R. Ellis, *Shack-Hartmann and Interferometric Hybrid Wavefront Sensor*. PhD thesis, The Air Force Institute of Technology, 2011.

65. D. E. Thornton, M. F. Spencer, C. A. Rice, and G. P. Perram, "Digital holography efficiency measurements with excess noise," *Appl. Opt.*, submitted.

66. P. M. Furth, V. Ponnapureddy, S. R. Dundigal, D. G. Voelz, R. Korupolu, A. Garimella, and M. W. Rashid, "Integrated CMOS sensor array for optical heterodyne phase sensing," *IEEE Sens. J.*, vol. 11, no. 6, pp. 1516–1521, 2011.

67. A. E. Siegman, "The Antenna Propertires of Optical Heterodyne Receivers," *Appl. Opt.*, vol. 5, no. 10, pp. 1588–1594, 1966.

68. D. E. Thornton, M. F. Spencer, C. A. Rice, and G. P. Perram, "Efficiency measurements for a digital- holography system," *Proc. SPIE*, vol. 10650, pp. 1–10, 2018.

69. M. C. Teich, "Infrared Heterodyne Detection," *Proc. IEEE*, vol. 56, pp. 37–46, 1968.

70. J. H. Shapiro, B. a. Capron, and R. C. Harney, "Imaging and target detection with a heterodyne-reception optical radar.," *Appl. Opt.*, vol. 20, no. 19, pp. 3292–3313, 1981.

71. R. Foord, R. Jones, J. M. Vaughan, and D. V. Willetts, "Precise comparison of experimental and theoretical SNRs in CO2 laser heterodyne systems.," *Appl. Opt.*, vol. 22, no. 23, pp. 3787–95, 1983.

72. G. R. Oesch, *Optical Detection Theory for Laser Applications*. Wiley, 2002.

73. P. Merritt and M. F. Spencer, *Beam Control for Laser Systems*. Directed Energy Professional Society, 2nd ed., 2018.

74. P. C. D. Hobbs, "Reaching the shot noise limit for $10," *Opt. Photonics News*, pp. 17–23, apr 1991.

75. R. Paschotta, "Intensity Noise," *Encycl. Laser Phys. Technol.*, 2008.

76. FLIR, "How to Evaluate Camera Sensitivity." https://www.ptgrey.com/white-paper/id/10912.

77. J. W. Goodman, *Speckle Phenomena In Optics*. Roberts & Company, 2007.

78. D. E. Thornton, D. Mao, M. F. Spencer, C. A. Rice, and G. P. Perram, "Digital holography experiments with degraded temporal coherence," *Opt. Eng.*, Draft.

79. C. J. Pellizzari, M. F. Spencer, and C. A. Bouman, "Phase-error estimation and image reconstruction from digital-holography data using a Bayesian framework," *J. Opt. Soc. Am. A*, vol. 34, no. 9, pp. 1659–1669, 2017.

80. C. J. Pellizzari, M. T. Banet, M. F. Spencer, and C. A. Bouman, "Demonstration of single-shot digital holography using a Bayesian framework," *J. Opt. Soc. Am. A*, vol. 35, no. 1, pp. 103–107, 2018.

81. M. F. Spencer, "Spatial Heterodyne," *Encycl. Mod. Opt. II, Vol. IV*, pp. 369–400, 2018.

82. L. Mandel, "Wavefront Reconstruction with Light of Finite Coherence Length," *J. Opt. Soc. Am.*, vol. 56, 1966.

83. M. Harris, G. N. Pearson, J. M. Vaughan, D. Letalick, and C. Karlsson, "The role of laser coherence length in continuous-wave coherent laser radar," *J. Mod. Opt.*, vol. 45, no. 8, pp. 1567–1581, 1998.

84. E. Fischer, E. Dalhoff, and H. Tiziani, "Overcoming coherence length limitation in two wavelength interferometry - an experimental verification," *Opt. Commun.*, vol. 123, no. February, pp. 465–472, 1996.

85. U. Hofbauer, E. Dalhoff, and H. Tiziani, "Double-heterodyne-interferometry with delay-lines larger than coherence length of the laser light used," *Opt. Commun.*, vol. 162, no. April, pp. 112–120, 1999.

86. Y. Salvadé, F. Przygodda, M. Rohner, A. Polster, Y. Meyer, S. Monnerat, O. Gloriod, M. Llera, R. Matthey, J. Di Francesco, F. Gruet, and G. Mileti, "Interferometric measurements beyond the coherence length of the laser source," *Opt. Express*, vol. 24, no. 19, pp. 21729–21743, 2016.

87. D. Claus, D. Iliescu, and J. M. Rodenburg, "Coherence requirement in digital holography.," *Appl. Opt.*, vol. 52, no. 1, pp. A326–A335, 2013.

88. B. Anderson, A. Flores, R. Holten, and I. Dajani, "Comparison of phase modulation schemes for coherently combined fiber amplifiers," *Opt. Express*, vol. 23, no. 21, pp. 27046–27060, 2015.

89. B. M. Anderson, A. Flores, and I. Dajani, "Filtered pseudo random modulated fiber amplifier with enhanced coherence and nonlinear suppression," *Opt. Express*, vol. 25, no. 15, pp. 17671–17682, 2017.

90. D. Mao, D. E. Thornton, M. F. Spencer, C. A. Rice, and G. P. Perram, "Sinusoidal Phase Modulation Effects on Digital Holography," *Proc. SPIE*.

91. N. Ismail, C. C. Kores, D. Geskus, and M. Pollnau, "Fabry-Pérot resonator: spectral line shapes, generic and related Airy distributions, linewidths, finesses, and performance at low or frequency-dependent reflectivity," *Opt. Express*, vol. 24, no. 15, pp. 3675–3676, 2016.

92. J. Buus, M.-C. Amann, and D. J. Blumenthal, *Tunable Laser Diodes and Related Optical Sources*. SPIE Press, 2nd ed., 2005.

93. P. E. Powers, *Field Guide to Nonlinear Optics*. SPIE Press, 2013.

94. D. E. Thornton, M. F. Spencer, C. A. Rice, and G. P. Perram, "Integration time-dependent mixing efficiency measurements of digital holography in the presence of laser frequency flicker noise," *IEEE J. Quantum Electron.*, Draft.

95. I. Yamaguchi, "Phase-Shifting Digital Holography," *Opt. Photonics News*, pp. 48–53, jul 2008.

96. W. Osten, A. Faridian, P. Gao, K. Körner, D. Naik, G. Pedrini, A. K. Singh, M. Takeda, and M. Wilke, "Recent advances in digital holography [Invited]," *Appl. Opt.*, vol. 53, no. 27, pp. G44—-G63, 2014.

97. M. Osinski and J. Buus, "Papers Linewidth Broadening Factor in Semiconductor Lasers-An Overview," *IEEE J. Quantum Electron.*, vol. QE-23, no. 1, 1987.

98. B. Daino, P. Spano, M. Tamburrini, and S. Pizzolla, "Phase Noise and Spectral Line Shape in Semiconductor Lasers," *IEEE J. Quantum Electron.*, vol. QE-19, no. 3, pp. 266–270, 1983.

99. C. H. Henry, "Theory of the Phase Noise and Power Spectrum of a Single Mode Injection Laser," *IEEE J. Quantum Electron.*, vol. QE-19, no. 9, pp. 1391–1397, 1983.

100. S. Piazzolla, P. Spano, and M. Tamburrini, "Characterization of phase noise in semiconductor lasers," *Appl. Phys. Lett.*, vol. 41, no. 695, pp. 1981–1983, 1982.

101. A. E. Siegman, B. Daino, and K. R. Manes, "Preliminary Measurements of Laser Short-Term Frequency Fluctuations," *IEEE J. Quantum Electron.*, vol. QE-3, no. 5, pp. 180–189, 1967.

102. A. Van der Ziel, "Noise in Solid-state Devices and Lasers," *Proc. IEEE*, vol. 58, no. 8, pp. 1178–1206, 1970.

103. L. B. Mercer, "1 /f Frequency Noise Effects on Self-Heterodyne Linewidth Measurements," *J. Light. Technol.*, vol. 9, no. 4, pp. 485–491, 1991.

104. Y. Salvade and R. Dandliker, "Limitations of interferometry due to the flicker noise of laser diodes," *J. Opt. Soc. Am. A*, vol. 17, no. 5, pp. 927–932, 2000.

105. K. Petermann, *Laser diode modulation and noise*. Kluwer Academic Publishers, 1988.

106. G. D. Domenico, S. Schilt, and P. Thomann, "Simple approach to the relation between laser frequency noise and laser line shape," *Appl. Opt.*, vol. 49, no. 25, pp. 4801–4807, 2010.

107. A. Papoulis, *Probability, Random Variables, and Stochastic Processes*. McGraw-Hill, 3rd ed., 1991.

108. L. S. Cutler and C. L. Searle, "Some Aspects of the Theorv and Measurement of Frequency Fluctuations in Frequency Standards," *Proc. IEEE*, vol. 54, no. 2, pp. 136–154, 1966.

109. G. M. Stephan, T. T. Tam, S. Blin, P. Besnard, and M. Tetu, "Laser line shape and spectral density of frequency noise," *Phys. Rev. A - At. Mol. Opt. Phys.*, vol. 71, pp. 1–9, 2005.

110. J. T. Verdeyen, *Laser Electronics*. Prentice-Hall, Inc., 3rd ed., 1995.

111. M. A. Richards, *Fundamentals of Radar Signal Processing*. McGraw-Hill, 2nd ed., 2014.

112. A. E. Siegman, "Why the sinc Function Should be Defined as (sinx)/x and not (sinπx/πx)," *Appl. Opt.*, vol. 13, no. 17, pp. 705–706, 1974.

REPORT DOCUMENTATION PAGE

Form Approved
OMB No. 0704–0188

1. REPORT DATE *(DD–MM–YYYY)*	2. REPORT TYPE	3. DATES COVERED *(From — To)*
31–08–2019	Doctoral Dissertation	Sep 2016 — Sep 2019

4. TITLE AND SUBTITLE

Digital Holography Efficiency Experiments for Tactical Applications

5a. CONTRACT NUMBER

5b. GRANT NUMBER

5c. PROGRAM ELEMENT NUMBER

6. AUTHOR(S)

Douglas E. Thornton

5d. PROJECT NUMBER

5e. TASK NUMBER

5f. WORK UNIT NUMBER

7. PERFORMING ORGANIZATION NAME(S) AND ADDRESS(ES)

Air Force Institute of Technology
Graduate School of Engineering and Management (AFIT/EN)
2950 Hobson Way
WPAFB, OH 45433-7765

8. PERFORMING ORGANIZATION REPORT NUMBER

AFIT/DS/ENP/19-S-029

9. SPONSORING / MONITORING AGENCY NAME(S) AND ADDRESS(ES)

Air Force Research Labs, Directed Energy Directorate
3550 Aberdeen Ave SE
Kirtland Air Force Base, NM 87117
DSN 263-1607, COMM 505-853-1607
Email: mark.spencer.6@us.af.mil

10. SPONSOR/MONITOR'S ACRONYM(S)

AFRL/RD

11. SPONSOR/MONITOR'S REPORT NUMBER(S)

12. DISTRIBUTION / AVAILABILITY STATEMENT

DISTRIBUTION STATEMENT A:
APPROVED FOR PUBLIC RELEASE; DISTRIBUTION UNLIMITED.

13. SUPPLEMENTARY NOTES

14. ABSTRACT

Digital holography (DH) uses coherent detection and offers direct access to the complex-optical field to sense and correct image aberrations in low signal-to-noise environments, which is critical for tactical applications. The performance of DH is compared to a similar, well studied deep-turbulence wavefront sensor, the self-referencing interferometer (SRI), with known efficiency losses. Wave optics simulations with deep-turbulence conditions and noise were conducted and the results show that DH outperforms the SRI by 10's of dB due to DH's strong reference. Additionally, efficiency experiments were conducted to investigate DH system losses. The experimental results show that the mixing efficiency (37%) is the dominate efficiency loss; however, excess reference noise (75%) and excess signal noise (3%-100%) are significant efficiency losses as well. Further experiments show DH effectively quantifies laser coherence as an efficiency to within ±3.2% of the spectral models and the observed laser coherence can be dependent on the hologram integration time. The observed laser linewidth was reduced 65% by decreasing the integration time from 100 ms to 100 μs, thus filtering laser frequency noise and increasing the effective system range by 280%.

15. SUBJECT TERMS

Digital holography; atmospheric turbulence; remote sensing; wavefront sensing; long-range imaging; coherence

16. SECURITY CLASSIFICATION OF:			17. LIMITATION OF ABSTRACT	18. NUMBER OF PAGES	19a. NAME OF RESPONSIBLE PERSON
a. REPORT	b. ABSTRACT	c. THIS PAGE			Dr. Glen P. Perram, AFIT/ENP
U	U	U	U	162	19b. TELEPHONE NUMBER *(include area code)* (937) 255-3636, x4504; glen.perram@afit.edu